TOPICAL REVIEW

Wave-based optical coherence elastography: the 10-year perspective

To cite this article: Fernando Zvietcovich and Kirill V Larin 2022 *Prog. Biomed. Eng.* **4** 012007

IOP Publishing Prog. Biomed. Eng. 4 (2022) 012007 https://doi.org/10.1088/2516-1091/ac4512

Progress in Biomedical Engineering

RECEIVED
31 March 2021

REVISED
6 September 2021

ACCEPTED FOR PUBLICATION
21 December 2021

PUBLISHED
14 January 2022

TOPICAL REVIEW

Wave-based optical coherence elastography: the 10-year perspective

Fernando Zvietcovich[1,2,*] **and Kirill V Larin**[1,*]

[1] University of Houston, Biomedical Engineering, Houston, TX 77204, United States of America
[2] Spanish National Research Council (CSIC), Daza de Valdes Institute of Optics, Madrid 28006, Spain
[*] Authors to whom any correspondence should be addressed.

E-mail: jzvietco@central.uh.edu **and** klarin@central.uh.edu

Keywords: elastography, review, wave propagation, optical coherence tomography, OCE

Abstract

After ten years of progress and innovation, optical coherence elastography (OCE) based on the propagation of mechanical waves has become one of the major and the most studied OCE branches, producing a fundamental impact in the quantitative and nondestructive biomechanical characterization of tissues. Preceding previous progress made in ultrasound and magnetic resonance elastography; wave-based OCE has pushed to the limit the advance of three major pillars: (a) implementation of novel wave excitation methods in tissues, (b) understanding new types of mechanical waves in complex boundary conditions by proposing advance analytical and numerical models, and (c) the development of novel estimators capable of retrieving quantitative 2D/3D biomechanical information of tissues. This remarkable progress promoted a major advance in answering basic science questions and the improvement of medical disease diagnosis and treatment monitoring in several types of tissues leading, ultimately, to the first attempts of clinical trials and translational research aiming to have wave-based OCE working in clinical environments. This paper summarizes the fundamental up-to-date principles and categories of wave-based OCE, revises the timeline and the state-of-the-art techniques and applications lying in those categories, and concludes with a discussion on the current challenges and future directions, including clinical translation research.

1. Introduction

Elastography, in the medical imaging perspective, is the functional modality that conveys information on the biomechanical properties of tissues. Among different mechanical parameters, elasticity has been proven to be an exciting biomarker not only for understanding physiological processes but also for the assessment of disease progression and treatment monitoring in various organs and tissues, including the ocular tunic, muscle, liver, brain, skin, and engineered tissues to name just a few [1–3]. Historically, elastography has been firstly implemented in imaging modalities such as magnetic resonance (MRE) [3] and ultrasound (USE) [1] (with millimeter-scale imaging resolution) demonstrating extensive capabilities in the generation of elasticity maps in 2D and 3D. Later on, the appearance of optical coherence tomography (OCT) as the light-based imaging method with micrometer spatial imaging resolution (∼3–10 μm) and depth penetration in the millimeter range (∼1–2 mm) made possible the first implementation of elastography in OCT, also named optical coherence elastography (OCE). Originally proposed by Schmitt *et al* [4] in 1998, OCE has rapidly evolved in the scientific community during the past decade with remarkable progress in the characterization of biomechanical properties of *ex vivo* and *in vivo* tissues, as reported by major review papers in years 2014 [5], 2015 [6], 2016 [7], 2017 [2], 2018 [8], and 2020 [9]. The underlying effort promoted a major advancement in answering basic science questions and improving medical disease screening in several types of tissues, ultimately leading to the first attempts of clinical trials and translational research [10–13].

Learning previous lessons from MRE and USE for the *in situ* and non-destructive elastography, OCE adopted the use of mechanical waves for the quantitative estimation of viscoelastic properties in soft tissues,

constituting today one of the major and most studied OCE branches, also named as wave-based OCE. The principal feature of OCT that makes elastography possible relies upon its ability to measure motion (displacement) with sub-nanometer sensitivity using the phase-sensitive OCT (PhS-OCT) approach [14]. Therefore, OCT generates not only structural images of a sample based on the light scattering produced by the different tissue distributions and boundaries but also provides sequences of displacement images along the time. This latter capability, ultimately, permits the measurement of quasi-static deformations and the tracking of mechanical waves within the same sample. Wave-based OCE was firstly implemented by Liang and Boppart [15] in 2010 and leveraged the connection between the speed of mechanical propagating waves with the viscoelastic properties of the material under study. Unlike quasi-static approaches where the elastic modulus of tissues is calculated by measuring its deformation produced by an exerted known force distribution [9], wave-based OCE allows for its quantitative elastography using only the motion field by assuming some *a priori* knowledge on boundary conditions of the tissue. This characteristic, together with the ability to generate waves using non-contact approaches, constitutes the major attraction towards developing this field.

Historically, shear waves have been the most desirable perturbations in wave-based elastography since shear waves speed (c_s) is related to the shear modulus and, making the proper assumptions, to the Young's modulus (E) which are important biomechanical parameters that have been used to characterize tissues in normal and pathological conditions. Moreover, shear wave speed in soft tissues is in the range of 0.1–50 m s^{-1} which does not impose a rigid restriction for imaging acquisition systems to capture wave propagation. The relationship between E, and c_s can be simplified for a uniform, elastic, homogenous and isotropic medium with density ρ and Poisson's ratio υ, as [1]:

$$c_s = \sqrt{E/2\rho(1+\upsilon)}. \tag{1.1}$$

This relationship has been further extended for more complex cases in which the medium is viscoelastic, anisotropic, and heterogenous by remodeling the fundamental equations that describe waves in elastic solids and calculating other wave parameters such as attenuation, speed dispersion, and direction-dependent speed. The use of shear waves was first leveraged by MRE [16] and USE [17] since these techniques can measure regions in tissues with dimensions much larger compared to the excitation wavelength. Then, shear waves can propagate farther away from the boundaries of the tissue boundaries at the speed shown in equation (1.1). However, in OCE, its millimeter penetration depth constrains the motion measurements to regions closer to the boundaries of tissues where surface acoustic waves (SAWs) are the dominant perturbations. Unlike pure transversal (shear waves) and pure longitudinal (pressure or acoustic waves) waves traveling in an elastic medium, SAWs have both transversal and longitudinal components of motion, it can be dispersive, and its speed is highly dependent on the boundary conditions of the media [18, 19]. A notable example in wave-based OCE demonstrating the importance of identifying the correct SAW propagating in tissues with complex boundary conditions is the cornea. As many studies reported before [8, 20, 21], the dominant perturbation in the cornea is called Lamb wave, and its speed not only depends on the shear/Young's modulus of the corneal tissue but also on the corneal thickness, excitation frequency, and acoustic properties of the neighboring coupling media, among other parameters. Then, interpreting changes of Lamb wave speed as uniquely related to changes in the elastic or shear moduli of corneal tissues is inaccurate and may lead to false conclusions.

In elastography, the most common assumptions made on tissues rely on their homogeneity, isotropy, elasticity, linearity, and incompressibility. Nevertheless, in reality, tissues exhibit far more complex biomechanical properties, including heterogeneous distributions (e.g. the corneoscleral boundary in the eye) [22], anisotropy (e.g. muscle or corneal tissue with a preferable orientation of fibers) [23, 24], viscoelasticity (e.g. liver and fat tissues producing strong dumping and attenuation of waves) [25], non-linearity (e.g. the increment of corneal rigidity when it is stretched) [26], and others. This biomechanical complexity, added to the challenges imposed by SAWs, encouraged the scientific community into the research of new analytical models of wave propagation and the development of estimators that can be used to reveal some of these parameters. Special attention is given to the capabilities of estimators in detecting smaller spatial elasticity gradients in tissues, which brings the concept of elastography resolution. In wave-based OCE, the increase of elastography resolution is primarily achieved by reducing the characteristic wavelength λ_c of the mechanical wave (or pulse spatial width for transient waves) is in tissues, and it is lastly limited by imaging resolution of the OCT system [27]. While axial and lateral imaging resolution of OCT ranges from 2 to 20 μm [28], wave-based elastography resolution tends to be in the millimeter scale in soft tissues [27, 29] due to the difficulty of reducing λ_c. As reported by numerous studies [27, 29], the reduction of λ_c can be achieved by increasing the temporal frequency content of the mechanical wave. Therefore, continuous efforts are invested

in the implementation of excitation sources capable of producing mechanical excitation in tissues at higher frequencies with enough displacement magnitude to be detected by OCT.

Finally, the development of excitation sources constitutes a fundamental pillar of wave-based OCE since the spatial and temporal source characteristics significantly limit the elastography resolution, while its coupling nature with the target tissues has a large influence on the types of mechanical waves generated. In the last decade, several excitation methods have been proposed [2, 8], and they can be classified by their physical nature (e.g. light-based, acoustic-based, air-based, electromagnetic-based, and displacement-based excitation), coupling properties (e.g. contact, and non-contact), spatial distribution (e.g. localized, and distributed sources), and temporal capabilities (e.g. transient, harmonic/quasi-harmonic, and multifrequency). The uses and attributes of each excitation method will depend on the boundary conditions, mechanical properties, and safety limits of the specific tissue under study. For instance, in the elastography of the ocular tissues, non-contact excitation methods are preferred in order to avoid possible damage, infection, and patient discomfort, which facilitates its translation for clinical use.

In this review, we describe the fundamental principles of wave-based OCE and summarize the ten-year progress in this field. In section 2, we review the main tissue mechanical properties using concepts of stress/strain and the types of boundary conditions typically found in OCE. In section 3, we conduct a taxonomical classification of the types of mechanical waves propagating in tissues according to their boundary conditions and mechanical properties, and we establish the relationship between wave speed and Young's/shear moduli. Later on, in section 4, we describe the types of excitation methods that generate these waves highlighting their physical nature and spatial-temporal characteristics. Motion detection in OCE, including notions of main OCT implementations and acquisition protocols, are discussed in section 5. In section 6, different elastography estimators that allow the 1D, 2D, and 3D quantitative imaging of mechanical properties of tissues leveraging various wave properties (e.g. group/phase speed, attenuation, and wavenumber) are described including the definition of elastography resolution in wave-based OCE. Most of the recent work in wave-based OCE is reviewed in section 7 in the context of the sample under investigation and categorized as: phantom studies, *ex vivo* studies, *in vivo* pre-clinical studies, and *in vivo* clinical studies. Furthermore, in section 8, we discuss the current main challenges of OCE in terms of resolution, acquisition speed, accuracy and repeatability of estimations, and feasibility for *in vivo* clinical implementations, underlying possible directions for future work. Finally, in section 9, we summarize the main progress of wave-based OCE in the past ten years, including information on how this OCE branch has been growing in terms of scientific productivity.

We apologize in advance if we have missed any significant publication in this review's content; we tried to be as throughout as possible.

2. Tissue mechanical properties and boundary conditions

In the field of elastography, the elastic properties of tissues can be understood as the relationship between the deformation (represented as strain ε) response produced by applied mechanical stress (σ). Then, a stiffer tissue will deform much less than a softer one under the same stress. This simple concept has been extensively used in medicine through the years in the palpation of tissues for the possible detection of tumors and other diseases. In this section, we aim to define the principal mechanical parameters probed in elastography for cases such as elasticity, viscoelasticity, anisotropy, and non-linear elasticity, and how these parameters are related to the components of the soft tissue microstructure.

2.1. Soft tissue microstructure

Pathological changes of tissues are often related to modifications in their consistency and histological microstructure which will further propagate in variations of mechanical properties at the macroscale level. At this scale, the extracellular matrix (ECM) and the active cells (e.g. fibroblasts in muscle tissue) are the two fundamental components, being the ECM the one providing integrity and support for the structural functionality of tissues [30]. Research has demonstrated that metrics derived from shear wave speed are potential biomarkers to assess changes of tumor microstructure principally affecting the ECM [31]. Therefore, the elements composing the ECM, including their interactions have an important role in its mechanical response. The ECM can be understood as a crosslinked network of collagen and elastin embedded in a gelatinous matrix of proteoglycans [32]. Following the dynamic strain–stress example of ECM under deformation proposed by Russ *et al* [30], in the absence of load ($\varepsilon = 0\%$), the symmetrical organization of the collagen fibers are in their natural state (loose and wavy) and it can be modeled as approximately isotropic (i.e. it strain–stress behavior is invariant to direction) at the microscale level. Then, when the soft tissue is stretched ($\varepsilon < 2\%$), the elastin fibers absorb most of the energy leading to an increase of the elastic modulus (i.e. non-linear elasticity effect). However, when ECM is further stretched,

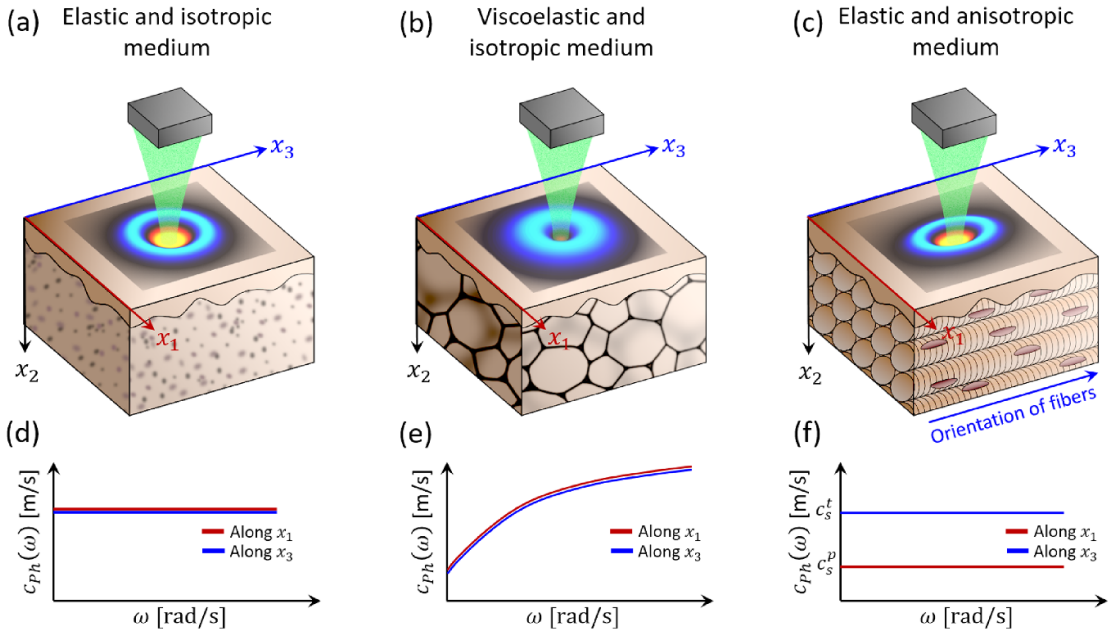

Figure 1. Characteristics of wave propagation produced by the same localized excitation device in homogeneous tissues with different mechanical properties: (a), (d) elastic and isotropic, (b), (e) viscoelastic and isotropic, and (c), (f) elastic and anisotropic. In (d), phase speed corresponding to (a) is not dispersive and is the same for any radial direction with respect to the excitation origin. In (e), phase speed is frequency-dependent, which produces spatio-temporal distortion and attenuation of wave propagation in (b). Nevertheless, the propagation in (e) is still isotropic with respect to the excitation origin. Finally, in (f), phase speed is non-dispersive but highly anisotropic with respect to the orientation of fibers in (c).

interfibrillar sliding is induced and collagen fibers start to line up along the loading direction which increases the elastic modulus at a preferable orientation (i.e. elastic anisotropy effect). Finally, the high fluid content of tissues combined with the poroelastic structure of the ECM produces a time-delayed deformation strain when a load is applied, which translates to energy dissipation and, seen at the macroscale, behaves as a viscoelastic solid. Therefore, the mechanical properties of the same tissue can be modeled differently depending on the components of its ECM and its response to deformation. Historically, elasticity has been assumed in soft tissues with unknown rheological behavior and because of the simplicity of the estimations; nevertheless, combined mechanical behavior has been reported in a variety of soft tissues including muscle and cardiac tissue [33, 34] (anisotropic and non-linear); liver [35, 36], breast [37], and prostate [38] (viscoelastic); cornea and sclera [22, 39, 40] (non-linear and anisotropic), to name just a few.

2.2. Elasticity

In a homogeneous, linear elastic, and isotropic medium (see figure 1(a)), the relationship between stress and strain in a 3D Cartesian space (x_1, x_2, x_3) is given by:

$$\begin{Bmatrix} \varepsilon_{11} \\ \varepsilon_{22} \\ \varepsilon_{33} \\ 2\varepsilon_{12} \\ 2\varepsilon_{13} \\ 2\varepsilon_{23} \end{Bmatrix} = \begin{bmatrix} 1/E & -\nu/E & -\nu/E & 0 & 0 & 0 \\ -\nu/E & 1/E & -\nu/E & 0 & 0 & 0 \\ -\nu/E & -\nu/E & 1/E & 0 & 0 & 0 \\ 0 & 0 & 0 & 1/\mu & 0 & 0 \\ 0 & 0 & 0 & 0 & 1/\mu & 0 \\ 0 & 0 & 0 & 0 & 0 & 1/\mu \end{bmatrix} \begin{Bmatrix} \sigma_{11} \\ \sigma_{22} \\ \sigma_{33} \\ \sigma_{12} \\ \sigma_{13} \\ \sigma_{23} \end{Bmatrix} \tag{2.1}$$

where, $\varepsilon_{ij}\,(i=j)$ is the infinitesimal normal strain; $2\varepsilon_{ij}\,(i\neq j)$ is the infinitesimal shear strain; σ_{ij} is the Cauchy stress in a finite-strain problem; and ν is the incompressibility modulus called Poisson's ratio in any ij-plane. Then, the elastic parameters of interest in OCE are: Young's modulus (E), which relates uniaxial strain and stress in the same direction $(i=j)$; and shear modulus (μ) which relates shear strain with stress in any ij-plane $(i\neq j)$. Then μ can be expressed in terms of E and ν as

$$\mu = E/2\,(1+\nu)\,. \tag{2.2}$$

Most tissues are considered incompressible (i.e. volume conservation when tissues are exposed to any load); therefore, we can use $\mathrm{Tr}\,(\varepsilon)=0$, and $\nu\approx 0.5$, leading to $\mu = E/3$. In wave-based OCE, the speed of shear waves (c_s) is related to the shear modulus μ and tissue density ρ as $c_s = \sqrt{\mu/\rho}$ (extended explanation in

section 3.1). Therefore, assuming a homogenous, isotropic, and linear elastic tissue, E can be calculated as well using equation (1.1). It is important to note the symmetry of equation (2.1) in which in E and μ are the same for any direction. Then, isotropic wave propagation along the x_1x_3-plane is produced when the motion is polarized along the x_2-axis (figure 1(a)) [19]. Therefore, c_s is the same along the x_1- and x_3-axes and constant for every excitation frequency as shown in figure 1(d). This condition will not hold for more complex cases such as anisotropic tissues (section 2.3).

2.3. Viscoelasticity

Up to this point, we have considered the shear modulus to be fully elastic (i.e. μ is a real number and $\mu > 0$); however, there is extensive evidence that tissues are viscoelastic [21, 25, 35, 38, 41–43], which means that μ is frequency-dependent and complex ($\tilde{\mu}(\omega)$) represented as:

$$\tilde{\mu}(\omega) = \mu_s(\omega) + i\mu_l(\omega), \tag{2.3}$$

where $\mu_s(\omega)$ and $\mu_l(\omega)$ are known as the storage modulus and loss moduli, respectively; and ω is the angular frequency ($\omega = 2\pi f$). We can extend the $c_s - \mu$ relationship from the elastic case to the complex version as

$$\widehat{c_s}(\omega) = \sqrt{\tilde{\mu}(\omega)/\rho}. \tag{2.4}$$

The complex shear wave speed $\widehat{c_s}(\omega)$ does not show a physical meaning itself until it is used in the wave equation solution $k = \omega/c_s$ as:

$$\tilde{k}(\omega) = \frac{\omega}{\widehat{c_s}(\omega)} = \frac{\omega}{\sqrt{\tilde{\mu}(\omega)/\rho}}. \tag{2.5}$$

Then, the frequency-depended wavenumber $\tilde{k}(\omega)$ can be represented in a complex form as [44]:

$$\tilde{k}(\omega) = \beta(\omega) - i\alpha(\omega) = \frac{\omega}{c_{Ph}(\omega)} - i\alpha(\omega). \tag{2.6}$$

In equation (2.6), the real part of $\tilde{k}(\omega)$ is related to the frequency-dependent phase velocity $c_{Ph}(\omega)$. The physical meaning of the imaginary part of $\tilde{k}(\omega)$ is related to the frequency-dependent attenuation of the shear wave when equation (2.6) is used in the complex exponential representation of a wave traveling along the positive side of the x_1-axis as:

$$u_{x_2}(x_1, t) = \frac{1}{{x_1}^N} e^{i\left(\omega t - \tilde{k}(\omega)x_1\right)} = \frac{1}{{x_1}^N} e^{i(\omega t - \beta(\omega)x_1)} e^{-\alpha(\omega)x_1}, \tag{2.7}$$

where $u_{x_2}(x_1, t)$ represents the displacement along the x_2-axis produced by a pure transversal wave traveling along the x_1-axis (or x_3-axis as the sample is considered isotropic in this derivation) as shown in figure 1(b). The first term on the right side of equation (2.7) represents the attenuation produce by the geometrical spreading of the wave in the far field when propagating along the x_1-axis. Then $N = 0$ for plane waves (no spreading), $N = 0.5$ for cylindrical waves, and $N = 1$ for spherical waves. The next term of equation (2.7) is the regular complex exponential representing wave propagation with speed controlled by $\beta(\omega)$, while the last term is the exponential decay of the wave amplitude produce by $\alpha(\omega)$ as the wave propagates toward the right side of the x_1-axis. In this treatment, we are agnostic on the frequency dependence mechanism of $c_{Ph}(\omega)$ and $\alpha(\omega)$; however, by choosing a constitutive model of the tissue and using the Kramers–Kronig relations, it is found that $c_{Ph}(\omega)$ and $\alpha(\omega)$ are linked to each other [45, 46].

The contributions of $\beta(\omega)$ and $\alpha(\omega)$ (equation (2.6)) in the storage and loss shear moduli (equation (2.3)), without any assumption of the viscoelasticity behavior of tissues, are described as [47, 48]:

$$\mu_s(\omega) = \rho\omega^2 \frac{\beta(\omega)^2 - \alpha(\omega)^2}{\left(\beta(\omega)^2 + \alpha(\omega)^2\right)^2} \tag{2.8a}$$

$$\mu_l(\omega) = 2\rho\omega^2 \frac{\beta(\omega)\alpha(\omega)}{\left(\beta(\omega)^2 + \alpha(\omega)^2\right)^2}. \tag{2.8b}$$

Then, in the case of elastic tissue where $\alpha(\omega) = 0$, then $\mu_l(\omega) = 0$, and the storage modulus only depend on the phase speed as $\mu_s(\omega) = \rho(\omega/\beta(\omega))^2 = \rho c_{Ph}(\omega)^2$. While $\mu_s(\omega)$ and $\mu_l(\omega)$ tend to be associated with the elastic and viscous part of the medium, and these definitions can only be interpreted when using a rheological model. Several rheological models have been proposed in elastography for the adequate modeling

of viscoelastic tissues [43]. One of the most used models in wave-based OCE is the Kelvin–Voigt model. This model simulates the elastic and viscous part of the medium with a spring (G_0 parameter) and dashpot (η parameter), respectively, arranged in parallel [43]. Then, the complex shear modulus is represented as:

$$\tilde{\mu}(\omega) = G_0 + i\omega\eta. \tag{2.9}$$

Using equations (2.8*a*) and (2.8*b*) in equation (2.9), $c_{\mathrm{Ph}}(\omega)$ and $\alpha(\omega)$ can be found as [43]:

$$c_{\mathrm{Ph}}(\omega) = c_0\left[\frac{1}{2}\frac{1}{1+\frac{\omega^2}{\omega_0^2}}\left(\sqrt{1+\frac{\omega^2}{\omega_0^2}}+1\right)\right]^{-1/2}, \tag{2.10}$$

$$\alpha(\omega) = \frac{\omega}{c_0}\left[\frac{1}{2}\frac{1}{1+\frac{\omega^2}{\omega_0^2}}\left(\sqrt{1+\frac{\omega^2}{\omega_0^2}}-1\right)\right]^{1/2}, \tag{2.11}$$

where $c_0 = \sqrt{G_0/\rho}$, and $\omega_0 = G_0/\eta$. Then, $c_{\mathrm{Ph}}(\omega)$ and $\alpha(\omega)$ are frequency-dependent, and parameters G_0 and η can be found by using either equations (2.10) and (2.11). If frequency-dependent data is not available, and c_{Ph} and α are only measured for a single frequency, both equations (2.10) and (2.11) are needed to calculate G_0 and η. Therefore, the effect of viscoelasticity (using this particular rheological model) in mechanical wave propagation is speed dispersion, as shown in figure 1(e), and attenuation, which both can highly dump and distort the propagation of transient pulses in tissues (see the wave pattern in figure 1(b)). Other models have also been proposed in USE [38, 43, 49] and wave-based OCE [8, 21, 25, 48, 50–53], including the Voigt, Maxwell, Kelvin–Voigt fractional derivative, and standard linear solid. In section 6, we will discuss estimators capable of measuring phase speed dispersion ($c_{\mathrm{Ph}}(\omega)$) and wave attenuation ($\alpha(\omega)$) from the spatio-temporal wave propagation, which, together with equation (2.8), are used to calculate $\mu_{\mathrm{s}}(\omega)$ and $\mu_{\mathrm{l}}(\omega)$.

2.4. Elastic anisotropy

In section 2.1, we assume that tissues are elastic, homogeneous, and isotropic; nevertheless, in reality, the distribution of many tissues breaks this assumption. For example, skeletal muscle cells are long and tubular with a preferable direction of alignment; therefore, muscle is considered an anisotropic medium, which has implications in the relationships between E and μ for specific direction and planes in the 3D space. Consequently, the wave speed will be affected by the direction in which the mechanical wave is propagating and its displacement polarization.

A special case of anisotropy in the transverse isotropic model in which the material is mechanically symmetric with respect to one selected direction (e.g. the direction of the fiber alignment in the skeletal muscle example). We will call this direction the axis of symmetry. Then, the elastic material exhibits isotropic behavior only at every plane perpendicular to the axis of symmetry (i.e. the plane of isotropy). For the purpose of this explanation, we choose x_3 as the axis of symmetry, and the x_1x_2-plane as the plane of isotropy, as shown in figure 1(c). Similar to the elastic case, we can represent the relationship between the 3D strain (ε) and stress (σ) as:

$$\begin{Bmatrix} \varepsilon_{11} \\ \varepsilon_{22} \\ \varepsilon_{33} \\ 2\varepsilon_{12} \\ 2\varepsilon_{13} \\ 2\varepsilon_{23} \end{Bmatrix} = \begin{bmatrix} 1/E_{\mathrm{p}} & -\nu_{\mathrm{p}}/E_{\mathrm{p}} & -\nu_{\mathrm{tp}}/E_{\mathrm{t}} & 0 & 0 & 0 \\ -\nu_{\mathrm{p}}/E_{\mathrm{p}} & 1/E_{\mathrm{p}} & -\nu_{\mathrm{tp}}/E_{\mathrm{t}} & 0 & 0 & 0 \\ -\nu_{\mathrm{pt}}/E_{\mathrm{p}} & -\nu_{\mathrm{pt}}/E_{\mathrm{p}} & 1/E_{\mathrm{t}} & 0 & 0 & 0 \\ 0 & 0 & 0 & 1/\mu_{\mathrm{p}} & 0 & 0 \\ 0 & 0 & 0 & 0 & 1/\mu_{\mathrm{t}} & 0 \\ 0 & 0 & 0 & 0 & 0 & 1/\mu_{\mathrm{t}} \end{bmatrix} \begin{Bmatrix} \sigma_{11} \\ \sigma_{22} \\ \sigma_{33} \\ \sigma_{12} \\ \sigma_{13} \\ \sigma_{23} \end{Bmatrix} \tag{2.12}$$

where, $E_{\mathrm{p}} = E_1 = E_2$, and $E_{\mathrm{t}} = E_3$ corresponding to the Young's modulus in the plain of isotropy (p), and along the axis of symmetry (t), as a function of the three moduli E_1, E_2, and E_3 in the principal directions x_1, x_2, and x_3, respectively. Similarly, $\nu_{\mathrm{tp}} = \nu_{31} = \nu_{32}$, $\nu_{\mathrm{pt}} = \nu_{13} = \nu_{23}$, and $\nu_{\mathrm{p}} = \nu_{12} = \nu_{21}$ are the Poisson's ratios as a function of ν_{ij}, which characterizes the transverse strain in the j-direction when the material is stressed in the i-direction. Finally, $\mu_{\mathrm{p}} = \mu_{12} = E_{\mathrm{p}}/2\left(1+\nu_{\mathrm{p}}\right)$, and $\mu_{\mathrm{t}} = \mu_{13} = \mu_{23}$ are the shear modulus in the plane of isotropy and in transverse planes parallel to the axis of symmetry, respectively.

Unlike the isotropic case, the relationship between μ_{p}, E_{p}, and ν_{p} parameters (equation (2.2) in the isotropic case) is only valid for the plane of isotropy, leaving the E_{t}, μ_{t}, and ν_{tp} as independent unknown variables, assuming that the medium is incompressible [54]. In wave-based OCE, μ_{p} and μ_{t} are responsible parameters to define the speed of shear waves. Two canonical cases can be identified. In the first case, shear waves travel parallel to the x_1x_2-plane of isotropy with displacement mainly polarized along the axis of

symmetry x_3. Then, when the wave travels along x_1 direction, the medium is sheared in the x_1x_3-plane and the wave speed is related to the shear modulus $\mu_t = \mu_{13}$. Similarly, if the wave travels along x_2, the medium is sheared in the x_2x_3-plane and the wave speed is related to the shear modulus $\mu_t = \mu_{23}$. Therefore, the wave speed is isotropic (i.e. same speed along any direction) within the plain of isotropy and is defined by

$$c_s^t = \sqrt{\mu_t/\rho}. \tag{2.13}$$

The second canonical case is defined when the wave travels in any transverse plane perpendicular to the plane of isotropy. Then, the displacement produced by the wave is mainly polarized perpendicular to the axis of symmetry. If we define x_1x_3-plane as the transverse plane, then the displacement is polarized along the x_2-axis as shown in figure 1(c). When the propagation direction is along x_1 (perpendicular to the axis of symmetry), the material is being mechanically sheared along the x_1x_2-plane associated with shear modulus $\mu_p = \mu_{12}$. Then, the wave speed is defined as:

$$c_s^p = \sqrt{\mu_p/\rho}. \tag{2.14}$$

On the other hand, when the wave propagates along x_3 (parallel to the axis of symmetry), the material is being sheared along the x_2x_3-plane, associated with shear modulus $\mu_t = \mu_{23}$. Then, the wave speed is the same as in equation (2.13). In summary, the wave speed in the x_1x_3-plane is anisotropic, and it has an elliptical shape (see the wave pattern in figure 1(c)) defined as [55]:

$$c_s(\theta) = \sqrt{\left(c_s^p \cos\theta\right)^2 + \left(c_s^t \sin\theta\right)^2}, \tag{2.15}$$

where the angle θ is defined with respect to x_1-axis.

In summary, the shear wave speed in any direction within a transverse isotropic tissue can be defined as a linear combination of the two canonical cases shown in equations (2.13) and (2.14). The assessment of c_s^p and c_s^t (where $c_s^t > c_s^p$ in the example of figure 1(f)) has been characterized before in USE, MRE, and numerical simulation [54–60]. Later, it was further extended in wave-based OCE in a variety of tissues, including skeletal muscle [61] and other more complex boundary conditions such as cornea [23, 62].

2.5. Non-linear elasticity

Previously, the Young's (or shear) modulus has been defined as a constant for the elastic case, or frequency-dependent for the viscoelastic case; however, in elastography, the dependence of E with respect to the strain ε (or deformation) imparted in tissues has been documented in muscle [33], cornea [62], sclera [22], and other soft tissues. Then, the strain–stress relationship is non-linear, and the Young's and shear moduli can be described as $E(\varepsilon)$, and $\mu(\varepsilon)$. In the context of wave-based OCE, the dynamic displacements produced in tissues under constant tension for the generation of waves tend to be in the submicron range, which constrains $E(\varepsilon)$, and $\mu(\varepsilon)$ to the very initial linear region (low ε) and it does not impose a problem in the repeatability of measurements. On the other hand, if tissues are subject to an external variable tension (or compression), OCE measurements will be able to probe $E(\varepsilon)$, and $\mu(\varepsilon)$ for different strain scenarios, which can be instrumental for the understanding of tissue function and biomechanics [22, 62].

2.6. Tissue spatial distribution and boundary conditions

The relationship between Young's modulus and shear wave speed in equation (1.1) constitutes the keystone in elastography. This relationship was obtained assuming a shear wave propagating in an elastic, isotropic, homogenous infinite-type media. Aside from anisotropy and viscoelasticity that were discussed in the previous sections, tissues can also be heterogeneous, and they have distributions and boundary conditions far more different than the initial assumption. Figure 2 shows a variety of tissues exhibiting different distribution and boundary conditions. For instance, skin can be considered a layered medium consisting of epidermis, dermis, and subcutaneous layers, each with different elasticities and thicknesses. Furthermore, the cornea can be considered as a layered thin-plate interacting with fluid in the posterior surface. In both cases, there is a top coupling media between the OCT probe and the tissue under measurement, which is typically air (or fluid for other cases where the excitation method or the tissue conditions require it) as shown in the left column of figure 2. In all these cases, the wave propagation phenomenon will be affected, and other branches of mechanical waves, such as SAWs or Lamb waves, depending on the tissue structure, will more likely to propagate [19, 63].

Tissue distribution and boundary conditions can be classified by infinite, semi-infinite, thin-plate, layered, and heterogenous, as seen by a characteristic wavelength (λ_c) of the propagating mechanical wave. Even though tissues can be described by combinations of more than one case and exhibit far more

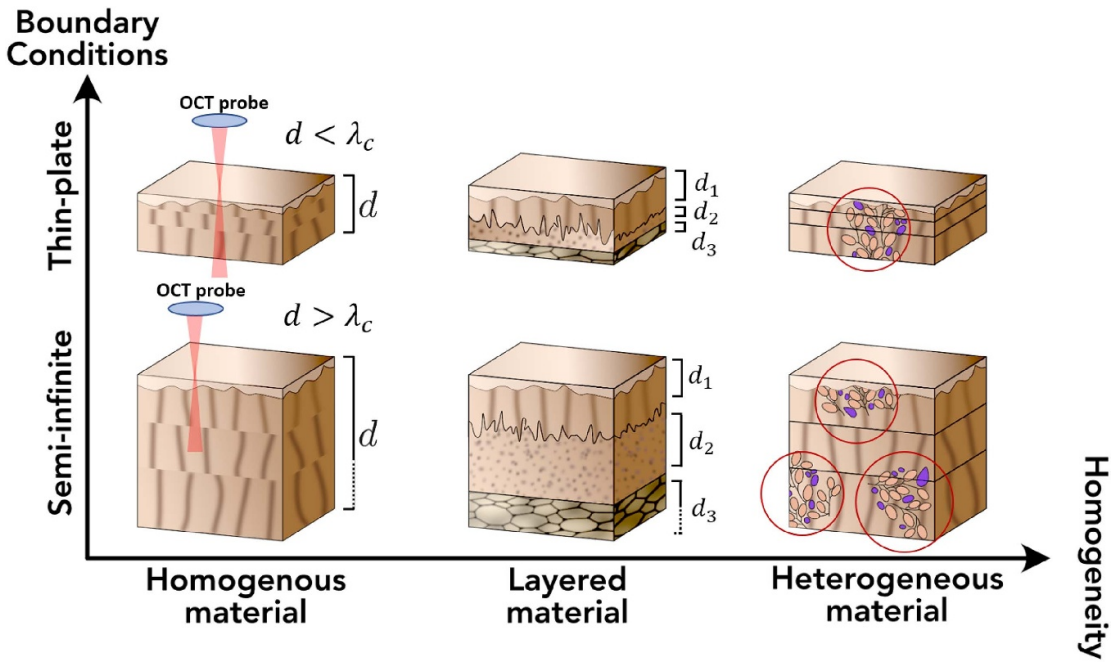

Figure 2. Tissue spatial distribution and boundary conditions with respect to the characteristic wavelength λ_c of the mechanical wave propagating in the tissue. In the horizontal axis, three categories of homogeneity are shown: homogeneous (with thickness d), layered (with different thickness for each layer), and heterogeneous (with softer and/or stiffer inclusions compared to the background) materials. In the vertical axis, two categories of boundary conditions are shown: semi-infinite, when $d > \lambda_c$; and thin-plate type media, when $d > \lambda_c$. In all cases, we assume the tissues are low-viscosity media and extend infinitely along the lateral directions.

complicated distribution, the proposed classification is useful for understanding the different branches of mechanical waves measured in wave-based OCE.

2.6.1. Infinite media

This case can be approximated to a medium with dimensions much larger than λ_c of the propagating wave. Similarly, this case is considered homogenous, which means that any inhomogeneity (localized inclusions with different elasticities than the background) is much smaller than λ_c. Finally, infinite media does not account for borders with external boundary conditions; therefore, pure body waves, such as shear and pressure waves, and longitudinal shear waves (LSWs) (detailed explanation in sections 3.1 and 3.2) are more likely to propagate. This type of assumption of tissues can be achieved in MRE and USE since they have a larger imaging field of view capable of measure deeper in tissues such as the human breast, kidney, and liver.

2.6.2. Semi-infinite media

Similarly to the previous case, semi-infinite media is characterized by a medium with dimensions much larger than λ_c of the propagating wave, but with the presence of a border delimiting the beginning of the elastic medium, which can be subjected to different boundary conditions (see the bottom element in the left column in figure 2). This case also considers homogeneity (local inclusions are much smaller than λ_c) in the elastic region. Semi-infinite media can support the propagation of pure body waves, and LSWs, and SAWs (detailed explanation in sections 3.1–3.3). This type of assumption of tissues is typically achieved with OCT since its imaging penetration is in the millimeter range. Examples of semi-infinite tissues are *ex vivo* biopsy samples extracted from larger organs such as the liver, brain, and muscle.

2.6.3. Thin-plate media

This type of media is characterized by a thickness with dimensions comparable to λ_c of the propagating wave (see the top element in the left column in figure 2). Therefore, there are two borders, delimiting the beginning and the end of the elastic medium, which can be subjected to different boundary conditions. This case also considers homogeneity (local inclusions are much smaller than λ_c) in the elastic region. Thin plates frequently support Lamb waves (detailed explanation in sections 3.4), and they can be imaged by OCT. Typical tissue example are tendons, cornea, and sclera (assuming λ_c much larger than the layer thicknesses within the thin-plate).

2.6.4. Layered media

This case takes effect when the thicknesses of two or more layers (with different elasticities) distributed horizontally (along the lateral extend) or vertically (along with the depth) are much smaller than λ_c of the propagating wave. Layered configuration can be added to semi-infinite media (e.g. skin tissue depicting epidermis, dermis, and subcutaneous layers), or thin-layer media (e.g. cornea showing layers such as epithelium, stroma, and endothelium) as shown in the bottom and top elements in the center column of figure 2, respectively. Layered media often support Love waves [64], which are guided by the borders in between consecutive layers and reported in seismic studies; however, up to date, there is no experimental evidence of them in wave-based OCE. In addition, there are reports of mixtures of other wave branches in this type of media, such as shear [65], SAWs [25], and Lamb waves [20] when λ_c is reduced.

2.6.5. Heterogeneous media

In this case, localized inclusions with variable shapes and different elasticities compared to the background have dimensions comparable to the characteristic wavelength λ_c of the propagating wave. Similar to the layered media, heterogeneity can be added to all other previous media cases, as shown in the third column of figure 2. Examples of this medium include disease conditions such as the presence of stiffer tumors in the liver or brain, skin carcinoma, localized anomalies in the cornea, etc. All types of waves can propagate in this media depending on the assigned boundary conditions explained in the previous cases.

3. Types of mechanical waves in tissues

A mechanical wave is generated when a disturbance (also called excitation) is produced in an elastic medium and spreads or transmits to other regions of the same medium. Such effect is also called wave propagation, and its speed is ultimately related to the intrinsic properties of the material and boundary conditions of the medium. In the context of OCE in tissues, the generation of waves is typically conducted within and beneath the surface of tissues (typically 1–3 mm due to the absorption of infrared light in tissues [66]) produced by an excitation source, and displacement (or particle velocity) is measured along the axial direction (z-axis) as shown in figure 3(a). The distribution of waves generated when a harmonic axial load is applied to the surface of a semi-infinite elastic and isotropic solid, as discussed by Graff [19] is shown in figure 3(b). Each wave can be classified according to its propagation direction, displacement polarization, and speed properties. In wave-based OCE, four major wave branches are generated and measured for the elastic characterization of tissues among different boundary conditions and excitation properties: body waves (those are shear and compression waves in figure 3(b)), LSWs, and SAWs (that can be Rayleigh/Scholte, or Lamb waves depending on the coupling media and boundary conditions).

3.1. Body waves

Body waves are also known as bulk waves, and they can be: pure longitudinal, when particle velocity (displacement) is parallel to the direction of propagation, and pure transversal when the particle velocity is perpendicular to wave propagation direction. Body waves are independent of boundary conditions as the relationship between wave speed and mechanical properties of the medium where they propagate is straightforward. The pure transversal wave is also known as shear wave or S-wave, and its speed (c_s) is determined by the shear modulus (μ) and density (ρ) of the medium [19]:

$$c_s = \sqrt{\mu/\rho}. \tag{3.1}$$

Figure 3(b) shows shear waves propagating with the strongest energy towards oblique angles, also called the shear window. Shear waves are the keystone of elastography, and they were especially leveraged by MRE and USE due to the large field of view capabilities of these imaging modalities. Nevertheless, in OCE, such waves are very difficult to measure due to the effect of the surface of tissues. Generally, in homogeneous, isotropic, and linear elastic solids, the relationship between shear and Young's modulus is tied to the Poisson's ratio as:

$$\mu = E/2\,(1+\upsilon)\,. \tag{3.2}$$

Using this relationship together with equation (3.1) gives birth to equation (1.1). Later on, in section 2.3, we will see that this relationship is not valid anymore for anisotropic tissues.

The pure longitudinal wave is also known as pressure wave (P-wave) or acoustic wave, and its speed (c_p) is related to the p-wave modulus (M) and density of the material as:

$$c_p = \sqrt{M/\rho}. \tag{3.3}$$

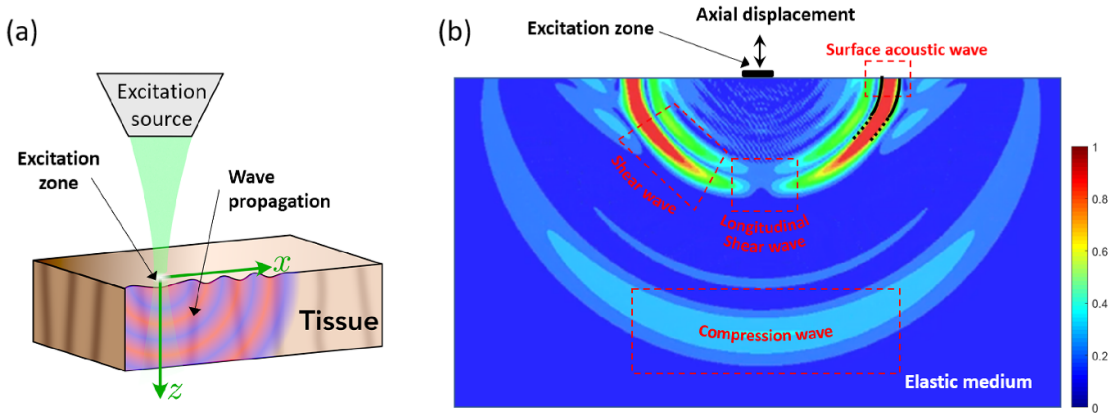

Figure 3. Mechanical waves in OCE. In (a), axial motion at the surface of a tissue sample is produced by an excitation source for the generation of mechanical wave propagation. (b) Numerically simulated diagram depicting different mechanical wave branches generated when an axial harmonic load is applied at the surface of a semi-infinite elastic medium. Four waves are identified: surface acoustic wave (traveling along the surface), shear wave, compressional wave and LSW (both traveling towards depth). Colormap represent normalized displacement magnitude in arbitrary units.

The P-wave modulus can be represented in terms of the bulk modulus K (or modulus of incompressibility), and the shear modulus μ as $M = K + 4\mu/3$ [19]. Figure 3(b) shows the acoustic wave as the primary perturbation propagating radially with respect to the loading point and faster than other wave branches. Biological soft tissues are mostly composed of water (considered nearly incompressible: $\upsilon \approx 0.5$) with K in the range of 2–3 GPa, and Young's modulus in the range of 0.1 kPa–30 MPa [67]. Then, assuming the tissues are isotropic, from equation (3.2), we have that μ roughly ranges from 30 Pa to 10 MPa, which is less than 1% of K. Therefore, as $K \gg \mu$, P-wave speed in tissues is mostly dominated by K in the range of 1400–1700 m s^{-1} [67]. Acoustic waves are not typically measured in OCE since they travel faster than typical OCT acquisition speed with lower displacements. On the other hand, shear wave speeds in soft tissues are in the range of 0.1–50 m s^{-1}, which can be captured and used in OCE. Recent developments in the Brillouin optical microscopy [68] are able to characterize bulk modulus K of tissues with interesting applications in the treatment monitoring of corneal therapies [69]. There are also studies that demonstrate log-log relationship between Brillouin shift and μ that could potentially be used for quantitative elastography (see, for example [70–72]). Nevertheless, it is important to highlight the strong sensitivity of Brillouin measurements to K, rather than μ [73].

3.2. LSWs

While pressure waves produce compression and extension of the medium and they satisfy the curl-free solution of the electrodynamic equation, shear waves, on the contrary, do not produce volumetric changes as they are divergence-free [74]. LSWs are a special case of transient shear waves that are both divergence- and curl-free, and they have been theoretically studied in [74, 75]. Therefore, such waves do have not only transversal but also longitudinal components of motion. When the surface of an elastic medium is excited with force/displacement perpendicular to such surface (axial motion in figure 3(b)), LSWs are generated and travel towards depth with interesting properties for OCE: they have a longitudinal (axial) component of motion detectable by OCT, and they travel at the shear wave speed (not being guided by the sample's surface as in SAW). In recent years, this type of waves have been leveraged by OCE for the characterization of tissue-mimicking phantoms and biological tissues *ex vivo* [76–82].

3.3. Rayleigh/Scholte waves

Rayleigh and Scholte waves are types of SAWs that propagate at the boundary of an elastic solid interfacing with a vacuum (or air-material as shown in figure 4(a)), and fluid (e.g. liquid-material as shown in figure 4(b)), respectively. These waves, unlike shear or compression waves, have longitudinal and transversal components of motion, are guided by the surface of the medium, are confined close to the surface (with an effective depth inversely proportional to the excitation frequency), and their speed is dependent on the characteristics of the elastic solid and coupling media. For a homogeneous, isotropic, linear-elastic, and nearly incompressible ($\nu \approx 0.5$) solid, the Rayleigh wave speed (c_R) travels at [18]:

$$c_R \approx 0.955\sqrt{\mu/\rho}, \tag{3.4}$$

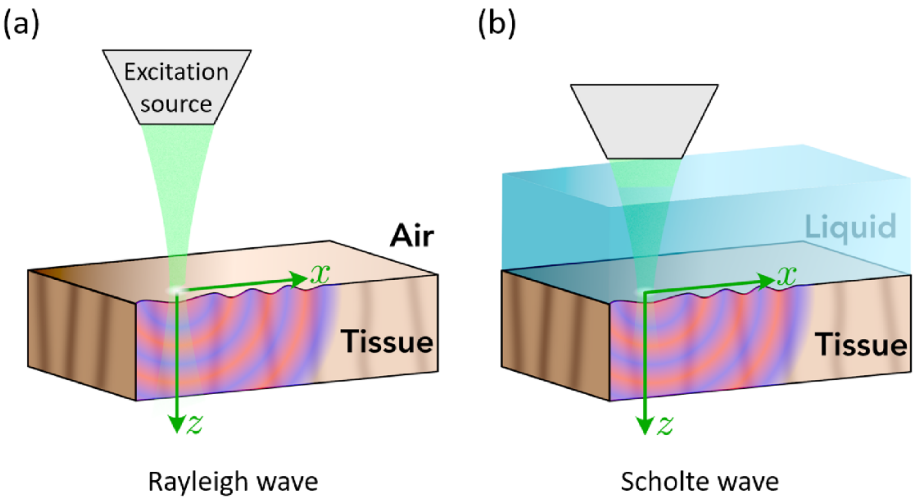

Figure 4. Generation of surface acoustic waves in a semi-infinite type tissue when the surface of the tissue is interfacing (a) air, and (a) liquid fluid. The excitation source is producing localized axial displacement at the tissue surface in both cases. After excitation, (a) Rayleigh, and (b) Scholte waves propagate guided by the tissue surface.

which has a similar relationship (95% of the shear wave speed) with the shear modulus μ as in equation (3.1). On the other hand, Scholte wave speed (c_{Sc}) travels at [18]:

$$c_{Sc} \approx 0.846\sqrt{\mu/\rho}, \tag{3.5}$$

which represents 84% of the shear wave speed using the same assumptions for the elastic medium.

Both SAWs are not dispersive (i.e. the wave speed is not frequency-dependent for an elastic and homogeneous medium), and decay as $1/\sqrt{r}$ when they propagate radially away from a localized source. In wave-based OCE, Rayleigh waves are the most common measured wave due to the presence of air-material as the coupling media between tissues and the OCT imaging probe. However, certain tissues, when measured *in vivo*, are surrounded by fluid (such as crystalline lens and retina inside the eye): therefore, the correct model should be utilized to avoid overestimations of the shear modulus μ.

3.4. Lamb waves

Lamb waves are perturbations that propagate in a medium with a thickness in the same order of magnitude as the characteristic wavelength of the mechanical wave (thin-plate type medium) as shown in figure 5(a). These waves are typically dispersive (i.e. there exists a frequency-dependence of the wave speed for elastic material), they are guided by the surface of the elastic plate, and they have multiple propagation modes distributed in different symmetric and antisymmetric orders [18, 19]. The speed of Lamb wave (c_L) is not only dependent of the body wave speeds c_p and c_s of the elastic medium, but also in the excitation frequency ($\omega = 2\pi f$), thickness of the plate (H), and the acoustic properties of the medium at the interphase of the top and bottom layer of the elastic plate. The Lamb wave speed cannot be represented in an explicit form as equation (3.1), but it can be solved numerically. Solutions to the Lamb wave speed have been proposed when the interphase medium is air or vacuum [18], fluid [83], and with mixed boundary conditions: top surface coupled with air, bottom surface coupled with fluid [21], as shown in figure 5(a).

The cornea is the biological tissue that can be considered as a thin plate with mixed boundary conditions as described in [21]. Then, the Lamb wave speed can be found by solving the non-trivial roots of $\det(\Lambda) = 0$, with Λ as [21]:

$$\Lambda = \begin{bmatrix} (k^2+\beta^2)\sinh(\alpha H/2) & 2k\beta\sinh(\beta H/2) & (k^2+\beta^2)\cosh(\alpha H/2) & 2k\beta\cosh(\beta H/2) & 0 \\ 2k\alpha\cosh(\alpha H/2) & (k^2+\beta^2)\cosh(\beta H/2) & 2k\alpha\sinh(\alpha H/2) & (k^2+\beta^2)\sinh(\beta H/2) & 0 \\ -(k^2+\beta^2)\sinh(\alpha H/2) & -2k\beta\sinh(\beta H/2) & (k^2+\beta^2)\sinh(\alpha H/2) & 2k\beta\cosh(\beta H/2) & \rho_F\omega^2/(\rho {c_s}^2) \\ 2k\alpha\cosh(\alpha H/2) & (k^2+\beta^2)\cosh(\beta H/2) & 2k\alpha\sinh(\alpha H/2) & -(k^2+\beta^2)\sinh(\beta H/2) & 0 \\ \alpha\cosh(\alpha H/2) & k\cosh(\beta H/2) & -\alpha\sinh(\alpha H/2) & -k\sinh(\beta H/2) & -\alpha_F \end{bmatrix}, \tag{3.6}$$

where $k = \omega/c_L$, $\alpha^2 = k^2 - \omega^2/{c_p}^2$, $\beta^2 = k^2 - \omega^2/{c_s}^2$, and μ is the shear modulus of the plate. The properties of the coupling fluid are defined as: ρ_F is the density of the fluid (typically ~1000 kg m^{-3}), c_p is the acoustic wave speed in the fluid (typically ~1500 m s^{-1}), and ${\alpha_F}^2 = k^2 - \omega^2/{c_F}^2$.

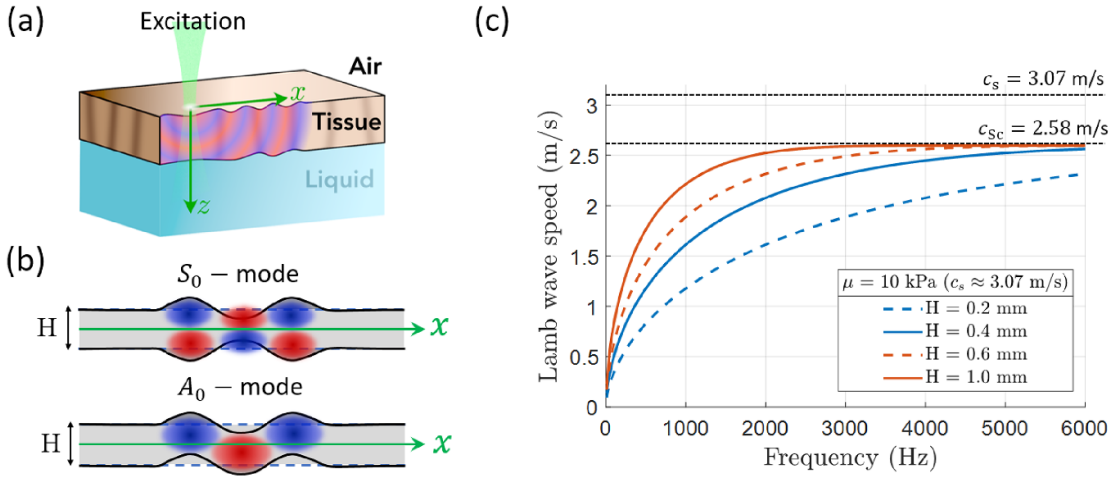

Figure 5. Propagation of Lamb waves in tissues. (a) Thin-plate type tissue (interfacing air at the top and liquid fluid at the bottom) being locally excited with axial motion at the top surface. (b) Lamb waves are generated and guided by the thin-plate in the quasi-symmetric (S_0) and quasi-antisymmetric (A_0) zero-order modes. Red and blue fields represent positive and negative displacement, respectively. (c) A_0 mode solution of equation (3.6) showing frequency-dependent Lamb wave speed for different thin-plate thicknesses H. For all cases, $c_p = c_F = 1500$ m s^{-1}, $\rho = \rho_F = 1000$ kg m^{-3}, $\mu = 10$ kPa, which produces a $c_s \approx 3.07$ m s^{-1}. The asymptotic Scholte wave speed (c_{Sc}) was calculated using equation (3.5).

The solution of $\det(\Lambda) = 0$ have two entire families of wave mode sets called symmetric and antisymmetric order mode solutions [18]. Unlike the infinite media case in which only two wave modes are possible (longitudinal and shear waves), in thin-plate bounded media, the number of mode solutions per family is infinite. Solutions of $\det(\Lambda) = 0$ can be found numerically by assuming that acoustic properties and densities of the elastic plate and fluid are the same: $c_p = c_F$, and $\rho = \rho_F$. The A_0 mode, also called flexural or bending mode, produces antisymmetrical displacement in the thin-plate with respect to its midplane ($z = 0$) as shown in figure 5(b). On the contrary, S_0 mode, also known as extensional mode, produces symmetric with respect to the midplane of the thin-plate (figure 5(b)). In practical applications, both S_0 and A_0 are perturbations typically generated and measured since they exist at all frequencies, and carry more energy than higher-order modes [18]. In wave-based OCE, experimental evidence shows that A_0 is the most common vibration mode in corneal plate-type tissues carrying most of the energy [21, 25, 65]; however, other studies also demonstrated the presence of other mode solutions [23, 84]. In this section, we are going to focus on the A_0 order mode solution which has been extensively used for the elastography of thin-plate type tissues.

In the A_0 solution of equation (3.6), the relationship between the Lamb wave speed c_L with the shear wave speed c_s (which provides μ), the thickness of the plate (H), and angular excitation frequency ω is determined as shown in figure 5(c). Here, we can call it quasi-antisymmetric zero-mode (A_0) solution since the boundary conditions of the plate is hybrid (air and water boundaries) rather than uniform in a typical Lamb wave. In figure 5(c), it is shown the frequency-dependent Lamb wave speed curves for different plate thicknesses with the same material's shear modulus ($\mu = 10$ kPa). Therefore, not taking into account the Lamb wave model for a specific plate thickness and excitation frequency will result in misleading interpretations of the material elasticity.

In contrast to other solution orders of symmetric and antisymmetric modes, in A_0 the asymptotic behavior of c_L tends to converge at the Scholte wave speed c_{Sc} when higher frequencies are reached. Moreover, the thinner the plate is, the slower is the convergence of the Lamb speed to c_{Sc} as shown in figure 5(c). Then, the estimation of μ can be achieved by either fitting the A_0 (or any other order) solution to the frequency-dependent Lamb wave speed with known thickness parameter, or by assuming convergence to the Scholte wave speed (typically valid for higher excitation frequencies). A special case of the Lamb wave propagation model is the one recently proposed by Pitre *et al* [23], in which the elasticity of the thin-plate material is considered as transverse isotropic (section 2.3) and applied for the anisotropic characterization of corneal elasticity using both zero-order symmetric and antisymmetric solutions.

4. Excitation sources and their classification

As explained in the previous section, mechanical waves are generated after a localized disturbance (force/displacement) is applied to the elastic medium under study. Different mechanical excitation methods

have been proposed during the last ten-year progress of wave-based OCE, and they can be classified by their physical nature (light-based, acoustic-based, air-based, electromagnetic-based, and displacement-based excitation), coupling properties (contact, and non-contact, and passive-intrinsic methods), spatial distribution (single, and multiple sources), and temporal capabilities (transient, quasi-harmonic, harmonic excitation), as shown in the diagram of figure 6. The spectral bandwidth of the waves produced by any selected excitation source is fundamental for defining the resolution of the OCE technique (further discussion of OCE resolution in section 6.5), and the selection of the most adequate elastography estimator. Besides the physical mechanism and coupling properties of the excitation, the spectral bandwidth of the generated motion will depend on the spatial extent and temporal shape of the excitation source.

4.1. Physical mechanism and coupling properties

The physics behind each excitation method proposed in OCE has a direct impact on the efficiency relationship between the input excitation energy and the output force/displacement generated in tissues. Understanding the mechanism in which each method produces motion is fundamental to determine if it complies with the safety standards required in clinical applications [85, 86]. They can be classified by light-based, acoustic-based, air-based, electromagnetic-based, and displacement-based stimulation, and each of them requires a different coupling medium between the stimulator and the tissue. The coupling properties will ultimately define if an excitation method is considered contact or non-contact with respect to the target tissue. In this section, we describe the most common excitation methods used in wave-based OCE.

4.1.1. Displacement contact

This method is based on the localized generation of displacement in tissues produced by the direct contact to a vibration source. It was early adopted by MRE [16] and USE [1, 17] for the generation of transient and harmonic excitation using pneumatic-, electromechanical- and piezoelectric-based excitation. Liang and Boppart [15] proposed the use of an electromechanical shaker for wave propagation generation in OCE for the first time, constituting the first application of a displacement excitation and, more generally, the first wave-based OCE paper. Later on, wave-based OCE adopted the use of piezoelectric actuators fixed to different mountings that will be in contact to the surface of tissues for the generation of localized [25, 29, 87], extended [76, 78], and distributed [65] wave propagation. Displacement-based excitation using piezoelectric actuators can produce large bandwidth (for transient excitation) and high frequency (for harmonic excitation) motion, stronger and localized displacements (in the order of μm), and allows to shape the displacement with a diverse variety of arbitrary time signals such as Gaussian and Bessel pulses, modulated, chirped and harmonic signals. Depending on the distribution of the contact tips and the time characteristics of the motion signal, different types of waves (e.g. SAW, shear, longitudinal shear, and Lamb waves) and wave interferences (standing waves, crawling waves, or reverberant fields) can be generated (extended development in section 4.2.2). Finally, this type of excitation is considered a contact method, and it could be problematic for the elastography of delicate tissues such as the cornea and the sclera due to the potential damage and discomfort. Nevertheless, a recent study of wave-based OCE using a contact probe with a spherical tip for the elastography of *in vivo* human cornea [12] demonstrated no irreversible damage of epithelial cells in the corneas of 12 volunteers.

4.1.2. Acoustic radiation force (ARF)

The use of concentrated acoustic waves for the localized generation of motion within tissues has been early adopted by USE. The technique is commonly known as ARF, and it has been initially implemented over acoustic mediums based on water. The physical principle of ARF relies on the focusing of acoustic ultrasonic waves (in the order of MHz) traveling at the speed of sound in water (c_p) that are absorbed by the tissue, with an ultrasound absorption coefficient α_p, and transformed into radiation force (F_{ARF}) within a volumetric region of submillimeter dimensions as [88]:

$$F_{ARF} = \frac{2\alpha I}{c_p}, \tag{4.1}$$

where I is the acoustic intensity of the pump beam. ARF can be produced by a single element ultrasonic transducer with a fixed focus [89], or using an element array transducer with refocusing and beam steering capabilities [90, 91]. The coupling between the transducer and the tissue needs to be an acoustic medium with a similar acoustic wave speed c_p (water or gel) that allows the full transmission of acoustic waves. Then, ARF is considered a contact method and it can generate mechanical waves not only at the surface, but beneath tissues (remote excitation) which is beneficial for generating SAWs, and shear waves. ARF can burst pulses from 10 μs to 10 s which provides extended bandwidth [88]. Finally, due to the necessary abortion of acoustic energy by tissues and the sufficiently large pressures that can be exerted, this method can represent a

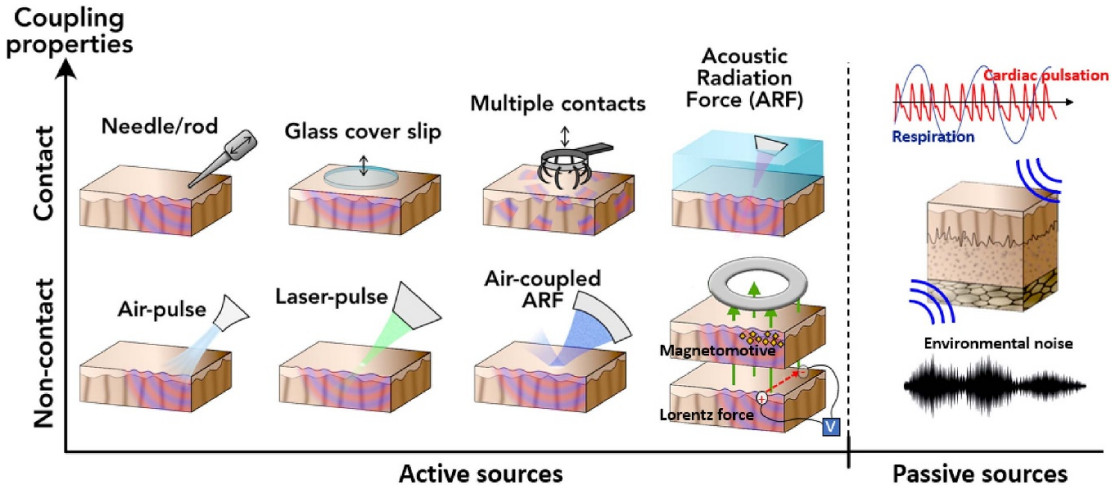

Figure 6. Diagram showing different types of active and passive excitation sources used in wave-based OCE divided into two groups according to their coupling nature: contact and non-contact.

safety concern for certain applications such as the elastography of ocular tissues [85]. Extended efforts are being put into developing methods that reduce the acoustic pressures by preserving the bandwidth and displacement amplitude [92].

4.1.3. Air-pulse stimulation

This excitation method is based on the fast and controlled release of compressed air through a conduit with a diameter <0.15 mm. The micro-air pulse delivers a localized impulse stimulus towards the surface of tissues in order to produce a wave perturbation. It was firstly proposed in [93, 94], and since then, it has been applied to the generation of SAWs for the elastography of diverse tissues, including cornea [20, 26, 62, 95–101], skin [13, 102, 103], cardiac and skeletal muscles [104–106], and cartilages [107], to name just a few applications. Air-pulse stimulation has advantageous properties relevant for its clinical translation, including its non-contact coupling with tissues, the generation of small loading pressures (in the mPa range), and the precedent of being used safely in other screening devices in ophthalmology [108, 109]. The mechanical waves generated by air-pulse estimation generally have lower frequency bandwidth since this method is limited to short pulses (< 0.8 ms duration) [94], which restricts the spatial resolution in the generation of quantitative maps of elasticity.

4.1.4. Laser-pulse stimulation

This excitation method leverages the light absorption of ultraviolet pulse-lasers (<10 ns duration) within tissues for the generation of SAWs and shear waves. As described in the USE study in [110], two regimes are identified during the underlying phenomena: the thermoelastic and ablative regimes. In the thermoelastic regime (lower laser beam energy <40 mJ), the absorption of the laser produces temperature increase and, in consequence, the local dilation of tissues that produces motion. In the ablative regime, partial vaporization of the medium (damage) is produced, which, in consequence, produces local displacements with a larger amplitude. Therefore, for a selected laser energy fluence, the motion will be produced in the thermoelastic or ablative regime depending on the optical absorption of the sample, as explored using OCE in tissue-mimicking phantoms and tissues [111]. Laser-pulse stimulation has been applied in the elastography of cornea [112], skin [113], and liver [111] for the non-contact generation of large bandwidth SAWs and Lamb waves. Moreover, laser stimulation in conjunction with photo-absorbers [114], and dye-loaded perfluorocarbon nanodroplets (also named as 'nanobombs') [79–82] inside tissues allows the localized generation of shear and LSWs of great importance in the transverse elastic characterization of tissues. Finally, the dependence of optical absorption coefficient in tissues with the laser energy fluence needed to produce detectable displacements are in the same range and, in some cases, surpasses the permissible safety levels. Current efforts are being focused on reducing the laser energy fluence for *in vivo* applications by breaking the absolute dependence of motion amplitude and tissue optical absorption using other laser-activated motion mechanisms such as nanobombs [79].

4.1.5. Air-coupled acoustic reflection-based force (AC-ARF)

Similar to ARF, this technique focuses ultrasonic waves on the surface of tissues through the air to produce displacement and wave propagation. Firstly proposed by Ambrozinski *et al* [115], the use of air-coupled ultrasound transducers was demonstrated to produce waves at larger bandwidths detectable by PhS-OCT. The physical principle of AC-ARF relies on the radiation pressure (P) generated by the reflection of acoustic waves at the border of tissues due to the large mismatch of acoustic impedances between the air ($\rho c_{\mathrm{p_{air}}} \sim 429$ Pa·s m^{-1}) and soft tissues ($\rho c_{\mathrm{p_{water}}} \sim 1.5 \times 10^6$ Pa·s m^{-1}) as [116]:

$$P = \frac{I\left(1 + \mathrm{R}^2\right)}{c_{\mathrm{p}}}, \tag{4.2}$$

where I is the acoustic intensity of the pump beam, R is the reflection coefficient at the air/tissue interface, and c_{p} is the acoustic wave speed in air ($\sim$340 m s^{-1}). Since acoustic impedance in air and tissue are very different, $R \approx 1$ and the acoustic energy is efficiently converted into displacements for lower acoustic pressures. AC-ARF is considered a non-contact method since only air is needed as the interphase of the transducer and tissues. The lateral size of the focusing spot will be determined by the frequency of the air-coupled ultrasound transducer (frequencies in the range of 20 kHz to several MHz) and its phase distribution (focusing power achieved with a fixed curvature [84, 117] or the use of masks and mirrors [118]). AC-ARF has been successfully tested in the elastography of cornea, achieving a localized focusing spot size of $\sim$0.35 mm using a 1 MHz transducer [84, 119], and an extended spot size of $\sim$4 mm when a 25 kHz transducer is utilized [117]. AC-ARF is also capable of producing large bandwidth waves due to the generation of sharp temporal transient [84] and queasy-harmonic [119] pulses. Finally, calculations on the acoustic intensity penetrating tissues were found to be orders of magnitude lower than 28 W cm^{-2}, which is the maximum exposure limit in ophthalmic imaging [120]; however, formal safety studies of this technology are still needed.

4.1.6. Magnetomotive excitation

The magnetomotive excitation leverages the properties of magnetic nanoparticles incorporated into tissues when exposed to an external dynamic magnetic field as shown in figure 6. Then, the nanoparticles vibrate as internal and localized motion transducers capable of producing mechanical wave propagation. Firstly proposed by Ahmad *et al* [121], wave-based OCE based on magnetomotive excitation has been only explored in a few cases when combined with thermotherapy dosimetry [122, 123]. The possibility of confining the magnetic nanoparticles to small cylindrical regions at higher concentrations within tissues allows the generation of localized wave propagation [123]. Challenges with this method rely on the need for sufficiently high magnetic field gradients with a relatively high concentration of nanoparticles in order to produce higher displacements measurable by PhS-OCT. Finally, even though this method is considered non-contact, maintaining low toxicity due to the presence of nanoparticles in tissues can limit its application for *in vivo* tissue elastography.

4.1.7. Lorentz force

This excitation method was firstly proposed in USE [124] and later extended in OCE [125], and consist in the generation of transient force when an electrical current is induced in tissues under the presence of a magnetic field flow. As shown in figure 6, two electrodes are located in the sample's surface and they are subjected to a transient pulse of voltage while a magnet produces an out-of-plane magnetic field. Since biological tissues are inherently conductive, biocurrent is generated with a direction perpendicular to the magnetic field, producing Lorentz force in a direction perpendicular to both current and magnetic field directions [125]. The generated force produces shear and SAW waves in tissues that can be detected by PhS-OCT. Difficulties of this method include the generation of biocurrent ($\sim$15 mA in [125]) that can excide safety limits in human applications. Moreover, in addition to the electrical damage, resistive heating may produce tissue ablation. However, due to the weak and short duration of the electrical pulses, these problems may be reduced and confined only in the excitation area.

4.1.8. Passive stimulation

Passive elastography constitutes one of the recent promising branches of wave-based OCE that leverages non-contact passive sources of mechanical waves (e.g. permanent ambient noise and physiological noise) for the local estimation of mechanical properties. It has been firstly introduced in USE [126], and then extended into wave-based OCE [127]. Typical passive sources of mechanical waves in the human body are muscular activity, heart beats [128], and heart wall vibrations [129]. Vessel pulsatility has been used in OCE to quantify the stiffness of arteries in developing chick embryos by imaging from outside the vessel [130].

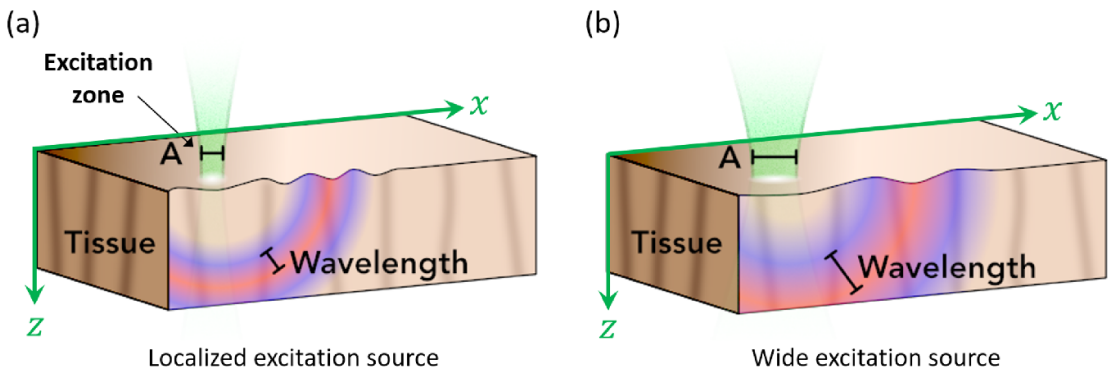

Figure 7. The impact of the excitation spatial extend (A, defined as the area diameter) in the characteristic wavelength of transient mechanical waves in tissue. In (a), localized sources (smaller A) can produce smaller excitation wavelengths in tissues. In (b), extended sources (larger A) can produce stronger waves with less attenuation by the cost of larger wavelengths.

Passive elastography uses the noise-correlation technique to passively retrieve the elastic parameter of *in vivo* tissues, with great potential for clinical translation. Furthermore, the resolution of this technique is not limited by the excitation wavelength as all other wave-based OCE techniques (section 6.5), but it is only limited by the imaging resolution according to [131]. Finally, the major limitation of using passive sources is the inability to generate quantitative information (wave speed) when the frequency content of the passive noise is unknown or spread out.

4.2. Spatial extent

The spatial extend refers to the spatial distribution (superficial or volumetric) in which the force or displacement is applied within the elastic medium under study. If we assume an infinitely short temporal pulse in an infinite elastic media, the bandwidth (BW) of the generated wave will be upper limited by the spatial extent of the excitation area (A, defined as de area diameter), and the relaxation of the stress across the same area (which occurs at the shear wave speed c_s) as:

$$\mathrm{BW} < c_s/A. \tag{4.3}$$

Therefore, the smaller the excitation spatial extend is, the larger bandwidth can be achieved. In addition, the spatial distribution of the sources has an effect on the type of mechanical waves and the interaction between them within the sample.

4.2.1. Localized and wide sources

Localized sources tend to generate force/displacement with a spot size diameter in the order of the sub-millimeters (see figure 7(a)) in order to achieve higher localization of the wave and larger bandwidths, as explained in equation (4.3). Examples of localized motion sources are air-pulse (>0.15 mm), ARF (>0.5 mm), AC-ARF (>0.3 mm), laser-pulse (>150 μm), and displacement (>2 mm) stimulations. Typically, localized sources produce SAWs in semi-infinite type tissues [132] and Lamb waves in thin-plate and layered tissues [20, 133]; nevertheless, it is possible to create shear waves with ARF when focusing deeper in the tissues [134, 135]. The downside of this configuration is the imminent attenuation of the propagating wave as it spreads cylindrically or spherically from the source within the sample [48]. On the other hand, wide sources (see figure 7(b)) can drive more displacement energy into the sample by the cost of lower bandwidth (see equation (4.3)). Wide displacement sources have been demonstrated to be instrumental in producing LSWs propagating towards depth (z-axis), as demonstrated in [76, 78]. Other excitation configurations have been used in order to emphasize specific types of waves in tissues. For instance, sources with non-symmetric stimulation areas such as lines were used in [23, 84] to create quasi-plane waves reducing the attenuation caused by the wave geometrical spreading. On the other hand, using orthogonal excitation of tissues with respect to the OCT beam direction can produce shear waves rather than SAWs as demonstrated in [135].

4.2.2. Distributed sources

The distribution of more than one localized source in tissues can generate wave interference patterns of use in wave-based OCE. For instance, standing waves are generated in between two harmonic displacement sources vibrating at the same frequency and producing propagating waves traveling towards each other [29]. In this case, local wave speed can be found using wavelength estimators (more details in section 6.4). Similarly, a crawling wave is a wave interference pattern formed when two waves with different frequencies

(with a frequency difference $\Delta\omega$) interfere against each other. As a result, the crawling wave is formed and travels at a slower version of a shear wave. The crawling wave speed (c_{CrW}) is related to the shear wave speed (c_{s}) [29, 136] as:

$$c_{\mathrm{CrW}} = c_{\mathrm{s}} \frac{\Delta\omega}{2\omega + \Delta\omega}. \tag{4.4}$$

The use of crawling waves can be beneficial when shear waves travel much faster than the OCT acquisition system as it happens in stiffer tissues such as ocular sclera and tendons. Then, $\Delta\omega$ can be chosen to make crawling waves to travel at fractions of the shear wave speed.

A special case of wave interference happens when more than two localized displacement sources are used to generate harmonic excitation in tissues. It is called reverberant shear wave fields and can be created in tissues for its elastic characterization. A reverberant or diffuse field can be understood as the limiting case of the continuous harmonic interaction of multiple mechanical waves traveling in a statistical distribution across all possible directions [137]. Reverberant elastography was firstly proposed in USE [137, 138], and later extended in wave-based OCE for the elastography of corneal tissues [65], also called Rev-OCE. Given the z-component of a 2D reverberant particle velocity field $V_z(r)$ (i.e. the time-derivative of displacement) excited at ω_0 angular frequency, its local complex autocorrelation along any perpendicular direction to the z-axis ($R_{\mathrm{V_zV_z}}(\Delta r_x)$) is given by [65]:

$$R_{\mathrm{V_zV_z}}(\Delta r_x) = C\left[j_0(k_0\Delta r_x) - \frac{j_1(k_0\Delta r_x)}{k_0\Delta r_x}\right], \tag{4.5}$$

where C is a scalar amplitude constant; j_0 and j_1 are spherical Bessel functions of the first kind of zero and first order, respectively; Δr_x is the autocorrelation direction along the x-axis; and k_0 is the local wavenumber such that $c_{\mathrm{s}} = \omega_0/k_0$. Then, assuming a linear, elastic, locally uniform, and isotropic medium, the local shear wave speed c_{s} can be estimated from the local autocorrelation of a reverberant field by fitting equation (4.5). Rev-OCE, leveraging on the spatial distribution of various displacement sources, has demonstrated interesting capabilities in the OCE of individual layers of composite tissues such as cornea using $\omega_0 = 2\pi \times 2000$ rad s^{-1} excitation frequency [65].

4.3. Temporal shape

The temporal shape refers to the temporal characteristics of the force or displacement that is applied to the target tissue. An elastic medium can be characterized by the time in which a stress perturbation has completely relaxed after being produced by a temporal impulsive load applied within a spatial region of area diameter A. This time, also called stress relaxation time (τ_{R}), is related to the speed c_{s} of shear waves (which is related to the material's shear modulus), excitation area diameter A by [139]:

$$\tau_{\mathrm{R}} \approx A/c_{\mathrm{s}}. \tag{4.6}$$

As shown in figure 8(a), a softer medium will have a larger τ_{R} compared to a stiffer medium for the same excitation parameters (i.e. impulsive load, and A). Therefore, τ_{R} will have an impact on the frequency content of the temporal excitation when it is transient, quasi-harmonic/harmonic, and multifrequency.

4.3.1. Transient motion

In transient excitation, the burst of a single pulse is typically used to produce a broadband wave. For a pulse with a burst duration T_{Pulse}, given the relaxation time τ_{R} of an elastic medium, the bandwidth of the excitation will be defined by $\sim 1/T_{\mathrm{Pulse}}$ if $T_{\mathrm{Pulse}} \gg \tau_{\mathrm{R}}$. On the other hand, if $T_{\mathrm{Pulse}} \ll \tau_{\mathrm{R}}$, then the bandwidth is defined by c_{s}/A as shown in equation (4.3) (impulsive simulation). Therefore, in transient excitation, the bandwidth of a generated wave within a tissue can be increased by primarily reducing the diameter of the excitation area (A) and, subsequently, bursting pulses of smaller duration T_{Pulse}. Almost all wave-based OCE techniques make use of excitation sources in transient mode since larger bandwidths allow for wave speed dispersion measurements that are required for the characterization of Lamb waves and viscoelastic tissues. However, the motion energy is distributed in the whole frequency spectrum, and its bandwidth will be dependent not only on T_{Pulse}, but on the τ_{R} of the elastic material [80, 84], as shown in figure 8(b). Then, the average frequency (f_{Avg}) which defines the elastography resolution (extended clarification in section 6.5), tends to be smaller than $1/2T_{\mathrm{Pulse}}$ (figure 8(b)). The most typical transient shape used in OCE is the square pulse. It is used in air-pulse stimulation for the temporal release of compressed air, in ARF/AC-ARF for the modulation of the acoustic MHz-range carrier signal, and in laser-based excitation for the triggering of the pulsed laser. Other shapes such as a Gaussian pulse or a single sinusoidal tone are typically used in contact displacement excitation methods.

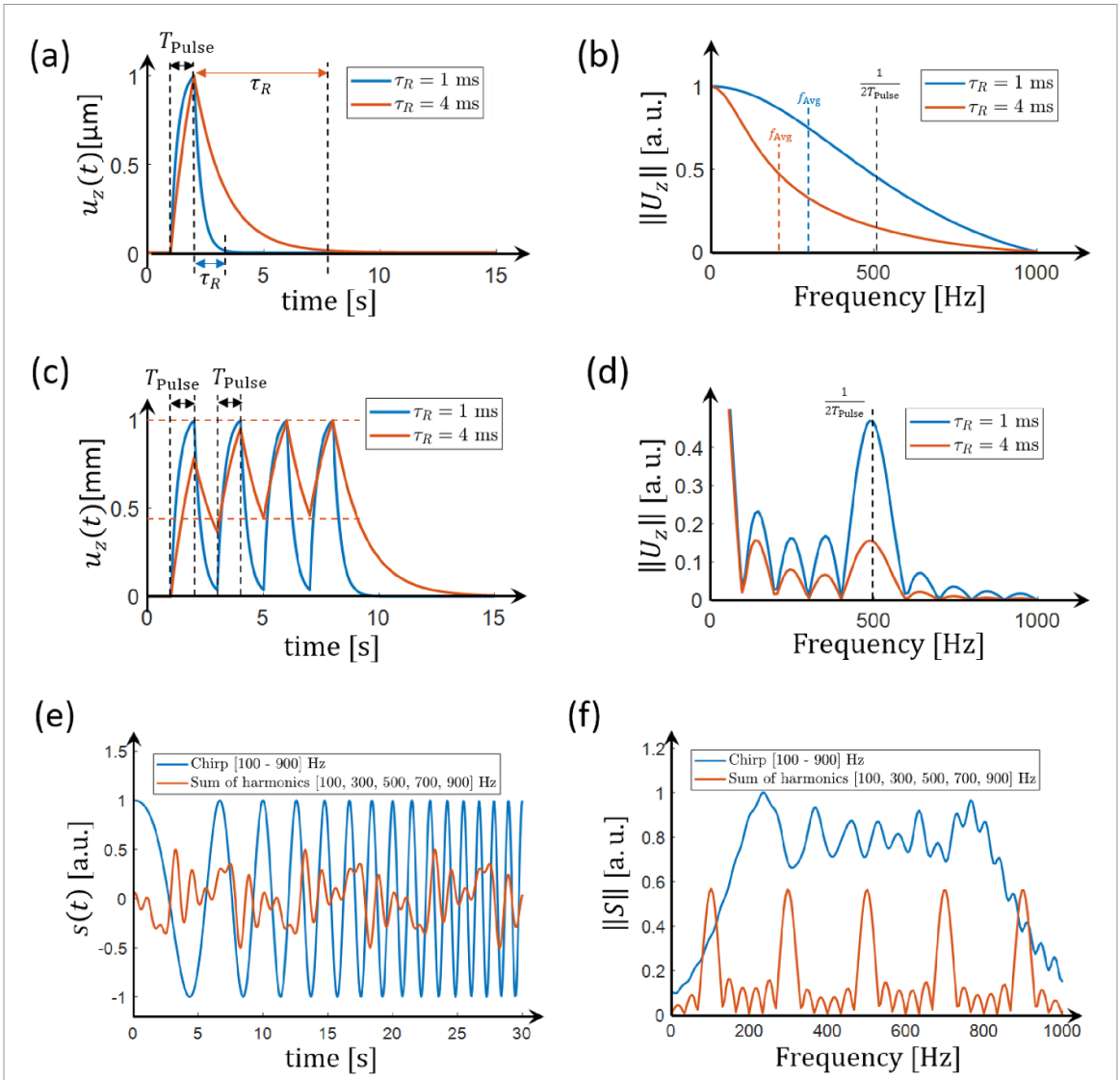

Figure 8. Types of temporal excitation signals in wave-based OCE (a), (c), (e) with their respective frequency responses (b), (d), (f). In (a), the temporal displacement $u_z(t)$ in two elastic materials with different relaxation times (stiff: $\tau_R = 1$ ms, and soft: $\tau_R = 4$ ms) is produced by a transient pulse with a duration T_{Pulse}. In (b), the frequency response of the pulses in (a) is shown with the calculation of the average frequency (f_{Avg}) for each case. The quasi-harmonic displacement in the stiffer ($\tau_R = 1$ ms) and softer ($\tau_R = 4$ ms) elastic media is shown in (c) when produced by a train of four pulses (periodicity $2T_{Pulse}$). (d) Frequency response of the quasi-harmonic displacement signals of (c). Finally, multifrequency signals used for the excitation of tissues are shown in (e) including its frequency response in (f) for two cases: a chirp signal covering (100–900) Hz range, and a sum of five harmonic signals with random phases covering (100–900) Hz with steps of 200 Hz.

4.3.2. Harmonic and quasi-harmonic motion

Harmonic excitation is the limiting case in which the transient perturbation is repeated along a large extend of time ($\gg \tau_R$) with a periodicity $2T_{Pulse}$. As opposed to a transient motion, the generated wave bandwidth is narrow, and the motion energy is concentrated at an operational frequency ($f_0 = 1/2T_{Pulse}$). The main advantage of this method is the possibility of raising the central excitation frequency f_0 of waves despite the limitations of τ_R as illustrated in figures 8(a) and (b). Here, even when the relaxation time is greater than $1/f_0$, harmonic oscillation can still be achieved. Harmonic excitation has been typically used in wave-based OCE using magnetomotive [121], and contact displacement [22, 29, 65, 76, 136] stimulation.

One interesting case in between transient and harmonic motion is the quasi-harmonic excitation. Here, a limited number of cycles of the transient pulse are burst, as shown in figure 8(c). Then, speed dispersion measurements (required for the characterization of Lamb waves and viscoelastic tissues) can be obtained in a smaller bandwidth Δf and still concentrate most of the motion amplitude in f_0 as shown in figure 8(d), despite of the τ_R of the medium. For instance, if $N = 5$ cycles of a $f_0 = 1$ kHz signal are burst, then, the excitation bandwidth is given by $\Delta f \approx f_0/N = 200$ Hz. Then, the selection of N will define the excitation bandwidth for a selected central frequency. Quasi-harmonic excitation can be instrumental for the comparison of phase speed of mechanical waves in tissues at the same frequencies. Comparing speeds at the

Table 1. Comparison chart of temporal excitation methods in wave-based OCE.

Temporal shape of excitation			
Signal	Spectrum	Advantages	Disadvantages
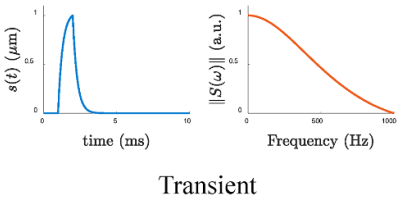 Transient		▪ Large distributed frequency bandwidths. ▪ Avoid reflections from tissue borders. ▪ Easy to track using time of flight estimators (group velocity).	▪ Bandwidth depend on tissue relaxation time τ_R. ▪ Motion is highly attenuated by medium, specially for higher frequencies.
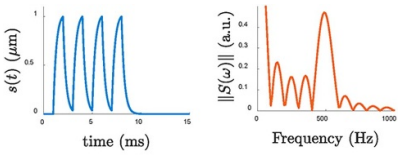 Quasi-harmonic/Harmonic		▪ Control of the central frequency f_0 of the excitation, despite tissue relaxation time τ_R. ▪ More displacement energy which translates in larger propagation distances.	▪ Narrow frequency bandwidths. ▪ Can produce reflections from tissue borders and other boundaries.
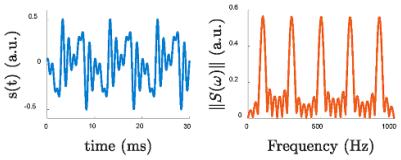 Multifrequency		▪ Control of the multiple central frequencies f_0 and/or excitation bandwidth, despite tissue relaxation time τ_R. ▪ More displacement energy which translates in larger propagation distances.	▪ Can produce reflections from tissue borders and other boundaries. ▪ Restrictive in some excitation methods such as air-pulse, and laser-pulse stimulation.

same frequencies is fundamental for monitoring tissue properties in longitudinal studies. Unlike the transient case, in which group speed measurements are tied to the average frequency (f_{Avg}) of the spectrum which changes between softer and stiffer media (see figure 8(b)), quasi-harmonic excitation allows the comparison of phase speed at the same frequency f_0, regardless of changes in the elasticity of tissues (figure 8(d)). Quasi-harmonic excitation has been implemented in contact displacement methods [12, 22, 140], and AC-ARF stimulation [119].

4.3.3. Multifrequency motion

Multifrequency excitation can be produced when a time signal contains frequency components encode along time (chirp signals) or by summing up harmonics of different frequencies, as shown in figure 8(e). This type of excitation can distribute the motion energy at a frequency range or specific frequency points (figure 8(f)) instead of the whole spectrum as in transient stimulation. It has been applied using ARF [92], and contact displacement stimulation [25] for the wave dispersion analysis in tissue-mimicking phantoms and corneal tissues, respectively. The advantage of multifrequency excitation over quasi-harmonic is the ability to produce excitation at multiple discrete frequencies or over a constrained bandwidth, and still produce stronger displacement compared to transient excitation. However, this technique is restrictive to some excitation methods that cannot handle arbitrary input signals such as air-pulse and laser-pulse estimation. In table 1, a comparative chart of all temporal excitation approaches (transient, quasi-harmonic/harmonic, and multifrequency) in wave-based OCE is conducted including advantages and disadvantages.

5. Motion detection in OCE

In the previous sections, the different excitation methods that produce motion and wave propagation in soft tissues were discussed. In this section, we are going to describe the principal OCT implementations that allow the spatially resolved displacement measurement, which is fundamental for the visualization, tracking, and speed estimation of mechanical waves in the context of wave-based OCE.

5.1. OCT for elastography

Two OCT implementations are the most common in wave-based OCE due to fast acquisition, high motion sensitivity, and high phase stability required for the capturing of fast propagating waves (ranging from 0.5 to 20 m s^{-1} [2, 8]) with submicron displacements: spectral-domain OCT (SD-OCT), and swept-source OCT (SS-OCT) as shown in figures 9(a) and (b), respectively. In both cases, the optical systems consist of a light source with a central wavelength λ_0 that is divided into two beams: one going toward the sample arm (i.e. where the tissue is located), and the other going to the reference arm (where a reflective mirror is located). In

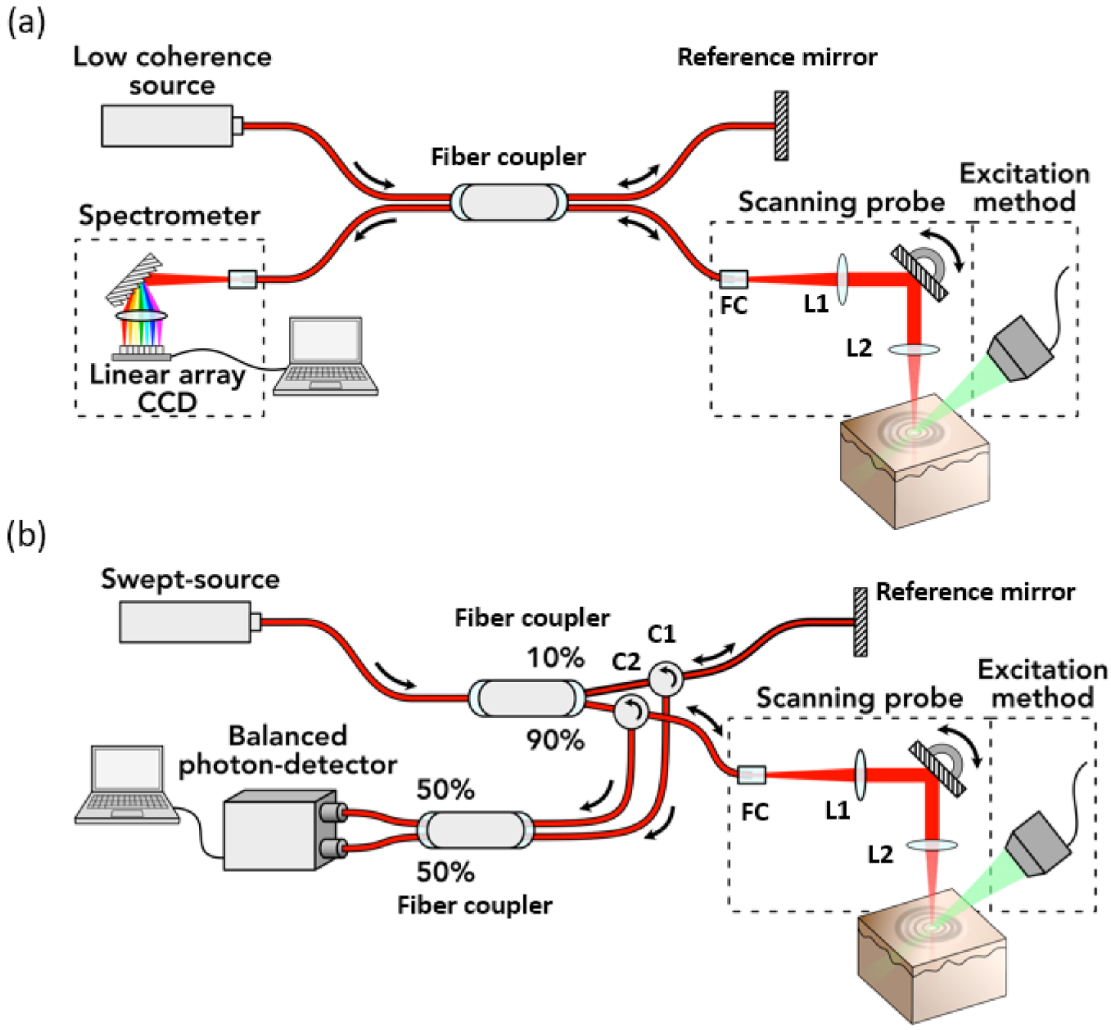

Figure 9. Schematic of wave-based OCE experimental setups including the excitation method, the target sample, and the optical system based on two OCT implementations: (a) SD-OCT, and (b) SS-OCT. FC: fiber coupler, L1: collimation lens, L2: telecentric scan lens, C1, C2: circulators.

the SD-OCT system, the light source is broadband (i.e. it contains a spectral bandwidth of $\Delta\lambda$ centered at λ_0), and the reflected light from both arms are collected back and recombined (to produce interference) using a coupler. Then, the light is captured by a spectrometer in order to measure the spectral interference fringes $i_A(k)$, where k is the linear wave-number [141]. On the other hand, the SS-OCT system uses a swept-source laser as the light source, which will sweep a narrowband light beam along the spectral bandwidth $\Delta\lambda$ centered at λ_0. Then, the reflected light from both arms go through optical circulators and is recombined using a coupler. At the end of the coupler, the intensity of the interfered light is measured by a balanced photodetector to generate the spectral interference signal $i_A(k)$. While in SD-OCT $i_A(k)$ is obtained instantly (k-wise) by the integration along the exposure time at, in SS-OCT $i_A(k)$ is progressively obtained while the laser is swept.

In OCT, an A-line ($I_A(z)$) represents the depth-dependent (along z-axis) information of the sample at a particular lateral position x_0. $I_A(z)$ is obtained from $i_A(k)$ by applying background subtraction and the discrete Fourier transform [141, 142]. Then, the magnitude of the complex-valued $I_A(z)$ (i.e. $I_A(z)$) represents the depth-dependent intensity of the backscattered light coming from the different structures of the sample (e.g. tissue layers, boundaries of structures, etc). Then, in conjunction with a mechanical system (e.g. a motorized stage, a piezoelectric actuator, or a galvanometer controlling a mirror) capable of steering the light beam to other lateral positions along the x-axis, and an objective lens to focus the light beam into the sample, 2D B-mode intensity images can be generated. In OCT, the axial resolution is determined by half of the coherence length (l_c) which depends on the properties of the light source (λ_0, $\Delta\lambda$) as [141]:

$$\frac{l_c}{2} = \frac{2\ln(2)}{\pi}\frac{{\lambda_0}^2}{\Delta\lambda}, \tag{5.1}$$

which is typically in the micrometer scale (2–15 μm). The lateral resolution depends on the numerical aperture of the objective lens and λ_0 of the light source. Both axial and lateral resolution will define the OCT system capabilities in generating highly detailed B-mode structural images of tissues. Moreover, the selection of the central wavelength will affect the effective axial imaging penetration of OCT as tissues will absorb and scatter more or less light depending on its components. For instance, wavelengths around 850–1050 nm are chosen for ocular tissues to balance light scattering by tissues and water absorption band in order to maximize penetration depth [28]. Finally, in wave-based OCE, OCT systems are not only used to produce B-mode images of tissues but, more impotently, for the measurement of displacement generated by excitation sources that will be explained in the next sub-section.

5.2. Motion measurements

In the early development of OCE, speckle tracking technique has been utilized for the vectorial displacement calculation accomplished by digital image correlation within a multi-pixel kernel in a sequence of B-mode structural images ($||I_A(z)||$) [4, 143, 144]. One major advantage of this technique is the possibility of measuring lateral- and depth-wise displacement, which is instrumental for the full characterization of mechanical waves when traveling in different directions. However, speckle tracking and its variants usually require large displacements, which may represent a challenge for the safety of delicate tissues (e.g. ocular tunic). Due to the coherent wave superposition nature of speckle tracking, it cannot detect displacements beyond fractions of the OCT speckle size producing speckle decorrelation and, in consequence, low signal-to-noise ratio (SNR) estimates of tissue displacement [145]. Therefore, the speckle tracking technique has not been used extensively for the measurement of wave propagation.

In the context of wave-based OCE, PhS-OCT has been the predominant method for motion detection [2, 8]. Unlike speckle tracking that uses only intensity information, this method leverages the phase extracted from OCT complex-valued A-lines: $\mathrm{Arg}(I_A(z)) = \phi(z)$. Then, in a medium with refractive index n, for a set of A-lines collected along time in the same lateral position x_0, the phase difference between two consecutive A-lines $\Delta\phi(z) = \phi(z, t_1) - \phi(z, t_0)$, for consecutive time points t_o and t_1 ($t_1 > t_0$), is related to the axial differential displacement $u_z(z)$ as [87, 146]:

$$u_z(z) = \Delta\phi(z)\frac{\lambda_0}{4\pi n}. \tag{5.2}$$

PhS-OCT is ultrasensitive for displacement detection (sub-nanometer level); however, it is only measured along the axial direction (i.e. z-axis) and is vulnerable to various sources of phase noise. The minimum phase difference that PhS-OCT can measure is given by $1/\sqrt{\mathrm{SNR}}$, which is valid for a range of 20–50 dB of typical OCT SNRs [147]. This effect is mainly produced by the shot-noise assuming a high SNR. In SS-OCT, the phase stability of PhS-OCT suffers from the desynchronization produced by the fluctuation of the swiping laser, also called Jitter noise. Two techniques were proposed in order to overcome Jitter based on optical frequency referencing: a λ-trigger using a fiber Bragg grating [148], and the use of a k-clock generated using a Mach–Zehnder interferometer. On the other hand, the phase fluctuations produced between the reference arm and the sample arm introduces another source of noise affecting the phase in both SS-OCT and SD-OCT systems. In order to compensate for this noise, the common-path technique has been implemented with great success in SD-OCT [149], and SS-OCT [14].

When a mechanical wave travels laterally (x-axis) in a medium (e.g. SAWs, shear, and lab waves), the particles of such medium at a given constant position x_0 in space will vibrate with a particular axial velocity $v_z(z)$ along time. Then, it is more appropriate to represent the particle velocity of a wave in terms of phase change between consecutive A-lines as [150]:

$$v_z(z) = \Delta\phi(z)\frac{\lambda_0}{4\pi n T_s}, \tag{5.3}$$

where T_s is the time sampling resolution (i.e. $t_1 - t_0$). However, in reality, $\Delta\phi(z)$ is related to the change of optical path length assuming the same refractive index n. Then, if the medium under analysis have layers with different refractive indices towards depth, $v_z(z)$ will accumulate apparent motions coming from the interfaces between those layers that produce refractive index mismatch. A compensation mechanism contemplating two different refractive media (n_1 and n_2) was proposed to generate the true phase change $\Delta\phi_T(z)$ as [2, 140]:

$$\Delta\phi_T(z) = \Delta\phi(z) + \left(\frac{n_2}{n_1} - 1\right)\Delta\phi(s_1), \tag{5.4}$$

where n_1 and n_2 are the refractive indices from the air (between the OCT probe and the sample), and sample medium, respectively. $\Delta\phi(s_1)$ is the phase change produced by the motion at the surface s_1 of the sample

(between mediums n_1 and n_2). Equation (5.4) is widely used in wave-based OCE since, in the majority of cases, the coupling medium between the OCT probe and the tissue under analysis is air. Then, typical refractive indices for tissue ($n_2 \approx 1.4$), and air ($n_1 \approx 1$) produce non-trivial distortions artifact in the order of $0.4\,\Delta\phi(s_1)$.

Equation (5.4) can be extended for more complex cases of three or more layers with different refractive indices. For instance, in ophthalmology, the elastography of crystalline lens will require the OCT beam to go through air, cornea, and aqueous humor before reaching lens tissue. On the other hand, when a glass coverslip is used in between the OCT probe and the tissue to generate vibrations and wave propagation [76, 78], the OCT bean needs to travel through air (n_1), glass (n_2), and tissue (n_3) with different refractive indices. Then, the true phase difference n_2 within the tissue for a general three-layer case is proposed as [76]:

$$\Delta\phi_{\mathrm{T}}(z) = \Delta\phi(z) + \left(\frac{n_3}{n_2} - 1\right)\Delta\phi(s_2) + \left(\frac{n_3}{n_1} - \frac{n_3}{n_2}\right)\Delta\phi(s_1), \tag{5.5}$$

where $\Delta\phi(s_1)$, and $\Delta\phi(s_2)$ are the phase differences produced by motion at the boundaries between $n_1 - n_2$, and $n_2 - n_3$ interfaces, respectively. Finally, PhS-OCT motion can also suffer from unwrapping problems when $\Delta\phi(z)$ is greater than π. Even when unwrapping algorithms can be used to compensate for this effect, they are very sensitive to noise and could reach a limit in which the speckle decorrelation is present [145].

Finally, some hybrid methods, such as Doppler variance [151, 152], uses the magnitude ($\|I_{\mathrm{A}}(z)\|$) and phase ($\mathrm{Arg}(I_{\mathrm{A}}(z))$) information of complex A-lines for the detection of motion along axial and lateral axes. This method overcomes the problem of PhS-OCT in measuring motion only along the z-axis. In the context of wave-based OCE, Doppler variance has been instrumental for the tracking of shear waves [134, 135, 153], and LSWs [77], when the main particle velocity direction produced by these waves is not aligned along the z-axis. The limitation of this technique relies on the need for large displacements in order to detect reliable motion information.

5.3. Phase estimators

There are different methods for the estimation of $\Delta\phi(z)$ from a set of complex A-lines $I_{\mathrm{A}}(z,t)$ along time. Considering the complex exponential form of two consecutive A-lines: $I_{\mathrm{A}}(z,t_0) = \|I_{\mathrm{A}}(z,t_0)\|e^{i\phi(z,t_0)}$, and $I_{\mathrm{A}}(z,t_1) = \|I_{\mathrm{A}}(z,t_1)\|e^{i\phi(z,t_1)}$, where $t_1 > t_0$; then, the most direct estimation of $\Delta\phi(z) = \phi(z,t_1) - \phi(z,t_0)$ can be achieved by:

$$\Delta\phi(z) = \arctan\left[\frac{\mathrm{Im}\left(I_{\mathrm{A}}(z,t_1)\,I_{\mathrm{A}}(z,t_0)^*\right)}{\mathrm{Re}\left(I_{\mathrm{A}}(z,t_1)\,I_{\mathrm{A}}(z,t_0)^*\right)}\right], \tag{5.6}$$

where $\mathrm{Im}(\cdot)$ and $\mathrm{Re}(\cdot)$ are imaginary- and real-part operators, and I^* is the complex conjugated version of I. Equation (5.6) is very sensitive to noise, and more robust methods are needed for the phase difference retrieval. Loupas' algorithm has been used in USE [154, 155], and, lately, it has been applied in wave-based OCE [29, 65, 76]. Loupas' approach increases the SNR and stability of the phase difference estimation by leveraging on the depth information of two consecutive A-lines as [156]:

$$\Delta\phi(z_0) = \frac{\arctan\left[\left(\frac{\sum_{m=0}^{M-1}\left[Q(z_m,t_0)\,II(z_m,t_1) - II(z_m,t_0)\,Q(z_m,t_1)\right]}{\sum_{m=0}^{M-1}\left[II(z_m,t_0)\,II(z_m,t_1) + Q(z_m,t_0)\,Q(z_m,t_1)\right]}\right)\right]}{1 + \arctan\left(\frac{\sum_{m=0}^{M-2}\sum_{n=0}^{1}\left[Q(z_m,t_n)\,II(z_{m+1},t_n) - II(z_m,t_n)\,Q(z_{m+1},t_n)\right]}{\sum_{m=0}^{M-2}\sum_{n=0}^{1}\left[II(z_m,t_n)\,II(z_{m+1},t_n) + Q(z_m,t_n)\,Q(z_{m+1},t_n)\right]}\right)/2\pi} \tag{5.7}$$

where z_m is the mth element towards the depth, $II(z,t) = \mathrm{Re}(I_{\mathrm{A}}(z,t))$, and $Q(z,t) = \mathrm{Im}(I_{\mathrm{A}}(z,t))$, and M is the size of the window in the axial direction centered at z_0 in which the phase estimation is performed. M size can be chosen to be 2% of the depth size for a good trade-off between SNR improvement and displacement axial resolution.

5.4. Acquisition protocols

In the previous sections, we review the main OCT implementations and motion estimation methods used for detecting waves in OCE. In this section, we will review the main acquisition protocols for the measurement of spatial motion distribution along cross-sections (2D), and volumes (3D) along time. The total acquisition speed will be determined by the number of A-lines acquired in space and time to capture wave propagation with enough resolution. The choice of the acquisition protocol will depend on the wave characteristics, the A-line rate of the OCT system, and the spatial requirements for the measurement of wave speed.

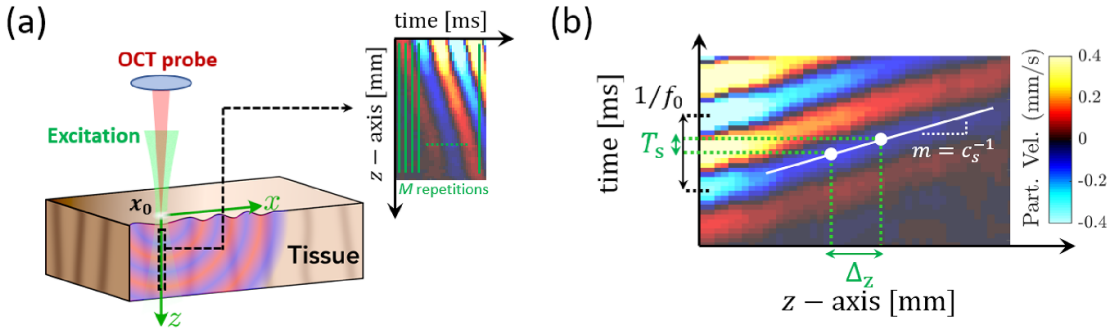

Figure 10. M-mode acquisition protocol. In (a), A-lines (M repetitions) are acquired at the fixed lateral position x_0 along depth and time. The mechanical excitation produces longitudinal shear waves propagating towards the z-axis. In (b), the spatio-temporal propagation of the wave in (a) is temporally sampled at the step time T_s which enables the tracking of the wave at the smallest travel distance Δ_z along the z-axis. The slope m of the line plot represents the inverse of the wave speed. Colormap in (a) and (b) represents particle velocity (motion) along the z-axis.

5.4.1. M-mode acquisition

The M-mode refers to the 'motion,' and it consists in the repetitive acquisition of A-lines along time for a static lateral position x_0 as shown in figure 10(a). Then, the time taken by the OCT system to acquire two consecutive A-lines is called time resolution (T_s) and is related to the A-line rate as $1/T_s$. Since A-lines provide 1D depth-dependent information, M-mode has been used to track the propagation of waves traveling along the z-axis, such as LSWs [78–82]. Then, space-time ($z-t$) maps can be generated for the subsequent depth-dependent speed estimation (figure 10(a)). Different criteria are used to select the appropriate T_s in order to detect the wave. First, the Nyquist sampling theorem set a maximum T_s to be at least 0.5 times smaller than the inverse of the main frequency component $1/f_o$ of the mechanical excitation as shown in the temporal axis of figure 10(b). In practice, $10T_s < 1/f_0$ will ensure an appropriate sample of the wave along time. For instance, a $f_0 = 2$ kHz wave will require $T_s < 50$ μs. Secondly, T_s controls the sampling of the spatio-temporal propagation of the mechanical wave. Then, as shown in figure 10(b), during the time step T_s, the wave has propagated a distance Δ_z along depth controlled by the wave speed c_s. The calculation of local wave speed is constrained to the minimum measurable spatio-temporal propagation defined by $\Delta_z - T_s$ which will have an impact in the elastography resolution of the OCE technique: the smaller Δ_z, the higher spatial OCE resolution is possible when not limited by the characteristic wavelength. For instance, if the propagation along depth is 2 mm, a $c_s = 5$ m s^{-1} wave will take 0.4 ms. If we choose $\Delta_z = 100$ μm (20 positions along 2 mm), then $T_s = \Delta_z/c_s = 20$ μs, which is equivalent to a 50 kHz A-line rate OCT system. Typical wave-based OCE implementations cover (10–70) kHz using SD-OCT, and from (20–200) kHz in SS-OCT. Currently, the implementation of super-fast swept-sources, OCE at A-line rates in the order of ~1.6 MHz were demonstrated in [157, 158].

5.4.2. M-B acquisition

In typical OCE implementation, the localized excitation source produces the spatio-temporal propagation of a mechanical wave within a tissue sample (figure 11(a)). Ideally, if a snapshot of the propagation process is taken at the instant t_0 along the xz-plane, the acquired spatial frame will completely characterize the wave shape as in figure 11(b). Moreover, the temporal propagation process can be analyzed along the lateral extent (x-axis) to generate xt-maps containing information of the wave speed (figure 11(c)). These will require the simultaneous acquisition of 2D/3D spatial motion for a single instant t_0. However, in typical OCT implementations, the laser beam is steered along the x-axis in order to acquire 2D frames as a collection of A-lines (acquired at $1/T_s$ rate) across different lateral locations. Therefore, the simultaneous acquisition of a single spatial frame with a frame rate equal to the A-line rate ($f_s = 1/T_s$) is not possible.

In this context, the M-B acquisition consists in the synchronized motion excitation and M-mode acquisition for each lateral position along the x-axis in order to capture wave propagation within a 2D space with an apparent frame rate of $f_s^* = 1/T_s$. For instance, using an OCT system with $T_s = 50$ μs, $M = 200$ A-lines along time ($T_s \times M = 10$ ms) in each lateral position x_0 are acquired, covering a lateral field of view of 5 mm using 250 locations (lateral step of $x_s \sim 20$ μm) as shown in figure 11(d). Then, 250 depth-time ($z-t$) frames are obtained and can be rearranged into a 3D matrix of 200 $z-x$ spatial frames distributed along time (10 ms) as shown in figure 11(e), providing the apparent frame rate of $f_s^* = 1/(50\,\mu\text{s}) = 20$ kHz.

This technique has been early implemented in wave-based OCE [95, 140] for the tracking of wave propagation along 2D $z-x$ cross-sections, and it has been demonstrated to reach apparent frame rates up to

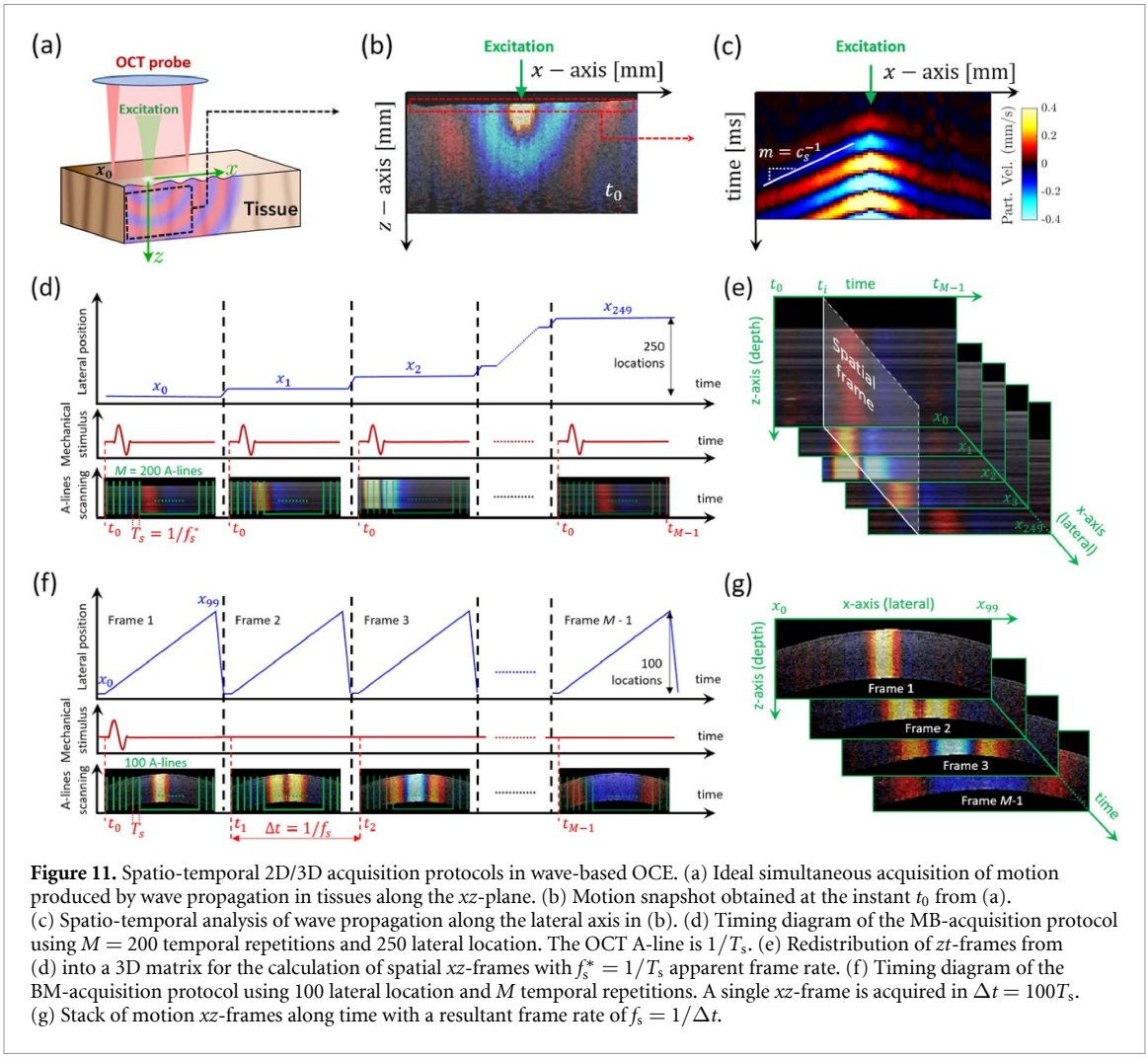

Figure 11. Spatio-temporal 2D/3D acquisition protocols in wave-based OCE. (a) Ideal simultaneous acquisition of motion produced by wave propagation in tissues along the *xz*-plane. (b) Motion snapshot obtained at the instant t_0 from (a). (c) Spatio-temporal analysis of wave propagation along the lateral axis in (b). (d) Timing diagram of the MB-acquisition protocol using $M = 200$ temporal repetitions and 250 lateral location. The OCT A-line is $1/T_s$. (e) Redistribution of *zt*-frames from (d) into a 3D matrix for the calculation of spatial *xz*-frames with $f_s^* = 1/T_s$ apparent frame rate. (f) Timing diagram of the BM-acquisition protocol using 100 lateral location and M temporal repetitions. A single *xz*-frame is acquired in $\Delta t = 100T_s$. (g) Stack of motion *xz*-frames along time with a resultant frame rate of $f_s = 1/\Delta t$.

100 kHz [14]. Since them, M-B mode became one of the most used techniques in wave-based OCE for the study of a high variety of tissues [2, 6, 8]. The downside of this technique is the repeated excitation of tissues as many times as lateral positions are measured, which can be problematic for delicate tissues such as the cornea [8]. Moreover, the main assumption of the M-B mode protocol is that the tissue is not changing its positions and properties while being measured at every lateral position. For the example given previously, the total acquisition time is calculated as $T_s \times M \times 250 = 2.5$ s, and, in clinical *in vivo* cases, any tissue movement will break that assumption and introduce errors. When waves are propagating laterally, M-B mode technique assumes waves are traveling parallel to the *xz*-plane which is not always true as tissues can be anisotropic and guided at the surface. Then, M-B mode has been extended for the 3D detection of wave propagation by adding the *y*-axis for the point-wise M-mode acquisition [65, 159, 160], which has been instrumental for the study of tissue anisotropy [61, 62]. Finally, the M-B mode for 3D studies is impractical for clinical applications due to the extended measurement time in the order of minutes.

5.4.3. B-M acquisition

The B-M mode consists in the repetitive B-mode acquisition of frames along time. Unlike the M-B mode, A-lines are collected laterally along the *x*-axis in order to form a single quasi-instantaneous B-mode frame as shown in figure 11(f). Then, this process is repeated as many times as samples along time are required to track a wave produced by a single stimulation push. The implementation of B-M acquisition has been possible due to recent improvements in the speed of swept-sources, reaching A-line rates of ∼1.5 MHz [84, 157] using Fourier domain mode-locked technology. Then, using a SS-OCT with a $T_s = 0.66$ μs, for a lateral scan of 5 mm sampled along 100 positions (lateral step of $x_s \sim 50$ μm), a single spatial motion frame is acquired in during a time $\Delta t = 100T_s = 66$ μs (figure 11(f)). Then, M spatial $z - x$ frames distributed along time with a frame rate of $f_s = 1/\Delta t \approx 15.2$ kHz are obtained as shown in figure 11(g). Then, the B-M mode allows for the single excitation of waves with frequency content smaller than $f_s/2$. Examples of B-M acquisition have been applied for clinically relevant cases such as the cross-sectional (2D-spatial + 1D-temporal) elastography

of cornea with a total acquisition time of a few ms [26, 157, 158]. B-M mode has been also extended for the volumetric (3D-spatial + 1D-temporal) elastography in which wave propagation is observed along *en face* planes for the OCE of the cornea [84] with total acquisition time ∼100 ms.

B-M acquisition is also possible with OCT implementations with typical A-line rates (10–200 kHz) by creating a low-speed version of shear waves, also called crawling waves (see section 4.2.2), to reduce the acquisition speed requirement. Crawling waves were proposed initially in USE [161, 162] using two continuous vibration sources with a frequency difference of Δf in order to overcome the problem of low acquisition frame rates ranging 0.24–1.06 kHz. Later on, crawling waves were implemented in wave-based OCE for the B-M mode acquisition at a frame rate of 5 Hz, using a SS-OCT system of $T_s = 50$ μs for the tracking of 400 Hz harmonic crawling waves traveling at ∼2000 times slower than shear wave speed [29, 136]. With this methodology, the temporal Nyquist sampling requirement is still achieved even using a SS-OCT with A-line rates in the order of kilohertz.

Other scanning protocols such as line-field OCT [163, 164] and full-field OCT [165, 166] have demonstrated to instantaneously acquire superficial lateral and *en face* displacement fields with temporal frame rates ∼200 kHz, and ∼6.66 Hz, respectively. These methods are instrumental for tracking SAWs at the surface of samples; however, it becomes more difficult when the measurement of wave dynamics along depth is desired. Finally, hybrid methods combining M-B and B-M modes with full-field digital holography [167], and the parallel acquisition using different channels [168] has demonstrated to acquire simultaneous displacements locations by sacrificing acquisition speed.

6. Elastography estimators

In section 2, we have discussed the relationship between shear wave speed (including wave attenuation) and viscoelastic properties of isotropic and anisotropic tissues including shear and Young's moduli. Then, this relationship was extended for other wave branches such as SAWs and Lamb waves (section 3). In figure 12, we summarized the typical mechanical waves and wave interferences found in wave-based OCE according to the spatio-temporal properties of the excitation method, and boundary conditions of tissues. After the type of wave propagating in tissues has been identified, the goal of elastography estimators is to provide accurate estimates of group speed, phase speed, speed dispersion and/or wave attenuation so that these parameters can be used to calculate shear and Young's moduli. Frequently, in many OCE studies, this last step is left undone and only wave speeds are reported due to the difficulties in identifying the actual type of wave propagating on the tissue sample, and the lack of knowledge on the elastic model of the tissue (e.g. type of rheological viscoelastic model, or if the tissue is anisotropic, etc). In this section, we are going to discuss the principal elastography estimators including time-of-flight, Fourier-based, attenuation, and wavelength type estimators. Finally, the definition of elastography resolution is wave-based OCE is reviewed in the last subsection.

6.1. Time-of-flight estimators

Tracking the propagation of a wave along space and time is the most common method in wave-based OCE when transient excitation is used. Theoretically, the group velocity governs the propagation speed of the wave packet composed of multiple frequencies ω within a defined bandwidth $\Delta\omega$ as shown in figure 8(b). Then, the group velocity (c_g) is defined as [19]:

$$c_g(\omega) = \frac{\partial \omega}{\partial \beta}, \tag{6.1}$$

where $\beta(\omega) = \omega / c_{ph}(\omega)$, and $c_{ph}(\omega)$ is the frequency-dependent phase velocity. The definition of speed for shear waves in section 2, and other mechanical waves (e.g. SAW, and Lamb waves) in section 3 refers to the phase velocity. Then, when the phase velocity is constant with respect to frequency (i.e. non-dispersive), from equation (6.1) we have that $c_g(\omega) = c_{ph}$, which is the case of shear waves traveling in elastic and infinite materials. For shear and SAWs traveling in viscoelastic tissues, or Lamb waves traveling in elastic media, $\partial c_g(\omega)/\partial\omega \neq 0$ (i.e. the speed is dispersive), and $c_g(\omega) \neq c_{ph}(\omega)$. Then $c_g(\omega)$ will be related to the frequency content $\Delta\omega$ of the wave packet. The local group speed of a transient wave packet can be estimated by measuring the travel distance of its main peak (Δx) along a period of time Δt as:

$$c_g(\omega_0) = \frac{\Delta x}{\Delta t}, \tag{6.2}$$

where ω_0 is assumed to be closer to the center of the frequency bandwidth of the wave packet. This estimator is also known as the time-of-flight and it has been extensively used in wave-based OCE [20, 78, 87, 93]. The

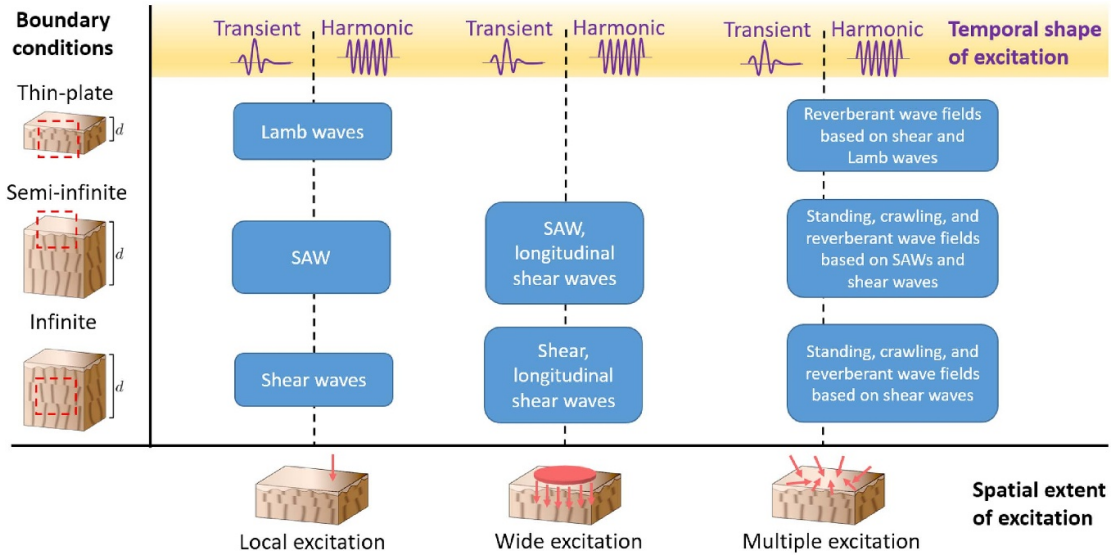

Figure 12. Classification of mechanical waves and interferences typically found in wave-based OCE according to the spatio-temporal properties of the excitation method, and boundary conditions of tissues.

size of Δx will determine how localized the speed is measured along space and it will limit the elastography resolution. As explained in section 5, the characteristics of the selected OCT system, and the motion acquisition protocol will ultimately define the lower limits of Δx and Δt, such that $\Delta x > x_s$, and $\Delta t > T_s$. Typically, the selection of a larger Δx will allow for more spatial and temporal samples of the peak propagation such that a least-squares approached can be used to estimate the local speed with higher accuracy. Then, for spatial locations $p(n) = [x_1, x_2, x_3, \ldots, x_w]$ of the wave peak measured at the instants $q(n) = [t_1, t_2, t_3, \ldots, t_w]$, within a distance Δx with w number of samples, the group speed can be calculated as [29]:

$$c_g(\omega_0) = \frac{\left[\sum_{i=1}^{w} p_i(n)\, q_i(n)\right] - w\overline{p(n)}\,\overline{q(n)}}{\left[\sum_{i=1}^{w} q_i(n)^2\right] - w\overline{q(n)}^2}, \tag{6.3}$$

where $\overline{q(n)} = \frac{1}{w}\sum_{i=1}^{w} q_i(n)$, $\overline{p(n)} = \frac{1}{w}\sum_{i=1}^{w} p_i(n)$.

6.2. Fourier estimators

In the previous section, the time-of-flight technique is limited to the estimation of group velocity corresponding to the central frequency of the wave packet bandwidth since the calculation is performed in the spatio-temporal domain. However, the Fourier analysis of the wave propagation allows for the frequency-dependent estimation of phase velocity with great importance not only for the characterization of viscoelastic tissues (as discussed in section 2.2) but for the correct estimation of elastic properties in thin-plate type tissues where the frequency-dispersive Lamb wave is the prominent perturbation (see section 3.4). Following equation (5.3), the spatio-temporal propagation of a transverse mechanical wave traveling along the x-axis can be represented by the particle velocity field $v_z(x,t)$. Then, $v_z(x,t)$ can be converted into the spectral domain by applying the 2D Fourier transform as:

$$V_z(k,\omega) = \Im_{2D}\{v_z(x,t)\}, \tag{6.4}$$

where k is the wavenumber, and ω is the angular frequency. In the $k-\omega$ map, for every ω_0, the wavenumber $k_{Peak}(\omega)$ with the highest magnitude can be found using peak detection methods. Then, the frequency-dependent wave number can then be converted into phase speed using the wave equation solution as:

$$c_{ph}(\omega) = \frac{\omega}{k_{Peak}(\omega)}. \tag{6.5}$$

Fourier estimators have been used in wave-based OCE for the viscoelastic characterization of tissues using shear/SAWs [48, 159, 169], and Lamb waves [20, 21, 23, 25, 98, 133, 160].

6.3. Wave attenuation estimators

The attenuation of mechanical waves $\alpha(\omega)$ is produced by the energy loss of such waves when they propagate through viscoelastic tissues. As explained in section 2.2, for the case of pure transversal waves, $\alpha(\omega)$ is connected to the shear storage and loss moduli and represents the imaginary part of the complex wavenumber $\tilde{k}(\omega)$ (equation (2.6)). Therefore, wave attenuation can provide important information about the viscoelastic properties of tissues. In the far-field ($r \gg 0$), the asymptotic approximation of amplitude decay $A(r)$ of a mechanical wave when propagating radially along r can be modeled as [47]:

$$A(r) = A_0 \frac{1}{|r|^m} e^{-\alpha(\omega)|r|}, \tag{6.6}$$

where A_0 is the initial wave amplitude. In equation (6.6), the amplitude decay is produced by two effects: geometrical spreading, and loss produced by viscoelastic materials. The geometrical spreading term is represented by the $1/|r|^m$ term, where $m = 0$ for plane waves, $m = 1/2$ for cylindrical waves, and $m = 1$ spherical waves. The $e^{-\alpha(\omega)|r|}$ term represents the decay caused by the viscoelastic attenuation $\alpha(\omega)$ which is the parameter of interest.

In wave-based OCE, $A(r)$ is usually calculated by tracking the peak of the wave packet along r in the far-field ($\sim\lambda$ away from the displacement origin) obtaining $A_{\text{Peak}}(r)$. Making a first-order Taylor approximation of $\alpha(\omega)$ around the central frequency of the wave packet ω_0, we obtain $\alpha(\omega) \approx \alpha_1\omega_0$ [170]. Then $A_{\text{Peak}}(r)$ can be fitted to equation (6.6) with the appropriate section of m, in order to find α_1. Wave attenuation was used to estimate viscoelastic properties in the far-field using USE [36, 47, 171], and wave-based OCE [25, 50, 172]. Nevertheless, in many cases, the excitation source tends to be within the field of view in wave-based OCE [61, 119, 173] which leads to the near-field propagation. In this case, more sophisticated models combining the Fourier approach were proposed to estimate attenuation closer to the excitation region [44, 48].

6.4. Wavenumber estimators

These estimators are devoted to the localized 1D/2D calculation of wavenumber k when harmonic and quasi-harmonic waves at a frequency ω_0 are propagated in tissues. Then, using the wave equation solution $c = \omega_0/k$, the local wave speed can be estimated. In wave-based OCE, speed maps are also called electrograms; however, if the appropriate elasticity model (section 2) and wave type (section 3) are chosen, then elastic/viscoelastic properties of tissue, such as shear or Young's moduli, can also be provided in a map format.

6.4.1. Phase-derivative method

The phase-derivative method [29, 136] leverages the complex-valued spatial particle velocity field ${v_z}^{\text{Cplx}}(x,z)$ when the mechanical wave travels along any direction within the xz-plane. At a particular spatial location, ${v_z}^{\text{Cplx}}(x,z)$ is obtained by (a) calculating the Fourier transform along the temporal dimension resulting in $V_z(x,z;\omega)$, and (b) evaluating the transformed signal at the excitation frequency ω_0: ${v_z}^{\text{Cplx}}(x,z) = V_z(x,z;\omega_0)$. Then, the complex-valued particle velocity can be expressed in term of magnitude, $A(x,z)$, and phase, $\theta(x,z)$, as ${v_z}^{\text{Cplx}}(x,z) = A(x,z)\, e^{i\theta(x,z)}$. Within a small region of interest (ROI) of $L \times L$ mm^2 centered at (x_0, z_0), orthogonal wave numbers corresponding to the propagation directions x, and z, can be calculated based on the spatial derivate of phase as:

$$k_x(x_0,z_0) = \frac{\partial\theta(x,z_0)}{\partial x}, \tag{6.7a}$$

$$k_y(x_0,z_0) = \frac{\partial\theta(x_0,\,z)}{\partial z}. \tag{6.7b}$$

Then, the equivalent 2D spatial phase speed (c_{2D}) of the mechanical wave at the central frequency ω_0 is found using:

$$c_{2D}(\omega_0) = \frac{\omega_0}{\sqrt{{k_x}^2 + {k_y}^2}}. \tag{6.8}$$

The phase-derivative method allows for the generation of phase speed maps with great definition capable of detecting elasticity gradients such as the cornea-sclera interface [22], the boundary between treated and untreated cornea [119], and heterogeneous tissue-mimicking phantoms [29, 119].

6.4.2. Auto-correlation method

In wave-based OCE, different approaches using harmonic active and passive noise sources make use of the auto-correlation in order to map the local wavenumber k of tissues. For instance, reverberant fields are produced by the multiple interferences of waves traveling at different directions when active harmonic displacement sources are activated at a frequency ω_0 at various locations within the target tissue (see section 4.2.2). Within a ROI along the xy-plane, the complex reverberant particle velocity field ${v_z}^{\text{Cplx}}(x,y) = V_z(x,y;\omega_0)$ can be obtained using the Fourier transform evaluated at ω_0. Then, the magnitude of the complex auto-correlation ${v_z}^{\text{Cplx}}(x,y)$ can be fitted to equation (4.5) for the estimation of the local wave number k [65, 137], and ultimately, local phase speed using $c_{\text{ph}}(\omega_0) = \omega_0/k$. Reverberant OCE has demonstrated to achieved higher resolution in the characterization of layered media such as cornea with unprecedented contrast compared to time-of-flight methods when distributed harmonic displacement sources are vibrating at $\omega_0 = 2\pi \times 2000$ rad s^{-1} [65]. However, the need of multiple sources represents a difficult challenge for the translation of this technique into clinical ophthalmic applications.

Another OCE approach leveraging the autocorrelation of motion fields is passive elastography. This technique consists in the correlation analysis of noise-like broadband motion signals to estimate the mechanical properties of tissues. Firstly applied in USE [126], it was then extended to wave-based OCE. Being $u_z(\vec{r},\omega)$ and $\varepsilon_z(\vec{r},\omega)$ the displacement and strain (i.e. the spatial derivative of displacement along the z-axis) fields along the 3D space $\vec{r}$ within a ROI, then the local wavenumber at the center of the ROI $k(\vec{r}_0)$ can be estimated as [127]:

$$k(\vec{r}_0) = \sqrt{-\frac{R_{u_z u_z}(\vec{r}_0, t_0)}{R_{\varepsilon_z \varepsilon_z}(\vec{r}_0, t_0)}}, \tag{6.9}$$

where $R_{u_z u_z}(\Delta\vec{r}, \Delta t)$ and $R_{\varepsilon_z \varepsilon_z}(\Delta\vec{r}, \Delta t)$ are the spatio-temporal autocorrelations of $u_z(\vec{r},\omega)$ and $\varepsilon_z(\vec{r},\omega)$, respectively, evaluated at the center of the ROI $\Delta\vec{r} = \vec{r}_0$, and at time $\Delta t = t_0 = 0$. Passive elastography has been also applied with optical holography [167] and it claims to achieve super-resolution only limited by the imaging resolution of the system [131]. However, the conversion of $k(\vec{r}_0)$ (equation (6.9)) into phase speed using $c_{\text{ph}} = \omega_0/k(\vec{r}_0)$ is not straight forward since the motion produced by noise-type signals tends to have a broad spectrum and a reliable ω_0 is difficult to choose.

6.5. Elastography resolution

The elastography resolution in wave-based OCE refers to the minimum spatial size in which an elasticity gradient (e.g. a stiff inclusion in a softer background) can be detected with accurate quantitative contrast. As demonstrated by Kirby *et al* [27], spatial OCE resolution is primarily defined by the spatial pulse width of the mechanical propagating wave when using transient excitation. Equivalently, in harmonic excitation, the mechanical wavelength is the main parameter that defines elastography resolution [29]. In addition, OCE resolution can be also limited by the spatio-temporal sampling of the OCT implementation, and the assumptions of the chosen wave propagation model [27]. A practical assessment of resolution along a determined spatial r-axis consists in: (a) the preparation of an elastic medium with a step change of elasticity along r (e.g. softer-to-stiffer transition) with known Young's or shear moduli in both regions (e.g. μ^*_{soft}, μ^*_{stiff}) as shown in figure 13(a)-top; (b) the propagation of a mechanical wave (transient or harmonic) along r, motion measurement using an OCT implementation, and the calculation of the wave speed transition along r (figure 13(a)-bottom); and (c) the fitting of the speed transition plot with a Sigmoid function (figure 13(b)) described as:

$$c(r) = c_{\text{soft}} + (c_{\text{stiff}} - c_{\text{soft}}) \frac{1}{1 + \mathrm{e}^{-(r-r_0)/\tau}}, \tag{6.10}$$

where c_{soft}, and c_{stiff} are the speeds of the mechanical wave in the soft and stiff material regions, respectively, measured farther away from the softer-to-stiffer transition location r_0. τ represents the width of the transition centered at r_0. Then, the spatial distance from 20% to 80% of the transition step can be defined by the 20%–80% resolution (R_{2080}) represented by [174]:

$$R_{2080} = 2\ln(4)\tau. \tag{6.11}$$

Another way to characterize the transition width is the application of spatial derivative of equation (6.10) and the evaluation of the full-width half-maximum (FWHM) spreading of the pulse as shown in figure 13(b). As demonstrated in OCE [27], and USE [174], the smaller the pulse width or wavelength of the mechanical wave is, the better OCE resolution (i.e. smaller R_{2080}) will be achieved. In wave-based OCE, the

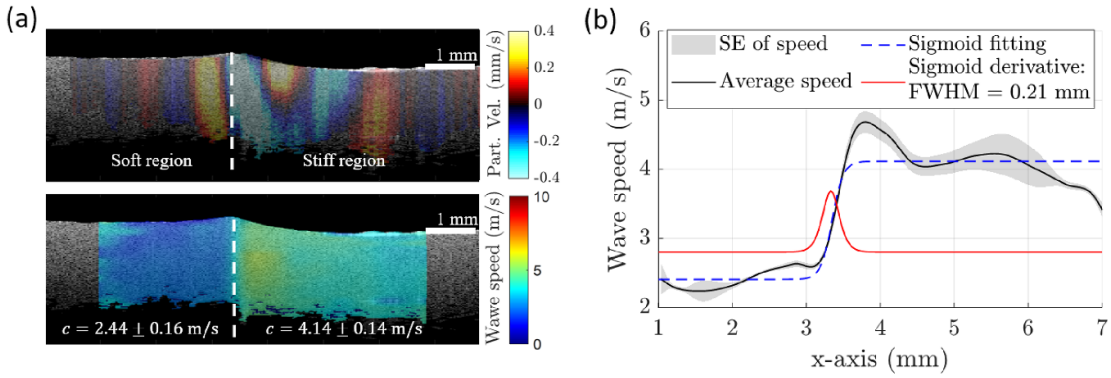

Figure 13. Elastography resolution characterization in wave-based OCE. In (a)-top Wave propagation generated at the center of a two-sided phantom (softer-to-stiffer transition) tissue-mimicking phantom. In (a)-bottom, the elastogram (i.e. wave speed map) was calculated based using a wavelength estimator (section 6.4.1). Average wave speeds in both regions show a differentiated elasticity between both phantom halves. (b) Lateral-dependent speed transition plot obtained from the elastogram in (a) fitted to the Sigmoid function (equation (6.10)). The spatial derivate of the Sigmoid plot was obtained in order to calculate the FWHM spreading of the pulse. Figure reproduced from [119].

OCT imaging resolution is typically greater than the elastography resolution; therefore, the spatio-temporal nature of the mechanical wave, defined by its spectral bandwidth BW in transient waves or the central frequency f_0 of quasi-harmonic/harmonic waves (section 4.3), and the tissue elastic properties (i.e. tissue relaxation time $\sim 1/c_s$), constitutes the main factor in defining the elastography resolution.

Even though R_{2080} can provide a practical measurement of OCE resolution along the r-axis, equation (6.10) assumes a symmetrical transition from softer to the stiffer regions which may not be the case for a higher elastic contrast media. In [27], separate Sigmoid functions are fitted in each side of the transition for a more accurate resolution estimation. Elastography resolution in wave-based OCE has been measured laterally (x-axis) by propagating SAWs or Lamb waves [27, 29, 119], and axially (z-axis) by propagating shear or LSWs [65, 76]. The presence of other mechanical wave branches generated at the boundaries between the softer and stiffer regions of the elastic medium (e.g. shear, Love and Stoneley waves, and back-reflected SAW and Lamb waves) can diminish the effectivity of speed estimators and, consequently, affect the OCE resolution. The use of directional filters has been demonstrated to improve this situation with a low compromise in resolution using typical OCE implementations [175, 176].

7. Techniques and applications

In this section, we are going to review the ten-year progress of wave-based OCE initiated with the study of tissue-mimicking phantoms for the proof of concept of novel OCE methodologies and followed by applications including the elastography of tissues in *ex vivo* conditions, the development of *in vivo* pre-clinical studies and, culminating with the *in vivo* clinical translation cases.

7.1. Phantoms

Elastography studies are often conducted in tissue-mimicking phantoms for the proof of concept of novel implementations of OCE methodologies and their feasibility in the elastography of tissues. In the first wave-based OCE seminal paper in the year 2010, Liang and Boppart [15] measured the propagation speed of surface waves in silicon-based tissue-mimicking phantoms of different stiffnesses produced by a contact harmonic stimulation when vibrated at different driving frequencies (50–500 Hz). This work implemented the first M-B mode acquisition using an SD-OCT system and provided average wave speeds corresponding to the whole sample. Even though this very first implementation only covered six locations along the lateral extent of the sample, the frequency-dependent speed estimations enabled the calculation of Young's modulus of human skin at different sites (volar and dorsal forearm and palm) and conditions (normal, dehydrated, and hydrated). Later on, the early development wave-based OCE started [87, 93, 165, 177–181] with great improvements in the M-B mode acquisition using SS-OCT [93, 178] and SD-OCT [87, 95], allowing the 2D spatial motion measurements of wave propagation in soft phantoms, and, later on, in tissues.

As explained in section 4, the development of excitation sources capable of producing wave propagation was one of the major research branches in wave-based OCE. Contact displacement methods were one of the first in being explored in phantoms and tissues [15, 180, 181] due to its easy implementation with

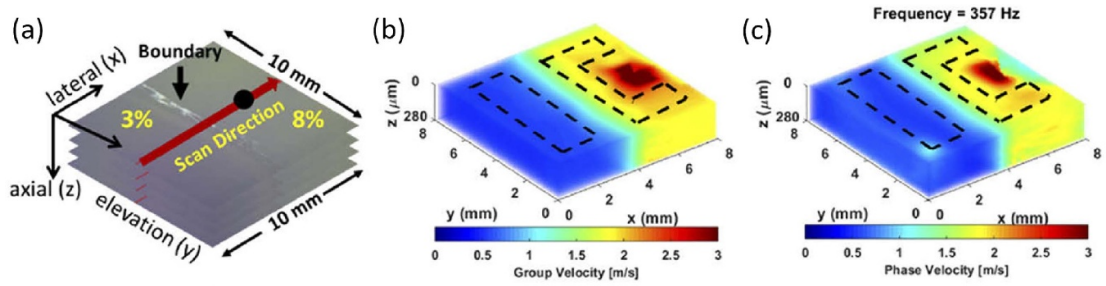

Figure 14. 3D elastography of a heterogeneous tissue-mimicking phantom using transient excitation. (a) B-mode structural *en face* images of a half-sided phantom with soft (3% gelatin) and stiff (8% gelatin) regions. Wave propagation was initiated using a transient ARF excitation (0.5 ms pulse) exited at the center of the stiff region (black dot). (b) 3D elastogram representing group velocity in m s^{-1}. (c) 3D elastogram of phase velocity calculated at $f_0 = 375$ Hz. The near-field effect of wave propagation can be observed in the excitation area of both (b) and (c) cases. Figure adapted from [159].

electromechanical shakers and piezoelectric actuators borrowed from previous development in USE and MRE. Later on, displacement methods were studied in more complex scenarios in order to produce mechanical wave interference patterns using one or more contact sources [29, 65, 136] and the generation of LSWs [76–78] for the elastography of tissues in 2D. Laser-induced excitation was firstly proposed in [112]. It demonstrated the possibility of generating transient Lamb wave propagation in the cornea using a solid-state Nd:YAG laser with 530 nm central wavelength producing a 6 ns pulsed excitation. Then, this technology was further explored in comparison with ultrasonic excitation techniques [114] and analyzed in thermoelastic and ablative regimes depending on the photothermal absorption of the sample and laser pulse energy for its safe application in the elastography of tissues [111]. Recently, laser excitation interaction with dye-loaded perfluorocarbon nanodroplets allowed the generation of high-frequency LSWs propagating towards depth in phantoms [79, 80, 82]. Magnetomotive-based harmonic excitation of mechanical waves (ranging from 300 to 700 Hz) was first demonstrated in [121] for the 2D elastography of heterogeneous and viscoelastic phantoms and some preliminary *ex vivo* tissues. Later on, this technique was explored in combination with thermotherapy dosimetry [122, 123]. ARF excitation was initially developed in USE and borrowed by wave-based OCE for the excitation of waves in phantom studies using single element [48, 92, 135], and phase array transducers [90, 91]. Then, ARF was used for the elastography of tissues in different applications [34, 153, 173, 182]. Air-pulse stimulation for the generation of short-duration and low-pressure waves was proposed in [94] as a pilot study in phantoms, and later on, it was applied for the elastography of ocular [20, 26, 62, 95–101], and other tissues [13, 102–107]. Finally, AC-ARF was proposed in [115] and explored in phantom studies, demonstrating the generation of non-contact (coupled with air), broadband, and localized stimulation of mechanical waves. Later on, this technique was applied for the wave-based OCE of ocular tissues using cylindrically focused [84], spherically focused [117], and confocal [119] ultrasonic transducers.

Phantom studies are fundamental for testing novel elastography estimators. As discussed in section 6, wave-based OCE has been proposed for the elastography of homogeneous viscoelastic [44, 48, 50, 169], and heterogeneous phantoms [29, 76, 77, 87, 127, 136, 159]. For instance, in [159], group ($c_g(\omega_0)$) and phase ($c_{\text{Ph}}(\omega)$) velocity of a transient Rayleigh wave are analyzed in four dimensions (3D along space, and 1D along frequency) when ARF excitation is produce in a bi-layer heterogeneous phantom, as shown in figure 14. Here, a Fourier estimator (section 6.2) is used to reconstruct the local shear wave speed associated with a specific frequency band using the 3D Fourier transform. This estimator is capable of differentiating the softer (3% gelatine) from the stiffer (8% gelatine) phantom regions in 3D and provide frequency-dependent and localized phase speed $c_{\text{Ph}}(x, y, z, \omega)$, fundamental for the viscoelastic characterization of tissues. Finally, phantom studies are also instrumental for the elastography resolution characterization of wave-based OCE techniques as demonstrated when mechanical waves travel along axial (z-axis) [65, 76], and lateral (x-axis) [27, 29, 131] directions.

7.2. Tissues *ex vivo*

In wave-based OCE, *ex vivo* studies are conducted for the feasibility analysis of OCE methodologies in a specific type of tissue. In this highly controlled environment, complex studies of tissue biomechanics, including viscoelasticity, elastic anisotropy, and non-linearity, are also possible due to the low perturbation of other noise-type displacement sources. *Ex vivo* studies have been instrumental for the understanding of basic science questions related to tissue physiology and pre-clinical applications, such as the study of the effect of diseases and treatments in the mechanical properties of tissues. The most explored application is, undoubtedly, the study of ocular tissues as demonstrated by the ten-year progress of wave-based OCE [8],

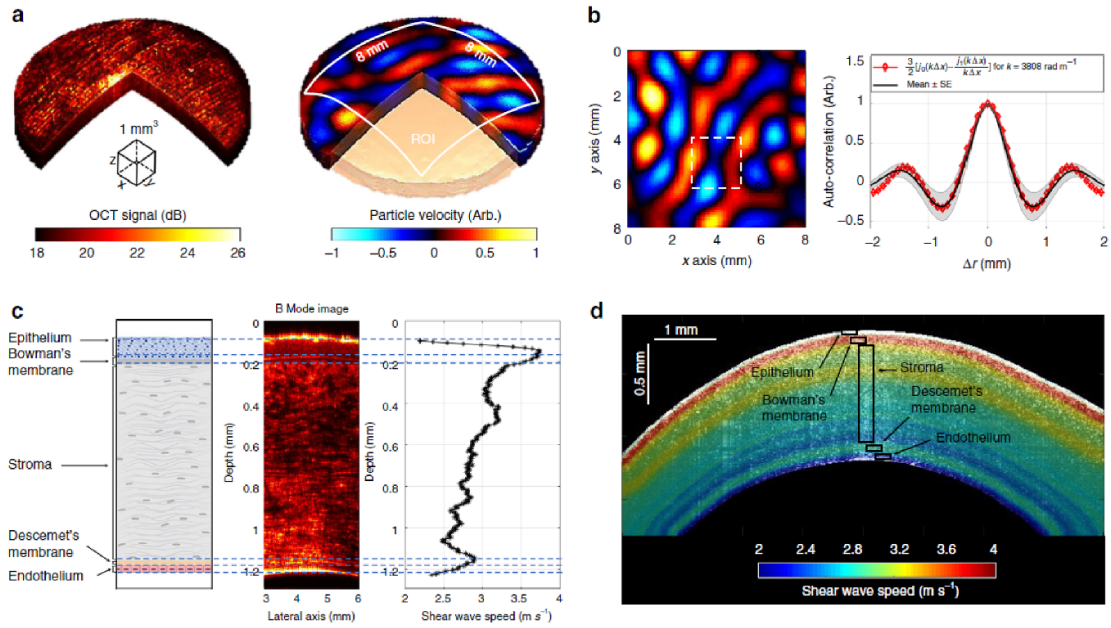

Figure 15. Elastography of layers in *ex vivo* porcine cornea using reverberant shear wave fields (section 4.2.2). (a) B-mode structural (left) and motion (right) volumes of a cornea. Motion represents particle velocity produced by eight localized contact displacement sources vibrating at 2 kHz. (b) The *en face* motion frame (left) extracted from the top layer in (a) is auto-correlated within a smaller region (discontinuous-line square) and fitted to equation (4.5) (right) for the estimation of local wavelength and local shear wave speed. (c) Depth-dependent shear wave speed obtained after applying (b) to every single corneal depth is compared against the physiological description of corneal layers (left) and the structural OCT image of the cornea (center). (d) Shear wave elastogram (in m s^{-1}) of the cornea superimposed with its B-mode structural image. Figure reproduced from [65].

followed by other tissues, including skin, muscle, brain, and cartilage, which will be discussed in the following subsections.

7.2.1. Ocular tissues

The imaging of ocular tissues has always been the main application of OCT due to its higher imaging resolution, low light scattering (e.g. cornea and crystalline lens), and non-contact nature. Following the historical precedent, wave-based OCE has advanced the knowledge of ocular biomechanics covering different tissues such as the cornea, sclera, crystalline lens, and retina. The cornea is one of the most critical parts of the eye since it is responsible for almost two-thirds of the eye's total refractive power [183]. The cornea is a highly organized tissue that contains at least five layers (layered-medium), it is viscoelastic, anisotropic, and non-linear. Several wave-based OCE methodologies using different excitation sources, acquisition protocols, and processing estimators have been applied to the study of the different corneal properties. For instance, the estimation of elasticity of individual corneal layers was achieved by tracking the Lamb wave speed [20] and analyzing reverberant shear wave fields [65] at each depth location from the corneal epithelium to the endothelium. In figure 15, the use of reverberant fields for the elasticity characterization of layers in *ex vivo* porcine cornea is shown. Here, an SD-OCT was used to obtain 3D structural and motion (particle velocity) spatio-temporal volumes (figure 15(a)) when the cornea was stimulated with eight contact-type harmonic actuators vibrating at $\omega = 2\pi \times 2000$ rad s^{-1}. Then, the complex-autocorrelation method (section 6.4.2) was applied in local regions of the motion field at a particular corneal surface, and fitted to equation (4.5) for the estimation of local wavenumber k as shown in figure 15(b). Then, the depth-dependent shear wave speed is calculated using $c_s = \omega/k$ for every corneal layer along depth. Figure 15(c) shows the agreement between the depth-dependent speed obtained using the reverberant method, the structural OCT profile, and the anatomical distribution of some of the corneal layers. Finally, figure 15(d) shows the elastogram of cornea (in m s^{-1}) superimposed with its B-mode structural image.

The cornea is considered a thin-plate type tissue (corneal thickness in the order of typical excitation wavelengths); therefore, Lamb waves are more likely to propagate (section 3.4). Other corneal properties were characterized with wave-based OCE using Lamb waves. Corneal anisotropy has been explored with the direction-dependent propagation of transient Lamb waves using air-pulse stimulation [62], and with a nearly incompressible transverse isotropic model when transient waves are stimulated using a cylindrically focused air-coupled transducer [23]. Moreover, corneal viscoelasticity in *ex vivo* porcine eyeballs was estimated using the frequency-dependent Lamb wave speed obtained using Fourier analysis (section 6.2)

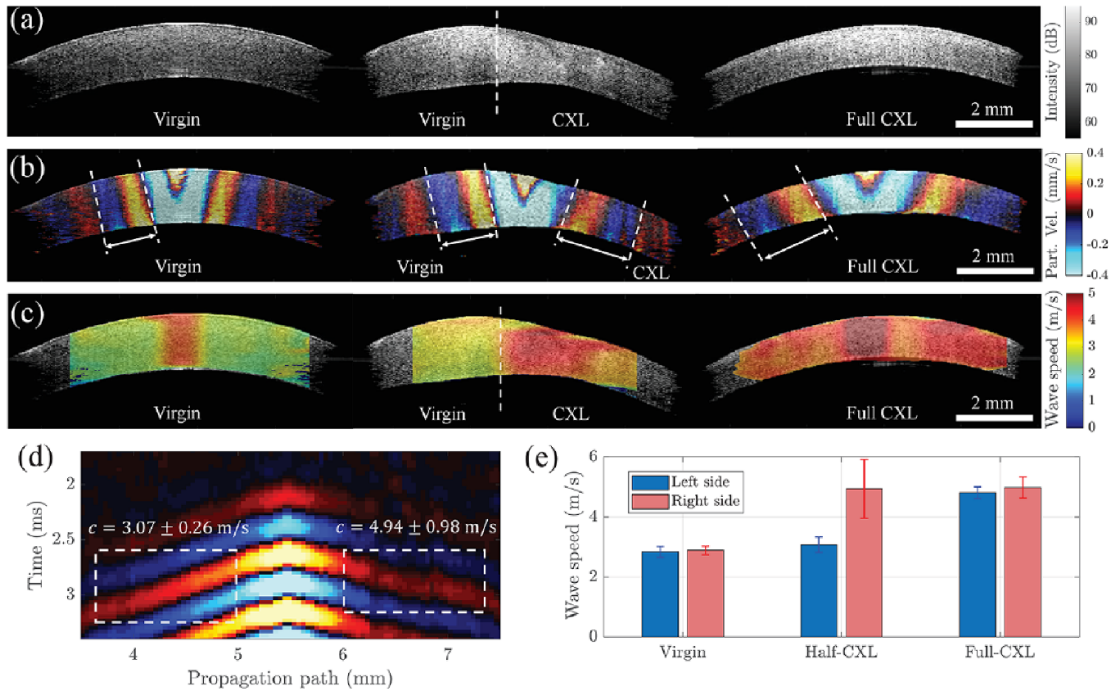

Figure 16. Wave-based OCE of *ex vivo* porcine cornea under localized UV-CXL treatment. (a) B-mode structural images of untreated (left), half-CXL-treated, and full-CXL-treated corneas. (b) Particle velocity snapshots (extracted at $t_0 = 1.5$ ms instant) showing Lamb wave propagation in corneas under the cases in (a) produced using an AC-ARF excitation method (quasi-harmonic vibration at 2 kHz) focused at the corneal apex. (c) Lamb wave speed elastogram of the corneas in (b) obtained using a wavelength estimator (equation (6.8)). (d) Space-time map showing average propagation of Lamb waves in the half-CXL-treated cornea case. (e) Comparison of average Lamb wave speeds obtained in the left and right side of each corneal case obtained from (c). Figure reproduced from [119].

fitted to a modified Rayleigh-Lamb wave model (equation (3.6)) [21, 25, 133], which takes into account the corneal thickness, and the air and fluid interfaces at the corneal epithelium and endothelium, respectively. Corneal tissue is also non-linear; i.e. it gets stiffer as it is stretched by the increase of the intraocular pressure or other external forces. Corneal non-linearity has been measured using multiple excitation techniques, including AC-ARF [84, 119], air-pulse stimulation [20, 26, 62], and contact methods [22, 65]. Finally, other effects in *ex vivo* corneal elasticity such as age [95] and hydration [98] have been explored using air-pulse stimulation of Lamb waves.

One major contribution of wave-based OCE in ophthalmology is understanding the effect of corneal treatments on the biomechanics of the cornea. Being able to screen and monitor corneal health over time is fundamental for clinical applications and helps doctors during clinical decision-making. Riboflavin/ultraviolet-A corneal collagen cross-linking (UV-CXL) is a clinical treatment that increases the stiffness of the cornea, and it is used when a degenerative corneal disease such as Keratoconus weakens the tissue and reduces its thickness and stiffness [184]. The effect of UV-CXL and other variations in the stiffening of the cornea has been explored using transient Lamb wave propagation in *ex vivo* porcine [101, 119, 160, 172], and rabbit [99, 100, 185] eyeballs. Here, measurements of group speed in the cornea tend to increase after the UV-CXL has been provided, demonstrating this treatment's effect. In particular, the localization of the UV-CXL treatment can be achieved with elevated lateral resolution (∼0.21 mm) in a pair of *ex vivo* porcine corneas when a quasi-harmonic excitation at 2 kHz is produced with a confocal AC-ARF method (see figure 16) [119]. Figure 16(a) shows the first corneal pair when no-treatment (left) and half-sided UV-CXL treatment (center) was applied, while the second pair was subjected to the full UV-CXL treatment (right). Lamb wave propagation can be observed for each when motion snapshots are taken at the same 1.5 ms instant showing differentiated wavelength (figure 16(b)). In figure 16(c), Lamb wave speed maps are shown for each case where the untreated (left), half-treated (center), and full-treated (right) regions can be clearly identified. In particular, for the half-treated case, differentiated Lamb wave phase speed can be estimated in both regions from spatio-temporal propagation maps (figure 16(d)) and compared against phase speeds at the same 2 kHz frequency for the untreated and full-treated cases as shown in figure 16(e).

Other ocular tissues have also been studied using wave-based OCE, including *ex vivo* sclera [22, 119, 127, 186, 187], limbus [22], and crystalline lens [89, 179, 188]. The elastography of the sclera remains a challenging task due to its elevated stiffness compared to the cornea, which results in higher

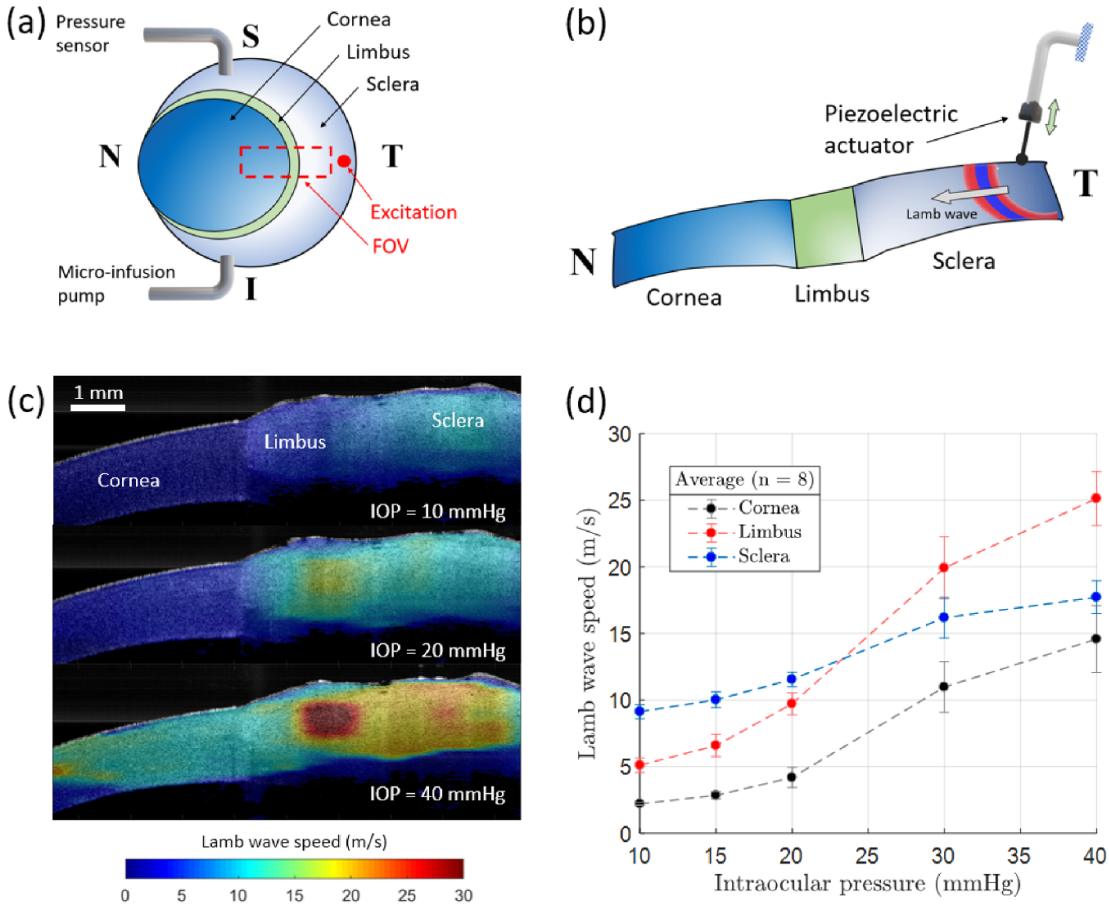

Figure 17. Wave-based OCE of the *ex vivo* porcine anterior segment of the eye. (a) Experimental schematic showing the eyeball being cannulated for the IOP control using a closed-loop system. The FOV indicates the region being scanned using an SS-OCT system. (b) Schematic showing a contact displacement method (based on a piezoelectric actuator generating quasi-harmonic excitation at 800 Hz) producing Lamb waves propagation from the sclera all the way to the cornea passing through the limbal connecting tissue. (c) Lamb wave speed elastograms (in m s^{-1}) of the anterior segment of the eye when IOP is subject to 10, 20, and 40 mmHg. (d) Comparison of average Lamb wave speed in cornea, limbus, and sclera tissues for different IOP levels. Error bars represent inter-sample standard error ($n = 8$ eyeballs). Figure adapted from [22].

propagation speeds (longer wavelengths) which diminishes the effectivity of time-of-flight and wavenumber estimators. In [22], the biomechanics of the anterior segment of the eye, including cornea, sclera, and the connecting tissue between them called limbus is explored as a function of intraocular pressure (IOP) using a closed-loop IOP controller system (figure 17(a)), and quasi-harmonic excitation produced by a contact displacement stimulation (figure 17(b)). Figure 17(c) shows Lamb wave speed elastograms of the corneo-scleral junction for 10, 20, and 40 mmHg IOP levels showing elasticity differentiation between cornea and sclera. Interestingly, Lamb wave speed in the limbal tissue is in between cornea and sclera and rapidly increases when the IOP is increased, reaching the point of surpassing scleral Lamb speed (figure 17(d)), suggesting that limbus has enough structural flexibility to change its elasticity in order to stabilize the anterior eye shape during IOP changes [22].

7.2.2. Other tissues

The application of wave-based OCE has also been instrumental in the study of other *ex vivo* tissues, including skin elastography using air-pulse [103] and laser-based [113] stimulation; the study of cardiac tissues under normal conditions [104] and myocardial infarction [105, 106], heart valves [189], uterus [190], liver [52, 123], brain [76, 191], cartilage [107], soft tumors [93], skeletal muscle [61], diaphragm muscle [24], and breast [192] tissues. Besides the study of ocular tissues, skin elastography has been of major interest in wave-based OCE since the imaging resolution of OCT implementations is capable of resolving tissue layers such as epidermis, dermis, and hypodermis with great detail compared to other imaging modalities. Since the safety and contact requirements for skin elastography using OCT are less restrictive than ocular tissues, its translation to pre-clinical and clinical implementations has been possible as described in sections 7.3 and 7.4. Finally, capillary wave propagation has been proposed for the study of mechanical properties of fluids such as surface tension in [193, 194]. Unlike waves in viscoelastic solids, capillary phase velocities also

depend on other parameters including fluid depth, gravity, and surface tension, offering a potential path for the exploration of fluid tension in the blood which can provide relevant information on hematological diseases [193].

7.3. *In vivo* pre-clinical studies

When wave-based OCE methodologies have been further investigated *ex vivo* and have demonstrated documented clinical potential, they are later explored *in vivo* using animal models. *In vivo* studies allow researchers to compensate for motion and noise sources that are present in clinical environments, study safety concerns, and understand tissue biomechanics in more realistic conditions. In ophthalmological applications, several *in vivo* ocular tissues have been explored using wave-based OCE. In [180], air-pulse stimulation is used in mouse corneas for measuring age-related elastic changes by measuring Lamb wave speeds ranging 1–4 m s^{-1}, and suggesting that elasticity of the cornea is increasing with age. The elastography of four *in vivo* normal rabbit corneas was conducted in [117] using AC-ARF stimulation and Lamb wave propagation analysis, finding an average group speed of 5.96 $\pm$ 0.55 m s^{-1}. In this study, the compensation of axial motion produce by the heartbeat and respiration of the rabbits was applied in order to obtain 3D displacement fields of wave propagation. The effect of UV-CXL treatment in nine rabbit corneas was also explored *in vivo* using air-pulse stimulation in [195]. Here, the wave speeds in corneas were converted into Young's modulus using the Rayleigh wave model (section 3.3) and compared for different UV-CXL treatment irradiances in preoperative, 30 min postoperative, and one week postoperative corneal conditions. *In vivo* crystalline lens and retina have also been studied using wave-based OCE. In [173], the elastography of rabbit lens and cornea was simultaneously measured using orthogonal ARF excitation in order to measure elastic changes in lens produced by aging, which is related to presbyopia disease. Results of this study suggested that lenticular tissue becomes stiffer as the age increases with wave speeds ranging from 1.5 m s^{-1} to 3 m s^{-1}. The elastography of layers in the posterior *in vivo* rabbit eye was conducted in [182] using ARF excitation in a confocal configuration with the OCT imaging probe. In this study, at least five different layers were detected with mechanical wave speeds up to 5.8 m s^{-1}, and compared with histological images. Finally, some *in vivo* pre-clinical pilot studies were conducted in human corneas using air-pulse stimulation for characterization of natural frequencies [11], and the effect of respiration and heartbeat in the corneal elastography [10].

In vivo wave-based OCE studies have also been conducted in other tissues such as skin. In [102], the effect of systemic sclerosis in the elastic properties of skin has been explored in control and bleomycin-induced systemic sclerosis-like mouse skin using air-pulse stimulation for the propagation of SAWs. Results showed a differentiated Young's modulus between control and sclerosis-induced tissues, suggesting that this OCE method is a promising technology for the quantitative, rapid, and non-invasive skin diseases diagnosis. Finally, some pilot studies involving the elastography of *in vivo* normal human skin has been conducted in [15, 181] using SAWs generated by contact displacement methods.

7.4. *In vivo* clinical studies

Only a subset of wave-based OCE technologies has been translated into clinical applications with human subjects for the study of diseases, treatments, and the development of biomarkers. In the study published by Ramier *et al* [12], the shear modulus of *in vivo* human corneas of 12 healthy subjects (ages between 27 and 67) were characterized using Lamb wave propagation produced by a contact displacement stimulation probe (figure 18(a)) attached to the OCE clinical prototype that complies with the subjects' motion. The first demonstration of wave-based OCE applied to human corneas *in vivo* as described in [196]. In another study [12], corneas were harmonically excited at eight different frequencies (2–6 kHz by steps of 2 kHz), and motion frames were acquired using the M-B acquisition protocol (43 kHz A-line rate) implemented in an SS-OCT system, as shown in figure 18(b). Frequency-dependent Lamb waves speed and attenuation were measured in each cornea (figure 18(c)), and an average 7.86 $\pm$ 0.75 m s^{-1} wave speed and 0.11 $\pm$ 0.014 mm kHz wave attenuation were found for the 12 subjects. As explained in section 3.4, the asymptotic behavior of Lamb waves along frequency is the Rayleigh/Scholte wave speed, which is used in [12] to convert wave speed into the average corneal shear modulus of 72 $\pm$ 13.7 kPa. The estimated maximum acoustic intensity produced by the vibration contact in the cornea was 7.5 mW cm^{-2}, which is below the spatial-peak temporal-average intensity limit of 17 mW cm^{-2} set by the safety limits in ophthalmic ultrasound [120]. Some limitations of this study include the contact nature of the mechanical excitation that produced minor reversible corneal epithelial disruption as reported in 3 out of 12 subjects. This effect, together with the deformation produced by the contact tip in corneas, should be carefully considered in the potential friction-induced damage to the corneal epithelium and patient discomfort. Overall, this study constitutes the first measurement of shear modulus in human *in vivo* corneas using a contact displacement wave-based OCE method that takes into account the dispersive behavior of Lamb waves and attenuation.

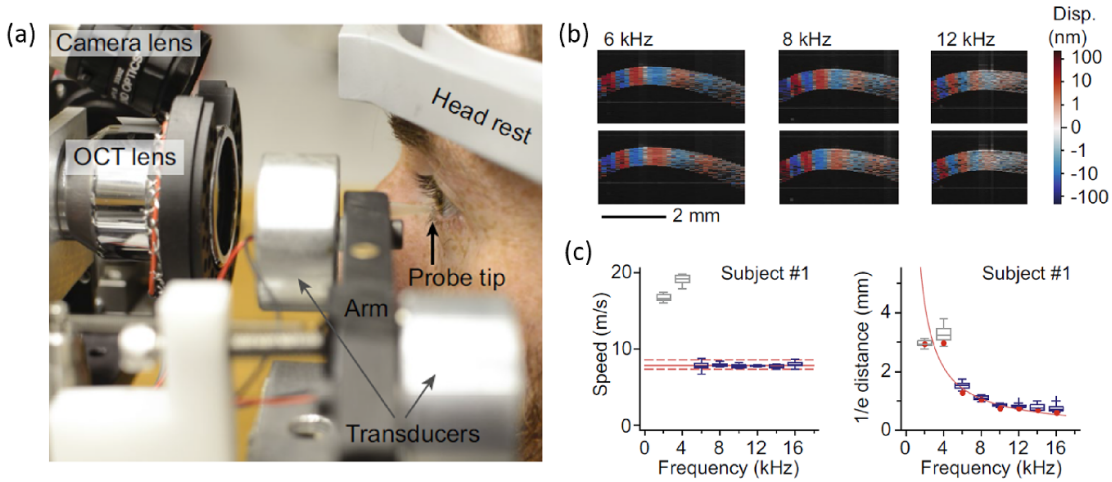

Figure 18. *In vivo* elastography of human corneas using wave-based OCE. (a) Schematic of the contact probe, including the OCT system and the vibration contact displacement tip touching the corneal epithelium. (b) Displacement snapshots showing Lamb wave propagation at (6, 8, 12) kHz harmonic frequencies. (c) Depth-dependent phase speed (left) and attenuation (right) extracted in the cornea of one of the human subjects over a range of 6–16 kHz frequencies. Gray box plots were left out from the analysis due to insufficient wave amplitude. Figure adapted from [12].

Another study of wave-based OCE in human corneas was recently published by Lan *et al* [197], using non-contact air-pulse stimulation as a source of Lamb wave propagation in the corneas of nine subjects. Here, a common-path SD-OCT system was combined with a fixation target and a camera in order to monitor the corneal position and compensate for the eye's lateral motion. Short-duration air pulses (840 μs) produced Lamb wave propagation in corneas, and wave speed was estimated using the time-of-flight technique (section 6.1). Lamb wave speeds were found in the range from 2.4 to 4.2 m s^{-1} ($n = 18$ corneas from the nine healthy subjects), showing minor differences in the elasticity between left and right eyes in the same subject. This study (and pilot results in [196]) constitutes the first *in vivo* report of the elastography of the human cornea using a fully non-contact approach with great potential to expand into the clinical translation. Unlike other excitation methods, air-pulse stimulation is proven to be safe as it has been used in other ophthalmic devices for decades [109]. Finally, the low frequency content of waves generated by air-pulse stimulation in corneas prevents the generation of elastograms and remains one of the major limitations of this approach.

Another example of clinical translation of wave-based OCE is the study published by Liu *et al* [13] for the assessment of systemic sclerosis in human skin *in vivo*. Here, non-contact air-pulse stimulation is used to produce Rayleigh waves in the skin of 12 patients (eight control, and four with systemic sclerosis) in order to calculate Young's modulus using equation (3.4). Average Young's moduli of 9.7 $\pm$ 3.9 kPa and 16.4 $\pm$ 3.9 kPa were found in normal and systemic sclerosis skin subjects, respectively, showing a significant increase of elasticity for the disease case. These results were compared with the modified Rodnan Skin Score, which is the gold standard in evaluating dermal thickening in systemic sclerosis, showing a strong correlation. This study shows the potential of wave-based OCE for the development of biomarkers capable of screening skin diseases with high repeatability (interclass correlation coefficient range: 0.76–0.95). Limitations of this study include the difficulty of obtaining 2D/3D spatial elasticity maps capable of differentiating elasticity gradient along lateral and depth directions due to the low frequency content of the air-pulse stimulation. Nevertheless, this study constitutes the first clinically useful demonstration of wave-based OCE in the characterization of systemic sclerosis disease.

8. Challenges and opportunities

In the previous sections, we have summarized the main mechanical properties and boundary conditions of tissues (section 2), and how wave-based OCE leverages the propagation of different types of mechanical waves (section 3) produced by excitation sources of distinct physical nature and coupling properties (section 4). Depending on the requirements of the study, including tissue condition (e.g. *ex vivo, in situ, in vivo,* and/or clinical), type of tissue under analysis (e.g. the ocular tunic, skin tissue, etc), spatial extend (e.g. 2D cross-sectional, and/or 3D volumetric) and temporal requirements (e.g. fast acquisition <1 s or extended acquisition), the selection of the suitable acquisition protocol for motion measurement is made (section 5). Then, the use of the appropriate elastography estimator (section 6) will mainly depend on the type of mechanical wave generated, the boundary conditions of the tissue, and the assumptions on the tissue

mechanical properties and distribution. Elastography estimators coupled with the appropriate wave model allows for the translation of wave properties (e.g. speed, attenuation, etc) into quantitative mechanical parameters such as Young's or shear moduli, which have been proven to be instrumental for the understanding of tissue physiology, pathological cases and treatment monitoring (section 7). Over the last decade of progress in wave-based OCE, different challenges and opportunities have emerged, highlighting the present and future direction in this field. In this section, we are going to comment on some of the major challenges, including elastography resolution, accuracy and repeatability, acquisition speed, and clinical translation, including the discussion of possible novel opportunities.

In section 6.5, we explained the impact of the spatio-temporal characteristics of the propagating mechanical wave in the elastography resolution: the smaller the pulse width or characteristic wavelength of the mechanical wave is, the higher OCE resolution will be achieved. Therefore, the generation of waves with greater localization (i.e. smaller excitation area) and higher frequency content in tissues is desired. Transient excitation using short pulses has been demonstrated to produce wave propagation with larger bandwidths which allow the calculation of frequency-dependent phase speed, fundamental for the elastography of tissues using Lamb waves, and viscoelastic studies using SAWs and shear waves. However, if the input pulse excitation time T_{Pulse} is smaller than the relaxation time of the tissue τ_{R} (see figure 8(a)), the frequency bandwidth of the propagating pulse will always be limited by τ_{R} no matter how small T_{Pulse} is selected (figure 8(b)). Moreover, the displacement attenuation of waves with higher frequency components constraints the propagation to smaller regions closer to the excitation area. These mechanisms set a fundamental limit in the frequency bandwidth of waves using transient excitation and represent a major challenge in the achievement of higher elastography resolution. An interesting alternative to mitigate the effect of wave attenuation is to improve the efficiency of motion detection in PhS-OCT by using the common-path configuration approach. The common-path technique has been implemented with great success in SD-OCT [149], and SS-OCT [14] for the motion detection of waves up to hundreds of picometers. Other alternatives rely on the use of quasi-harmonic excitation, as shown in figure 8(c). Unlike the transient case, quasi-harmonic excitation concentrates more displacement energy to narrower bandwidth centered at $f_0 = 1/2T_{\text{Pulse}}$ breaking the limitation of τ_{R}, as shown in figure 8(d). In this way, the mechanical wavelength is reduced for the resolution improvement by the cost of calculating wave speed dispersion in a smaller bandwidth. Finally, quasi-harmonic excitation allows the comparison of speed maps at the same frequency f_0 which is fundamental for the accuracy and repeatability of measurements in longitudinal tissue studies. Quasi-harmonic and harmonic excitation has been successfully used with contact displacement [22, 29, 65, 87] and AC-ARF [119] excitation methods for the generation of detailed elastograms at the same central frequency f_0.

The accuracy and repeatability of elastography estimations are important requirements for wave-based OCE methods to be used in clinical applications such as the study of biomarkers to distinguish disease from non-disease states of tissues, as well as the development of screening devices to measure the progression of diseases and treatments. The accuracy will be mainly affected by the appropriateness of the mechanical model of wave propagation, assumptions made about tissue elasticity and its boundary conditions, and the correct selection of the elastography estimator. For instance, in the anterior section of the eye, the cornea is an anisotropic, viscoelastic, and non-linear thin layer tissue coupled with air in the top surface and with fluid in the bottom layer. Then, estimations of shear/Young's moduli will disagree if the tissue is considered semi-infinite by using the SAW model (equation (3.4)), a thin-plate, isotropic, and viscoelastic tissue by using the Lamb wave model (equation (3.6)), or a thin-plate, transverse isotropic, and elastic tissue by using the modified derivation of Lamb wave model in [23]. This is possibly the reason why estimations of corneal shear and Young's moduli using wave-based OCE differ greatly with tensile and inflation testing, as reported in [23]. A useful practical guide for the correct selection of wave propagation model can be given and it consists in: the (a) identification of tissue geometry and boundary conditions using structural OCT images (and other imaging modalities), histological and physiological studies; (b) identification of the predominant tissue mechanical properties (e.g. if the interrogated tissue is highly anisotropic, viscoelastic, or non-linear for the conditions in which is going to be measure) consulting to previous rheological and elastography studies; and (c) simulating wave propagation using numerical methods taking into account the previous steps and the properties of the excitation method (i.e. its spatio-temporal characteristics). Based on the spatio-temporal and spectral analysis of the simulated wave propagation, and its comparison with real data from the tissue is question, we can guide our selection of propagation model and tailor it to more specific conditions. This proposed guide only offers a practical exploration approach to the reader based on extensive past work and does not guarantee its validity for all soft tissue cases and conditions.

The repeatability of wave-based OCE estimations will depend on how robust is the selected methodology to the fluctuations of other variables such as OCT system noise (e.g. sensitivity and stability of the system), perturbation of tissues produced by environmental factors (e.g. changes in position, shape, and elasticity of

tissues due to external vibrations, or temperature, pressure or humidity changes), and changes of boundary conditions (e.g. changes in the stress and dimension of tissues). In practical applications, achieving repeatability, accuracy, and high resolution in the same OCE implementation is difficult, and compromises need to be made. For instance, in wave-based OCE, spatial resolution is often sacrificed in order to obtain a more repeatable speed estimation by extending the estimation ROI to almost the whole OCT field of view. Moreover, repeated displacement measurements of the same region can improve the SNR by the cost of extending the acquisition time. Then, the trade-off between resolution, accuracy, and repeatability is always present in wave-based OCE, and prioritizing one over the other will depend on the objectives of the study.

In wave-based OCE, the acquisition speed will depend on the type of OCT implementation (i.e. SS-OCT or SD-OCT, as shown in figure 9) and the acquisition protocol. Here, PhS-OCT is used to detect displacement (or particle velocity) in the nanometer range produce by a wave. Therefore, if the tissue under study is subjected to low frequency motion (e.g. respiration or involuntary movement during *in vivo* studies) producing differential displacements much greater than the OCT speckle size; then, the speckle decorrelation among two consecutive A-lines along time is expected to distort the motion measurements. This problem can be mitigated if the displacement between two consecutive lines is reduced by increasing the acquisition A-line rate and using correlation techniques to track and compensate for the speckle movement [117, 192]. Recent advances in the development of MHz-range swept-source lasers can dramatically reduce the acquisition time of SS-OCT [157, 158]; however, the phase stability of these systems remains a challenging task. Current efforts in the stabilization of swept-sources in wave-based OCE applications rely on optical and electrical optimization [198] and the use of common-path configuration as a reference arm [14]. The use of the common-path technique mitigates the fluctuations between the reference and sample arm and has also been demonstrated in SD-OCT implementations [149].

Finally, only a subset of wave-based OCE technologies [12, 13, 197] has been translated into clinical applications with human subjects for the study of diseases and the development of biomarkers. This final step requires not only the effectivity and robustness of the OCE methodology but also the development of safety studies demonstrating that the OCE imaging under the selected acquisition protocol and the energy absorbed during the mechanical excitation of tissues are below any safety limit proposed by regulatory agencies. In this regard, only air-pulse and contact displacement stimulation methods have been implemented for the study of human cornea and skin, as of yet. In the elastography of cornea, air-pulse is the only non-contact stimulation method proven to be safe as it has been used in clinics for decades [109], with great benefits for the clinical translation since it does not produce patient discomfort and possible damage of corneal epithelium. However, the low frequency content of the stimulated wave highly constraints the elastography resolution and the accuracy of the estimations. On the other hand, contact displacement methods have been proven to produce high-frequency waves in human corneas by the cost of patient discomfort, possible reversible epithelium damage, and the difficult control of the vibration tip position and contact with the tissue. One possible alternative to the challenges proposed by both stimulation methods is the use of AC-ARF excitation technology that can generate high-frequency waves in tissues in a non-contact fashion [84] without propagating ultrasonic pressure waves through tissues as in ARF. Moreover, in [119], a confocal AC-ARF version with an OCT probe is proposed for the elastography of ocular tissues in the anterior segment of the eye with great potential for clinical translation. Here, the coaxial configuration of the AC-ARF transducer and the OCT probe facilitates the easy control and alignment of the excitation location in the cornea at a safe working distance of $\sim$20 mm [119]. Safety studies of AC-ARF technology remain a pending work before it can be translated into clinical applications.

Another challenge in wave-based OCE is the difficulty of measuring elasticity gradients along the axial direction (z-axis) with the same effectivity as in the lateral axis for various tissue-specific applications. As explained in section 3, mechanical waves in OCE tend to be guided by the surface of tissues which limits its propagation along the depth. Novel alternatives using contact displacement excitation have been proposed in order to distinguish depth-dependent elastic distribution in phantoms and tissues, including the use of LSWs [76–78, 80] and reverberant shear wave fields [65]. Unfortunately, this goal has not been yet achieved using non-contact methods and remains the topic of future work. The use of passive elastography estimators combined with active sources [127] comes with an opportunity for the depth- and lateral-resolved elastography of tissues with higher resolution [131]. Finally, in terms of tissue applications, wave-based OCE presents great unexplored opportunities in the anisotropic characterization of corneal tissue, taking into account viscoelasticity and non-linearity for normal, disease, and treatment corneal cases; the depth-dependent and viscoelastic characterization of layers in skin and retina; the elastography of sclera as it is challenging due to its elevated stiffness (Young's modulus in the order of MPa); the elastography of the trabecular meshwork, fundamental for developing biomarkers in glaucoma. Two particular areas that could greatly benefit from recent development in wave-based OCE are tumor mechanobiology and developmental

biomechanics. We predict that these areas, along with the strong emphasis on clinical and commercial translation, will be the main focus of the wave-based OCE technology in the next decade.

9. Conclusion

In this review, the ten-year perspective on the progress of wave-based OCE has been conducted, highlighting major developments in (a) the implementation of novel excitation methods, (b) the proposition of advanced analytical wave models and estimators capable of generating quantitative 2D/3D biomechanical information, and (c) the elastography of a wide variety of tissues including *ex vivo, in vivo* pre-clinical, and clinical studies. Ophthalmology and dermatology remain, undoubtedly, the major medical fields in which wave-based OCE has demonstrated to be the most clinically relevant, as shown by latest translation efforts. Some of the current major challenges leave a broad space for opportunities in the improvement of lateral- and depth-dependent elastography resolution, the accurate and repeatable translation of wave properties into mechanical parameters such as Young's and shear moduli, and the faster and more stable motion acquisition in tissues in 2D and 3D. Future work may combine analytical and numerical techniques based on machine learning's latest progress, expecting to have the first wave-based OCE commercial device in the upcoming decades.

Data availability statement

No new data were created or analyzed in this study.

Acknowledgment

The authors would like to acknowledge the research support provided by NIH grants R01EY022362, R01EY030063, R61AR078078, and R01HD095520.

ORCID iDs

Fernando Zvietcovich https://orcid.org/0000-0003-2467-4168
Kirill V Larin https://orcid.org/0000-0002-5532-5027

References

[1] Parker K J, Doyley M M and Rubens D J 2011 Imaging the elastic properties of tissue: the 20 year perspective *Phys. Med. Biol.* **56** R1
[2] Larin K V and Sampson D D 2017 Optical coherence elastography—OCT at work in tissue biomechanics [invited] *Biomed. Opt. Express* **8** 1172–202
[3] Glaser K J, Manduca A and Ehman R L 2012 Review of MR elastography applications and recent developments *J. Magn. Reson. Imaging* **36** 757–74
[4] Schmitt J M 1998 OCT elastography: imaging microscopic deformation and strain of tissue *Opt. Express* **3** 199–211
[5] Kennedy B F, Kennedy K M and Sampson D D 2014 A review of optical coherence elastography: fundamentals, techniques and prospects *IEEE J. Sel. Top. Quantum Electron.* **20** 272–88
[6] Wang S and Larin K V 2015 Optical coherence elastography for tissue characterization: a review *J. Biophoton.* **8** 279–302
[7] Mulligan J A, Untracht G R, Chandrasekaran S N, Brown C N and Adie S G 2016 Emerging approaches for high-resolution imaging of tissue biomechanics with optical coherence elastography *IEEE J. Sel. Top. Quantum Electron.* **22** 246–65
[8] Kirby M A *et al* 2017 Optical coherence elastography in ophthalmology *J. Biomed. Opt.* **22** 121720
[9] Zaitsev V Y *et al* 2020 Strain and elasticity imaging in compression optical coherence elastography: the two-decade perspective and recent advances *J. Biophoton.* **14** e202000257
[10] Lan G, Gu B, Larin K V and Twa M D 2020 Clinical corneal optical coherence elastography measurement precision: effect of heartbeat and respiration *Transl. Vis. Sci. Technol.* **9** 3
[11] Lan G, Larin K V, Aglyamov S and Twa M D 2020 Characterization of natural frequencies from nanoscale tissue oscillations using dynamic optical coherence elastography *Biomed. Opt. Express* **11** 3301–18
[12] Ramier A *et al* 2020 *In vivo* measurement of shear modulus of the human cornea using optical coherence elastography *Sci. Rep.* **10** 17366
[13] Liu C-H *et al* 2019 Translational optical coherence elastography for assessment of systemic sclerosis *J. Biophoton.* **12** e201900236
[14] Li Y, Moon S, Chen J J, Zhu Z and Chen Z 2020 Ultrahigh-sensitive optical coherence elastography *Light Sci. Appl.* **9** 58
[15] Liang X and Boppart S A 2010 Biomechanical properties of *in vivo* human skin from dynamic optical coherence elastography *IEEE Trans. Biomed. Eng.* **57** 953–9
[16] Low G, Kruse S A and Lomas D J 2016 General review of magnetic resonance elastography *World J. Radiol.* **8** 59–72
[17] Ormachea J and Parker K J 2020 Elastography imaging: the 30 year perspective *Phys. Med. Biol.* **65** 24TR06
[18] Viktorov I A 2013 *Rayleigh and Lamb Waves: Physical Theory and Applications* (New York: Springer)
[19] Graff K F 1975 *Wave Motion in Elastic Solids* (Oxford: Oxford University Press)
[20] Wang S and Larin K V 2014 Noncontact depth-resolved micro-scale optical coherence elastography of the cornea *Biomed. Opt. Express* **5** 3807–21
[21] Han Z *et al* 2017 Optical coherence elastography assessment of corneal viscoelasticity with a modified Rayleigh-Lamb wave model *J. Mech. Behav. Biomed. Mater.* **66** 87–94

[22] Zvietcovich F, Nair A, Singh M, Aglyamov S R, Twa M D and Larin K V 2020 Dynamic optical coherence elastography of the anterior eye: understanding the biomechanics of the limbus *Invest. Ophthalmol. Vis. Sci.* **61** 7
[23] Pitre J J Jr *et al* 2020 Nearly-incompressible transverse isotropy (NITI) of cornea elasticity: model and experiments with acoustic micro-tapping OCE *Sci. Rep.* **10** 12983
[24] Loehr J A *et al* 2018 NADPH oxidase mediates microtubule alterations and diaphragm dysfunction in dystrophic mice *eLife* **7** e31732
[25] Ramier A, Tavakol B and Yun S-H 2019 Measuring mechanical wave speed, dispersion, and viscoelastic modulus of the cornea using optical coherence elastography *Opt. Express* **27** 16635–49
[26] Singh M, Han Z, Nair A, Schill A, Twa M D and Larin K V 2017 Applanation optical coherence elastography: noncontact measurement of intraocular pressure, corneal biomechanical properties, and corneal geometry with a single instrument *J. Biomed. Opt.* **22** 20502
[27] Kirby M A *et al* 2019 Spatial resolution in dynamic optical coherence elastography *J. Biomed. Opt.* **24** 1–16
[28] Aumann S, Donner S, Fischer J and Müller F 2019 Optical coherence tomography (OCT): principle and technical realization *High Resolution Imaging in Microscopy and Ophthalmology: New Frontiers in Biomedical Optics* ed J F Bille (Cham: Springer International Publishing) pp 59–85
[29] Zvietcovich F, Rolland J P, Yao J, Meemon P and Parker K J 2017 Comparative study of shear wave-based elastography techniques in optical coherence tomography *J. Biomed. Opt.* **22** 035010
[30] Rus G, Faris I H, Torres J, Callejas A and Melchor J 2020 Why are viscosity and nonlinearity bound to make an impact in clinical elastographic diagnosis? *Sensors* **20** 2379
[31] Riegler J *et al* 2018 Tumor elastography and its association with collagen and the tumor microenvironment *Clin. Cancer Res.* **24** 4455–67
[32] Rozario T and DeSimone D W 2010 The extracellular matrix in development and morphogenesis: a dynamic view *Dev. Biol.* **341** 126–40
[33] Koo T K, Guo J Y, Cohen J H and Parker K J 2013 Relationship between shear elastic modulus and passive muscle force: an *ex-vivo* study *J. Biomech.* **46** 2053–9
[34] Wang M, Byram B, Palmeri M, Rouze N and Nightingale K 2013 Imaging transverse isotropic properties of muscle by monitoring acoustic radiation force induced shear waves using a 2D matrix ultrasound array *IEEE Trans. Med. Imaging* **32** 1671–84
[35] Garteiser P *et al* 2012 MR elastography of liver tumours: value of viscoelastic properties for tumour characterisation *Eur. Radiol.* **22** 2169–77
[36] Nenadic I Z *et al* 2017 Attenuation measuring ultrasound shearwave elastography and *in vivo* application in post-transplant liver patients *Phys. Med. Biol.* **62** 484
[37] Sridhar M and Insana M F 2007 Ultrasonic measurements of breast viscoelasticity *Med. Phys.* **34** 4757–67
[38] Zhang M *et al* 2008 Quantitative characterization of viscoelastic properties of human prostate correlated with histology *Ultrasound Med. Biol.* **34** 1033–42
[39] Elsheikh A and Alhasso D 2009 Mechanical anisotropy of porcine cornea and correlation with stromal microstructure *Exp. Eye Res.* **88** 1084–91
[40] Nguyen T D, Jones R E and Boyce B L 2008 A nonlinear anisotropic viscoelastic model for the tensile behavior of the corneal stroma *J. Biomech. Eng.* **130** 041020
[41] Hatami-Marbini H 2014 Viscoelastic shear properties of the corneal stroma *J. Biomech.* **47** 723–8
[42] Zhang J, Green M A, Sinkus R and Bilston L E 2011 Viscoelastic properties of human cerebellum using magnetic resonance elastography *J. Biomech.* **44** 1909–13
[43] Carstensen E L and Parker K J 2014 Physical models of tissue in shear fields *Ultrasound Med. Biol.* **40** 655–74
[44] Zvietcovich F, Baddour N, Rolland J P and Parker K J 2019 Shear wave propagation in viscoelastic media: validation of an approximate forward model *Phys. Med. Biol.* **64** 025008
[45] Szabo T L and Wu J 2000 A model for longitudinal and shear wave propagation in viscoelastic media *J. Acoust. Soc. Am.* **107** 2437–46
[46] Blackstock D T 2000 *Fundamentals of Physical Acoustics* (New York: Wiley)
[47] Kazemirad S, Bernard S, Hybois S, Tang A and Cloutier G 2016 Ultrasound shear wave viscoelastography: model-independent quantification of the complex shear modulus *IEEE Trans. Ultrason. Ferroelectr. Freq. Control* **63** 1399–408
[48] Zvietcovich F, Rolland J P and Parker K J 2017 An approach to viscoelastic characterization of dispersive media by inversion of a general wave propagation model *J. Innov. Opt. Health Sci.* **10** 1742008
[49] Zhang H *et al* 2018 Modeling ramp-hold indentation measurements based on Kelvin-Voigt fractional derivative model *Meas. Sci. Technol.* **29** 035701
[50] Leartprapun N, Iyer R and Adie S G 2017 Model-independent quantification of soft tissue viscoelasticity with dynamic optical coherence elastography *SPIE BiOS* **10053** 8
[51] Zhang X 2016 Identification of the Rayleigh surface waves for estimation of viscoelasticity using the surface wave elastography technique *J. Acoust. Soc. Am.* **140** 3619–22
[52] Wang Y, Shemonski N D, Adie S G, Boppart S A and Insana M F 2013 Dynamic method of optical coherence elastography in determining viscoelasticity of polymers and tissues *2013 35th Annual Int. Conf. IEEE Engineering in Medicine and Biology Society (EMBC)* pp 117–20
[53] Aglyamov S R *et al* 2015 The dynamic deformation of a layered viscoelastic medium under surface excitation *Phys. Med. Biol.* **60** 4295–312
[54] Royer D, Gennisson J-L, Deffieux T and Tanter M 2011 On the elasticity of transverse isotropic soft tissues (L) *J. Acoust. Soc. Am.* **129** 2757–60
[55] Chatelin S, Charpentier I, Corbin N, Meylheuc L and Vappou J 2016 An automatic differentiation-based gradient method for inversion of the shear wave equation in magnetic resonance elastography: specific application in fibrous soft tissues *Phys. Med. Biol.* **61** 5000–19
[56] Feng Y, Okamoto R J, Namani R, Genin G M and Bayly P V 2013 Measurements of mechanical anisotropy in brain tissue and implications for transversely isotropic material models of white matter *J. Mech. Behav. Biomed. Mater.* **23** 117–32
[57] Nguyen T-M, Aubry J-F, Fink M, Bercoff J and Tanter M 2014 *In vivo* evidence of porcine cornea anisotropy using supersonic shear wave imaging *Invest. Ophthalmol. Vis. Sci.* **55** 7545–52
[58] Rouze N C, Wang M H, Palmeri M L and Nightingale K R 2013 Finite element modeling of impulsive excitation and shear wave propagation in an incompressible, transversely isotropic medium *J. Biomech.* **46** 2761–8

[59] Hossain M, Moore C J and Gallippi C M 2017 Acoustic radiation force impulse-induced peak displacements reflect degree of anisotropy in transversely isotropic elastic materials *IEEE Trans. Ultrason. Ferroelectr. Freq. Control* **64** 989–1001
[60] Chadwick P 1989 Wave propagation in transversely isotropic elastic media—I. Homogeneous plane waves *Proc. R. Soc.* A **422** 23–66
[61] Zvietcovich F, Singh M, Ambekar Y S, Aglyamov S R, Twa M D and Larin K V 2020 Micro air-pulse spatial deformation spreading characterizes degree of anisotropy in tissues *IEEE J. Sel. Top. Quantum Electron.* **27** 1
[62] Singh M *et al* 2016 Investigating elastic anisotropy of the porcine cornea as a function of intraocular pressure with optical coherence elastography *J. Refract. Surg.* **32** 562–7
[63] Li G-Y, Zheng Y, Jiang Y-X, Zhang Z and Cao Y 2019 Guided wave elastography of layered soft tissues *Acta Biomater.* **84** 293–304
[64] Harkrider D G 1964 Surface waves in multilayered elastic media I. Rayleigh and Love waves from buried sources in a multilayered elastic half-space *Bull. Seismol. Soc. Am.* **54** 627–79
[65] Zvietcovich F, Pongchalee P, Meemon P, Rolland J P and Parker K J 2019 Reverberant 3D optical coherence elastography maps the elasticity of individual corneal layers *Nat. Commun.* **10** 4895
[66] Sharma U, Chang E W and Yun S H 2008 Long-wavelength optical coherence tomography at 1.7 microm for enhanced imaging depth *Opt. Express* **16** 19712–23
[67] Sarvazyan A 2001 Elastic properties of soft tissues *Handbook of Elastic Properties of Solids, Liquids, and Gases* vol 3, ed M Levy, H Bass and R Stern (New York: Academic) pp 107–27
[68] Prevedel R, Diz-Munoz A, Ruocco G and Antonacci G 2019 Brillouin microscopy: an emerging tool for mechanobiology *Nat. Methods* **16** 969–77
[69] Scarcelli G, Pineda R and Yun S H 2012 Brillouin optical microscopy for corneal biomechanics *Invest. Ophthalmol. Vis. Sci.* **53** 185–90
[70] Scarcelli G, Kim P and Yun S 2011 *In vivo* measurement of age-related stiffening in the crystalline lens by Brillouin optical microscopy *Biophys. J.* **101** 1539–84
[71] Ambekar Y S *et al* 2020 Multimodal quantitative optical elastography of the crystalline lens with optical coherence elastography and brillouin microscopy *Biomed. Opt. Express* 11 2041–51
[72] Ambekar Y S *et al* 2020 Multimodal optical elastography of *ex vivo* porcine lens *Invest. Ophthalmol. Vis. Sci.* **61** 4643 (https://iovs.arvojournals.org/article.aspx?articleid=2770082)
[73] Wu P J *et al* 2018 Water content, not stiffness, dominates Brillouin spectroscopy measurements in hydrated materials *Nat. Methods* **15** 561–2
[74] Catheline S and Benech N 2015 Longitudinal shear wave and transverse dilatational wave in solids *J. Acoust. Soc. Am.* **137** EL200–5
[75] Carstensen E L and Parker K J 2015 Oestreicher and elastography *J. Acoust. Soc. Am.* **138** 2317–25
[76] Zvietcovich F *et al* 2019 Longitudinal shear waves for elastic characterization of tissues in optical coherence elastography *Biomed. Opt. Express* **10** 3699–718
[77] Zhu J *et al* 2017 Longitudinal shear wave imaging for elasticity mapping using optical coherence elastography *Appl. Phys. Lett.* **110** 201101
[78] Zhu J *et al* 2018 Coaxial excitation longitudinal shear wave measurement for quantitative elasticity assessment using phase-resolved optical coherence elastography *Opt. Lett.* **43** 2388–91
[79] Boerner P *et al* 2020 Repetitive optical coherence elastography measurements with blinking nanobombs *Biomed. Opt. Express* **11** 6659
[80] Liu C H *et al* 2018 Nanobomb optical coherence elastography *Opt. Lett.* **43** 2006–9
[81] Liu C H*et al* 2020 Longitudinal elastic wave imaging using nanobomb optical coherence elastography: erratum *Opt. Lett.* **45** 3296
[82] Liu C H *et al* 2019 Longitudinal elastic wave imaging using nanobomb optical coherence elastography *Opt. Lett.* **44** 3162–5
[83] Nenadic I Z, Urban M W, Aristizabal S, Mitchell S A, Humphrey T C and Greenleaf J F 2011 On Lamb and Rayleigh wave convergence in viscoelastic tissues *Phys. Med. Biol.* **56** 6723–38
[84] Ambroziński Ł *et al* 2016 Acoustic micro-tapping for non-contact 4D imaging of tissue elasticity *Sci. Rep.* **6** 38967
[85] Miller D L *et al* 2020 Diagnostic ultrasound safety review for point-of-care ultrasound practitioners *J. Ultrasound Med.* **39** 1069–84
[86] Fowlkes J B 2008 American institute of ultrasound in medicine consensus report on potential bioeffects of diagnostic ultrasound *J. Ultrasound Med.* **27** 503–15
[87] Song S *et al* 2013 Shear modulus imaging by direct visualization of propagating shear waves with phase-sensitive optical coherence tomography *J. Biomed. Opt.* **18** 121509
[88] Doherty J R, Trahey G E, Nightingale K R and Palmeri M L 2013 Acoustic radiation force elasticity imaging in diagnostic ultrasound *IEEE Trans. Ultrason. Ferroelectr. Freq. Control* **60** 685–701
[89] Wu C, Aglyamov S R, Han Z, Singh M, Liu C-H and Larin K V 2018 Assessing the biomechanical properties of the porcine crystalline lens as a function of intraocular pressure with optical coherence elastography *Biomed. Opt. Express* **9** 6455
[90] Kang H *et al* 2020 2D ultrasonic array-based optical coherence elastography *IEEE Trans. Ultrason. Ferroelectr. Freq. Control* **68** 1
[91] Song S, Le N M, Huang Z, Shen T and Wang R K 2015 Quantitative shear-wave optical coherence elastography with a programmable phased array ultrasound as the wave source *Opt. Lett.* 40 5007–10
[92] Nguyen T-M, Arnal B, Song S, Huang Z, Wang R K and O'Donnell M 2015 Shear wave elastography using amplitude-modulated acoustic radiation force and phase-sensitive optical coherence tomography *J. Biomed. Opt.* **20** 016001
[93] Wang S *et al* 2012 Noncontact measurement of elasticity for the detection of soft-tissue tumors using phase-sensitive optical coherence tomography combined with a focused air-puff system *Opt. Lett.* **37** 5184–6
[94] Wang S *et al* 2013 A focused air-pulse system for optical-coherence-tomography-based measurements of tissue elasticity *Laser Phys. Lett.* **10** 075605
[95] Wang S and Larin K V 2014 Shear wave imaging optical coherence tomography (SWI-OCT) for ocular tissue biomechanics *Opt. Lett.* **39** 41–44
[96] Li J *et al* 2014 Air-pulse OCE for assessment of age-related changes in mouse cornea *in vivo Laser Phys. Lett.* **11** 065601
[97] Allen W M *et al* 2016 Wide-field optical coherence micro-elastography for intraoperative assessment of human breast cancer margins *Biomed. Opt. Express* **7** 4139–53
[98] Singh M *et al* 2018 Quantifying the effects of hydration on corneal stiffness with noncontact optical coherence elastography *J. Cataract. Refract. Surg.* **44** 1023–31
[99] Singh M, Li J, Vantipalli S, Han Z, Larin K V and Twa M D 2017 Optical coherence elastography for evaluating customized riboflavin/UV-A corneal collagen crosslinking *J. Biomed. Opt.* **22** 91504

[100] Singh M *et al* 2016 Evaluating the effects of riboflavin/UV-A and rose-bengal/green light cross-linking of the rabbit cornea by noncontact optical coherence elastography *Invest. Ophthalmol. Vis. Sci.* **57** OCT112–20
[101] Singh M *et al* 2017 Assessing the effects of riboflavin/UV-A crosslinking on porcine corneal mechanical anisotropy with optical coherence elastography *Biomed. Opt. Express* **8** 349–66
[102] Du Y *et al* 2016 Rapid, noninvasive quantitation of skin disease in systemic sclerosis using optical coherence elastography *J. Biomed. Opt.* **21** 46002
[103] Singh M, Wang S, Yee R W and Larin K V 2016 Optical coherence tomography as a tool for real-time visual feedback and biomechanical assessment of dermal filler injections: preliminary results in a pig skin model *Exp. Dermatol.* **25** 475–6
[104] Wang S *et al* 2014 Noncontact quantitative biomechanical characterization of cardiac muscle using shear wave imaging optical coherence tomography *Biomed. Opt. Express* **5** 1980–92
[105] Singh M *et al* 2019 Optical coherence elastography reveals the changes in cardiac tissue biomechanical properties after myocardial infarction in a mouse model *SPIE* vol **10867**
[106] Wang S *et al* 2018 Biomechanical assessment of myocardial infarction using optical coherence elastography *Biomed. Opt. Express* **9** 728–42
[107] Liu C H, Skryabina M N, Li J, Singh M, Sobol E N and Larin K V 2014 Measurement of the temperature dependence of Young's modulus of cartilage by phase-sensitive optical coherence elastography *Quantum Electron.* **44** 751–6
[108] Asaoka R *et al* 2015 The relationship between Corvis ST tonometry measured corneal parameters and intraocular pressure, corneal thickness and corneal curvature *PLoS One* **10** e0140385
[109] Matsuura M *et al* 2016 The relationship between Corvis ST tonometry and ocular response analyzer measurements in eyes with glaucoma *PLoS One* **11** e0161742
[110] Grasland-Mongrain P, Lu Y, Lesage F, Catheline S and Cloutier G 2016 Generation of shear waves by laser in soft media in the ablative and thermoelastic regimes *Appl. Phys. Lett.* **109** 2219011–5
[111] Das S, Schill A, Liu C-H, Aglyamov S and Larin K 2020 Laser-induced elastic wave classification: thermoelastic versus ablative regimes for all-optical elastography applications *J. Biomed. Opt.* **25** 035004
[112] Li C, Guan G, Huang Z, Johnstone M and Wang R K 2012 Noncontact all-optical measurement of corneal elasticity *Opt. Lett.* 37 1625–7
[113] Li C, Guan G, Zhang F, Nabi G, Wang R K and Huang Z 2014 Laser induced surface acoustic wave combined with phase sensitive optical coherence tomography for superficial tissue characterization: a solution for practical application *Biomed. Opt. Express* **5** 1403–19
[114] Zhao L, Vanderlaan D, Yoon H, Liu J, Li C and Emelianov S Y 2020 Ultrafast ultrasound imaging of surface acoustic waves induced by laser excitation compared with acoustic radiation force *Opt. Lett.* **45** 1810–3
[115] Ambrozinski L *et al* 2016 Air-coupled acoustic radiation force for non-contact generation of broadband mechanical waves in soft media *Appl. Phys. Lett.* **109** 043701
[116] Torr G R 1984 The acoustic radiation force *Am. J. Phys.* **52** 402–8
[117] Jin Z *et al* 2019 *In-vivo* 3D corneal elasticity using air-coupled ultrasound optical coherence elastography *Biomed. Opt. Express* **10** 6272–85
[118] Gómez Álvarez-Arenas T E, Camacho J and Fritsch C 2016 Passive focusing techniques for piezoelectric air-coupled ultrasonic transducers *Ultrasonics* **67** 85–93
[119] Zvietcovich F *et al* 2020 Confocal air-coupled ultrasonic optical coherence elastography probe for quantitative biomechanics *Opt. Lett.* **45** 6567–70
[120] Food and Drug Administration 2019 Guidance for industry and Food and Drug Administration staff *Marketing Clearance of Diagnostic Ultrasound Systems and Transducers* (FDA-2017-D-5372, U.S. Department of Health and Human Services) (Rockville, MD: Center for Devices and Radiological Health) 1–60
[121] Ahmad A, Kim J, Sobh N A, Shemonski N D and Boppart S A 2014 Magnetomotive optical coherence elastography using magnetic particles to induce mechanical waves *Biomed. Opt. Express* **5** 2349–61
[122] Huang P C *et al* 2016 Magnetomotive optical coherence elastography for magnetic hyperthermia dosimetry based on dynamic tissue biomechanics *IEEE J. Sel. Top. Quantum Electron.* **22** 104–19
[123] Huang P C *et al* 2019 Interstitial magnetic thermotherapy dosimetry based on shear wave magnetomotive optical coherence elastography *Biomed. Opt. Express* **10** 539–51
[124] Grasland-Mongrain P *et al* 2014 Imaging of shear waves induced by Lorentz force in soft tissues *Phys. Rev. Lett.* **113** 038101
[125] Wu C *et al* 2016 Lorentz force optical coherence elastography *J. Biomed. Opt.* **21** 90502
[126] Gallot T, Catheline S, Roux P, Brum J, Benech N and Negreira C 2011 Passive elastography: shear-wave tomography from physiological-noise correlation in soft tissues *IEEE Trans. Ultrason. Ferroelectr. Freq. Control* **58** 1122–6
[127] Nguyen T-M, Zorgani A, Lescanne M, Boccara C, Fink M and Catheline S 2016 Diffuse shear wave imaging: toward passive elastography using low-frame rate spectral-domain optical coherence tomography *J. Biomed. Opt.* **21** 126013
[128] Nair A, Singh M, Aglyamov S R and Larin K V 2020 Heartbeat OCE: corneal biomechanical response to simulated heartbeat pulsation measured by optical coherence elastography *J. Biomed. Opt.* **25** 055001
[129] Papadacci C, Bunting E A, Wan E Y, Nauleau P and Konofagou E E 2017 3D myocardial elastography *in vivo IEEE Trans. Med. Imaging* **36** 618–27
[130] Li P, Liu A, Shi L, Yin X, Rugonyi S and Wang R K 2011 Assessment of strain and strain rate in embryonic chick heart *in vivo* using tissue Doppler optical coherence tomography *Phys. Med. Biol.* **56** 7081–92
[131] Zemzemi C, Zorgani A, Daunizeau L, Belabhar S, Souchon R and Catheline S 2020 Super-resolution limit of shear-wave elastography *Europhys. Lett.* **129** 34002
[132] Zvietcovich F, Yao J, Rolland J P and Parker K J 2016 Experimental classification of surface waves in optical coherence elastography *SPIE BiOS.* **9710** 97100Z
[133] Han Z *et al* 2015 Quantitative assessment of corneal viscoelasticity using optical coherence elastography and a modified Rayleigh–Lamb equation *J. Biomed. Opt.* **20** 020501
[134] Zhu J *et al* 2016 3D mapping of elastic modulus using shear wave optical micro-elastography *Sci. Rep.* **6** 35499
[135] Zhu J *et al* 2015 Imaging and characterizing shear wave and shear modulus under orthogonal acoustic radiation force excitation using OCT Doppler variance method *Opt. Lett.* **40** 2099–102
[136] Meemon P, Yao J, Chu Y J, Zvietcovich F, Parker K J and Rolland J P 2016 Crawling wave optical coherence elastography *Opt. Lett.* **41** 847–50

[137] Parker K J, Ormachea J, Zvietcovich F and Castaneda B 2017 Reverberant shear wave fields and estimation of tissue properties *Phys. Med. Biol.* **62** 1046–61
[138] Ormachea J, Castaneda B and Parker K J 2018 Shear wave speed estimation using reverberant shear wave fields: implementation and feasibility studies *Ultrasound Med. Biol.* **44** 963–77
[139] Aglyamov S R, Karpiouk A B, Ilinskii Y A, Zabolotskaya E A and Emelianov S Y 2007 Motion of a solid sphere in a viscoelastic medium in response to applied acoustic radiation force: theoretical analysis and experimental verification *J. Acoust. Soc. Am.* **122** 1927–36
[140] Song S, Huang Z and Wang R K 2013 Tracking mechanical wave propagation within tissue using phase-sensitive optical coherence tomography: motion artifact and its compensation *J. Biomed. Opt.* **18** 121505
[141] Podoleanu A G 2012 Optical coherence tomography *J. Microsc.* **247** 209–19
[142] Yasin Alibhai A, Or C and Witkin A J 2018 Swept source optical coherence tomography: a review *Curr. Ophthalmol. Rep.* **6** 7–16
[143] Pan B, Qian K, Xie H and Asundi A 2009 Two-dimensional digital image correlation for in-plane displacement and strain measurement: a review *Meas. Sci. Technol.* **20** 062001
[144] Hild F and Roux S 2006 Digital image correlation: from displacement measurement to identification of elastic properties—a review *Strain* **42** 69–80
[145] Chin L *et al* 2014 Analysis of image formation in optical coherence elastography using a multiphysics approach *Biomed. Opt. Express* **5** 2913
[146] Wang R K, Ma Z and Kirkpatrick S J 2006 Tissue Doppler optical coherence elastography for real time strain rate and strain mapping of soft tissue *Appl. Phys. Lett.* **89** 144103
[147] Yun S H, Tearney G, de Boer J and Bouma B 2004 Motion artifacts in optical coherence tomography with frequency-domain ranging *Opt. Express* **12** 2977–98
[148] Vakoc B, Yun S, de Boer J, Tearney G and Bouma B 2005 Phase-resolved optical frequency domain imaging *Opt. Express* **13** 5483–93
[149] Lan G, Singh M, Larin K V and Twa M D 2017 Common-path phase-sensitive optical coherence tomography provides enhanced phase stability and detection sensitivity for dynamic elastography *Biomed. Opt. Express* **8** 5253–66
[150] Meemon P, Lee K-S and Rolland J P 2010 Doppler imaging with dual-detection full-range frequency domain optical coherence tomography *Biomed. Opt. Express* **1** 537–52
[151] Liu G, Lin A J, Tromberg B J and Chen Z 2012 A comparison of Doppler optical coherence tomography methods *Biomed. Opt. Express* **3** 2669–80
[152] Liu G, Chou L, Jia W, Qi W, Choi B and Chen Z 2011 Intensity-based modified Doppler variance algorithm: application to phase instable and phase stable optical coherence tomography systems *Opt. Express* **19** 11429–40
[153] Zhu J, He X and Chen Z 2019 Acoustic radiation force optical coherence elastography for elasticity assessment of soft tissues *Appl. Spectrosc. Rev.* **54** 457–81
[154] Pinton G F, Dahl J J and Trahey G E 2006 Rapid tracking of small displacements with ultrasound *IEEE Trans. Ultrason. Ferroelectr. Freq. Control* **53** 1103–17
[155] Widman E, Maksuti E, Amador C, Urban M W, Caidahl K and Larsson M 2016 Shear wave elastography quantifies stiffness in *ex vivo* porcine artery with stiffened arterial region *Ultrasound Med. Biol.* **42** 2423–35
[156] Loupas T, Peterson R B and Gill R W 1995 Experimental evaluation of velocity and power estimation for ultrasound blood flow imaging, by means of a two-dimensional autocorrelation approach *IEEE Trans. Ultrason. Ferroelectr. Freq. Control* **42** 689–99
[157] Singh M *et al* 2015 Phase-sensitive optical coherence elastography at 1.5 million A-lines per second *Opt. Lett.* **40** 2588–91
[158] Song S *et al* 2016 Strategies to improve phase-stability of ultrafast swept source optical coherence tomography for single shot imaging of transient mechanical waves at 16 kHz frame rate *Appl. Phys. Lett.* **108** 191104
[159] Liu H-C, Kijanka P and Urban M W 2020 Four-dimensional (4D) phase velocity optical coherence elastography in heterogeneous materials and biological tissue *Biomed. Opt. Express* **11** 3795–817
[160] Singh M *et al* 2016 Noncontact elastic wave imaging optical coherence elastography for evaluating changes in corneal elasticity due to crosslinking *IEEE J. Sel. Top. Quantum Electron.* **22** 266–76
[161] Hoyt K, Castaneda B and Parker K J 2008 Two-dimensional sonoelastographic shear velocity imaging *Ultrasound Med. Biol.* **34** 276–88
[162] Ormachea J, Lavarello R J, McAleavey S A, Parker K J and Castaneda B 2016 Shear wave speed measurements using crawling wave sonoelastography and single tracking location shear wave elasticity imaging for tissue characterization *IEEE Trans. Ultrason. Ferroelectr. Freq. Control* **63** 1351–60
[163] Liu C-H, Schill A, Wu C, Singh M and Larin K V 2016 Non-contact single shot elastography using line field low coherence holography *Biomed. Opt. Express* **7** 3021–31
[164] Liu C-H *et al* 2017 Ultra-fast line-field low coherence holographic elastography using spatial phase shifting *Biomed. Opt. Express* **8** 993–1004
[165] Nahas A, Tanter M, Nguyen T-M, Chassot J-M, Fink M and Boccara A C 2013 From supersonic shear wave imaging to full-field optical coherence shear wave elastography *J. Biomed. Opt.* **18** 121514
[166] Gubarkova E V *et al* 2020 Diagnostic accuracy of cross-polarization OCT and OCT-elastography for differentiation of breast cancer subtypes: comparative study *Diagnostics* **10** 994
[167] Marmin A, Catheline S and Nahas A 2020 Full-field passive elastography using digital holography *Opt. Lett.* **45** 2965–8
[168] Elyas E *et al* 2017 Multi-channel optical coherence elastography using relative and absolute shear-wave time of flight *PLoS One* **12** e0169664
[169] Han Z *et al* 2016 Quantifying tissue viscoelasticity using optical coherence elastography and the Rayleigh wave model *J. Biomed. Opt.* **21** 090504
[170] Parker K J and Baddour N 2014 The Gaussian shear wave in a dispersive medium *Ultrasound Med. Biol.* **40** 675–84
[171] Ormachea J and Parker K J 2020 Comprehensive viscoelastic characterization of tissues and the inter-relationship of shear wave (group and phase) velocity, attenuation and dispersion *Ultrasound Med. Biol.* **46** 3448–59
[172] Li J, Han Z, Singh M, Twa M D and Larin K V 2014 Differentiating untreated and cross-linked porcine corneas of the same measured stiffness with optical coherence elastography *J. Biomed. Opt.* **19** 110502
[173] Li Y *et al* 2019 Simultaneously imaging and quantifying *in vivo* mechanical properties of crystalline lens and cornea using optical coherence elastography with acoustic radiation force excitation *APL Photonics* **4** 106104
[174] Rouze N C, Wang M H, Palmeri M L and Nightingale K R 2012 Parameters affecting the resolution and accuracy of 2D quantitative shear wave images *IEEE Trans. Ultrason. Ferroelectr. Freq. Control* **59** 1729–40

[175] Deffieux T, Gennisson J L, Bercoff J and Tanter M 2011 On the effects of reflected waves in transient shear wave elastography *IEEE Trans. Ultrason. Ferroelectr. Freq. Control* **58** 2032–5
[176] Song P, Manduca A, Zhao H, Urban M W, Greenleaf J F and Chen S 2014 Fast shear compounding using robust 2D shear wave speed calculation and multi-directional filtering *Ultrasound Med. Biol.* **40** 1343–55
[177] Li C, Huang Z and Wang R K 2011 Elastic properties of soft tissue-mimicking phantoms assessed by combined use of laser ultrasonics and low coherence interferometry *Opt. Express* **19** 10153–63
[178] Razani M, Mariampillai A, Sun C, Luk T W H, Yang V X D and Kolios M C 2012 Feasibility of optical coherence elastography measurements of shear wave propagation in homogeneous tissue equivalent phantoms *Biomed. Opt. Express* **3** 972–80
[179] Manapuram R K *et al* 2010 Assessment of wave propagation on surfaces of crystalline lens with phase sensitive optical coherence tomography *Laser Phys. Lett.* **8** 164–8
[180] Manapuram R K *et al* 2012 *In vivo* estimation of elastic wave parameters using phase-stabilized swept source optical coherence elastography *J. Biomed. Opt.* **17** 100501
[181] Li C, Guan G, Reif R, Huang Z and Wang R K 2012 Determining elastic properties of skin by measuring surface waves from an impulse mechanical stimulus using phase-sensitive optical coherence tomography *J. R. Soc. Interface* **9** 831–41
[182] He Y *et al* 2019 Confocal shear wave acoustic radiation force optical coherence elastography for imaging and quantification of the *in vivo* posterior eye *IEEE J. Sel. Top. Quantum Electron.* **25** 7200107
[183] Ruberti J W, Sinha Roy A and Roberts C J 2011 Corneal biomechanics and biomaterials *Annu. Rev. Biomed. Eng.* **13** 269–95
[184] Wollensak G, Spoerl E and Seiler T 2003 Riboflavin/ultraviolet-A–induced collagen crosslinking for the treatment of keratoconus *Am. J. Ophthalmol.* **135** 620–7
[185] Twa M D *et al* 2014 Spatial characterization of corneal biomechanical properties with optical coherence elastography after UV cross-linking *Biomed. Opt. Express* **5** 1419–27
[186] Singh M *et al* 2017 Noncontact optical coherence elastography of the posterior porcine sclera *in situ* as a function of IOP *SPIE* vol 10045
[187] Nair A *et al* 2018 Evaluation of posterior porcine sclera elasticity *in situ* as a function of IOP *SPIE* vol 10474 (https://www.spiedigitallibrary.org/conference-proceedings-of-spie/10474/1047418/Evaluation-of-posterior-porcine-sclera-elasticity-in-situ-as-a/10.1117/12.2289233.short#:~:text=Evaluation%20of%20posterior%20porcine%20sclera%20elasticity%20in%20situ%20as%20a%20function%20of%20IOP&text=The%20biomechanical%20properties%20of%20the,and%20etiology%20of%20ocular%20diseases.&text=The%20results%20show%20an%20increase,as%20a%20function%20of%20IOP)
[188] Wu C *et al* 2015 Assessing age-related changes in the biomechanical properties of rabbit lens using a coaligned ultrasound and optical coherence elastography system *Invest. Ophthalmol. Vis. Sci.* **56** 1292–300
[189] Vekilov D P, Singh M, Aglyamov S R, Larin K V and Grande-Allen K J 2019 Mapping the spatial variation of mitral valve elastic properties using air-pulse optical coherence elastography *J. Biomech.* **93** 52–59
[190] Hakim J *et al* 2018 Can we improve vaginal tissue healing using customized devices: 3D printing and biomechanical changes in vaginal tissue *Gynecol. Obstet. Invest.* **84** 145–53
[191] Ge G R *et al* 2019 A preliminary study on using reverberant shear wave fields in optical coherence elastography to examine mice brain *ex vivo SPIE* vol 10880
[192] Liu X, Hubbi B and Zhou X 2019 Spatial coordinate corrected motion tracking for optical coherence elastography *Biomed. Opt. Express* **10** 6160–71
[193] Liu H C, Kijanka P and Urban M W 2020 Optical coherence tomography for evaluating capillary waves in blood and plasma *Biomed. Opt. Express* **11** 1092–106
[194] Liu H-C, Kijanka P and Urban M W 2020 Fluid surface tension evaluation using capillary wave measurement with optical coherence tomography *AIP Adv.* **10** 055121
[195] Zhou Y *et al* 2019 *In vivo* evaluation of corneal biomechanical properties by optical coherence elastography at different cross-linking irradiances *J. Biomed. Opt.* **24** 1–7
[196] Twa M D, Lan G, Singh M and Larin K 2017 *In-vivo* human corneal elasticity imaging: a phase sensitive optical coherence elastography method *Invest. Ophthalmol. Vis. Sci.* **58** 4324 (https://iovs.arvojournals.org/article.aspx?articleid=2638478)
[197] Lan G, Aglyamov S R, Larin K V and Twa M D 2021 *In vivo* human corneal shear-wave optical coherence elastography *Optom. Vis. Sci.* **98** 58–63
[198] Moon S and Chen Z 2018 Phase-stability optimization of swept-source optical coherence tomography *Biomed. Opt. Express* **9** 5280–95